



DISSERTATION

Model-based Nonlinear Multivariate Control of a Dynamic Fuel Cell Stack Test Bed

ausgeführt zum Zwecke der Erlangung des akademischen Grades
eines Doktors der technischen Wissenschaften

unter der Leitung von

o.Univ.Prof. Dr.techn. Stefan Jakubek

am Institut für Mechanik und Mechatronik
Abteilung für Regelungstechnik und Prozessautomatisierung

eingereicht an der Technischen Universität Wien,
Fakultät für Maschinenwesen und Betriebswissenschaften

von

Dipl.-Ing. János Kancsár



Wien, im Mai 2018

Affidavit

I declare in lieu of oath, that I wrote this thesis and performed the associated research myself, using only literature cited in this volume. If text passages from sources are used literally, they are marked as such.

I confirm that this work is original and has not been submitted elsewhere for any examination, nor is it currently under consideration for a thesis elsewhere.

Vienna, May 2018

János Kancsár

*Science is about knowing;
engineering is about doing.*
H.P.

Kurzfassung

In ihrem Bestreben, schadstoffarme Fahrzeugsysteme zu entwickeln, interessieren sich Automobilhersteller zunehmend für Brennstoffzellen-Technologien. Polymerelektrolytmembran-Brennstoffzellen (PEMFC) gehören zu den vielversprechendsten Technologien, um ein geräuschloses und schadstofffreies Antriebssystem bereitzustellen. Eine PEMFC wandelt Wasserstoff und Sauerstoff in Wasser, elektrische und thermische Energie um. Im Automobilbereich wird der Brennstoffzellenstapel unter hochdynamischen Bedingungen betrieben, so dass sich die Sollwerte im laufenden Betrieb kontinuierlich ändern. Um das Brennstoffzellensystem erfolgreich in den elektrischen Antriebsstrang zu integrieren, ist transientes Testen während der Entwicklung von besonderem Interesse.

Die Luftzufuhr ist einer der wichtigsten Faktoren für die Leistung eines Brennstoffzellensystems. Daher wird in dieser Arbeit ein neuer Ansatz für ein Hardware- und Regelungskonzept der Gaskonditionierung eines dynamischen Prüfstandes für PEMFC Stapel vorgestellt.

Zur Versorgung des Brennstoffzellenstapel-Einlasses mit einströmendem Gasmassenstrom, Gastemperatur, relativer Feuchte des einströmenden Gases und der Gewährleistung des Stapel Druckes werden unterschiedliche Hardwarekonzepte getestet und ausgewertet. Basierend auf der Auswertung wird ein modularer Testprüfstand aufgebaut. Da der entworfene Prüfstand ein nichtlineares Verhalten aufweist, ein Mehrgrößensystem darstellt und die zu regelnden thermodynamischen Größen auf verschiedene Arten miteinander gekoppelt sind, können lineare Regelungsverfahren nicht angewendet werden, um eine ausreichende transiente Regelung sicherzustellen. Deshalb wird ein dynamisches nichtlineares Modell des Prüfstandes hergeleitet und mit Messungen auf dem Prüfstand parametrisiert. Das Systemmodell beinhaltet die wesentlichen dynamischen Eigenschaften, Nichtlinearitäten und thermodynamischen Kopplungen des Systems.

Um eine ausreichende Regelung während transienten Betriebszuständen zu gewährleisten, müssen die Kopplungen und Nichtlinearitäten des Prüfstandes vom Regler berücksichtigt werden. Daher wird ein modellbasiertes nichtlineares Mehrgrößenregelungskonzept entworfen, das auf exakter Eingangs-Ausgangs Linearisierung basiert und die Systemausgänge entkoppelt sowie die Anwendung eines Zwei-Freiheitsgrad-Reglers (2DoF) für jedes Teilsystem ermöglicht. Die Leistungsfähigkeit des realisierten Hardwarekonzepts und des angewendeten nichtlinearen Regelungskonzeptes wird anhand von Messungen am Prüfstand demonstriert. Der entworfene nichtlineare Regler gewährleistet einen akkuraten Trajektorienverlauf während dynamischer Sollwertänderungen.

Ferner kann die entwickelte modellbasierte Vorsteuerung auf eine lineare Regelung angewendet werden, die selbst zur Regelung des nichtlinear gekoppelten Systems nicht ausreichend ist. Die Erweiterung der linearen Reglerstruktur mit zusätzlicher modellbasierter Vorsteuerung verbessert die Performance erheblich.

Abstract

In their strive of developing low pollution vehicle systems automotive manufacturers are more and more interested in fuel cell technologies. Polymer electrolyte membrane fuel cells (PEMFC) are among the most promising technologies to provide a noise free and pollution free propulsion system. A PEMFC converts hydrogen and oxygen to water, electrical and thermal energy. In automotive applications, the fuel cell stack is operated under highly dynamic conditions, which means that the set points are changing continuously during operation. In order to successfully integrate the fuel cell system into the electric power train, transient testing during development is of particular interest.

The air supply is one of the most crucial factors for the performance of a fuel cell system. Therefore, in this thesis a novel approach for a hardware and control design of the gas conditioning system of a dynamic test bed for PEMFC stack testing is proposed.

Different hardware concepts are tested and evaluated in order to supply the fuel cell stack inlet with inflowing gas mass flow, gas temperature, relative humidity of the inflowing gas and stack pressure. Based on the evaluation, a modular test setup is constructed. Since the designed test bed is nonlinear, multivariate and the governing thermodynamic quantities are coupled in various ways, linear control methods can not be applied to provide a sufficient transient control. Therefore, a dynamic nonlinear model of the test bed is derived and parameterised with measurements from the test bed. The system model incorporates the essential dynamic properties, nonlinearities and thermodynamic couplings of the system.

To provide adequate control during transients, the couplings and nonlinearities of the test bed have to be accounted for by the controller. Therefore, a model-based nonlinear multivariate control concept based on exact input-output linearisation is designed, which decouples the system outputs and enables the applications of a Two-Degree-of-Freedom (2 DoF) controller for each subsystem. The performance of the realised hardware concept and applied nonlinear control concept is demonstrated with measurements on the test bed. The designed nonlinear controller ensures accurate trajectory tracking during dynamic set point changes.

Further, the developed model-based feedforward control can be applied to a standard linear controller, which, itself, is insufficient for controlling the nonlinear coupled system. The extension of the linear control structure with additional model-based feedforward control significantly improves the performance.

Danksagung

Diese Dissertation entstand während meiner Anstellung als Projektassistent an der TU Wien am Institut für Mechanik und Mechatronik, Abteilung für Regelungstechnik und Prozessautomatisierung im Rahmen eines FFG Projektes (FCH Media, Projektnummer 840395) in Zusammenarbeit mit der Firma AVL List GmbH und der Firma HyCentA Research GmbH.

An erster Stelle möchte ich mich bei Prof. Stefan Jakubek bedanken der mir die Möglichkeit eröffnet hat, im Bereich der Regelungstechnik eine Dissertation zu verfassen. Insbesondere gilt mein Dank für die kompetente Leitung des Projekts und die fachliche Unterstützung. Weiters bedanke ich mich bei meinen Kollegen am Institut, die das gute Arbeitsklima wesentlich mitgestaltet haben und für fachliche Diskussionen jederzeit zur Verfügung standen.

Mein Dank gilt auch den Kollegen beim Projektpartner AVL, die in das Projekt entweder fachlich oder organisatorisch involviert waren. Allen voran möchte ich an dieser Stelle Christoph Kügele und Tomas Dehne danken, die immer mit Rat und Tat zur Seite standen.

Auch bei den Mitarbeitern des HyCentA bedanke ich mich ganz herzlich, insbesondere bei Michael Striednig und David Aldrian für ihre tatkräftige Unterstützung am Prüfstand.

Außerdem möchte ich meiner Familie und meiner Freundin Katja für ihre Unterstützung danken. Der allergrößte Dank gilt jedoch meinen Eltern, welche mir diese Ausbildung ermöglicht haben.

János Kancsár

Contents

1	Introduction	1
1.1	PEM Fuel Cell	1
1.2	PEMFC Stack	3
1.3	PEMFC System	4
1.3.1	Reaction Subsystem	4
1.3.2	Thermal Subsystem	5
1.3.3	Water Management Subsystem	5
1.3.4	Power Management Subsystem	5
1.4	PEMFC Stack Test Bed	6
1.5	Contribution	7
2	Test Bed Hardware Design	9
2.1	Hardware Concept	10
2.1.1	Flow Control	10
2.1.2	Heating	12
2.1.3	Humidification	14
2.1.4	Back Pressure Control	16
2.1.5	Fuel Cell Stack	16
2.2	Test Bed	17
2.2.1	Test Bed Construction	17
2.2.2	Test Bed Coupling	21
3	System Description and Modelling	22
3.1	Dynamic Model of Test Bed	22
3.1.1	Describing System Equations	23
3.1.2	Model Modularity	25
3.1.3	Model Couplings and Nonlinearities	26
3.2	Model Stability	27
3.2.1	Lyapunov Stability Analysis	28
3.2.2	System Model Analysis	31
3.3	Model Adaptation and Parametrisation	32
3.3.1	Thermal Inertia Adaptation	32

3.3.2	Model Parametrisation	34
3.3.3	Simulation Results	37
4	Control Design - Nonlinear Multivariate Control	40
4.1	Feedback Linearisation	40
4.2	Feedback Linearisation for Multivariate Systems	43
4.3	Flatness	47
4.4	Feedforward Control	49
4.5	Controller Design for the Nonlinear System Model	49
4.5.1	Exact Linearisation and Nonlinear State Transformation	50
4.5.2	Trajectory Tracking and Error Dynamics	52
4.5.3	System Input Constraints	54
4.5.4	Closed Loop Simulation Results	55
4.6	Stability Analysis of Closed Loop System	57
4.6.1	Boundedness	58
4.6.2	Analysis of System Decoupling	59
4.6.3	Simulation Results	61
5	Implementation and Measurement	64
5.1	Mechatronical Setup	64
5.2	Implementation of Low Level Control Structures	65
5.2.1	Gas Flow Submodule Control	65
5.2.2	Heater Submodule Control	66
5.2.3	Steam Flow Submodule Control	67
5.2.4	Backpressure Valve Submodule Control	68
5.2.5	Mass Flow Observer	69
5.3	Measurement Results for High Level Controller	69
5.3.1	Nonlinear Multivariate Control	70
5.3.2	Linear Control	72
5.3.3	Linear Control with additional Model-based Feedforward Control	73
5.3.4	Discussion of Control Performances	77
6	Conclusions and Outlook	78
A	Mathematics	80
A.1	State Space Coordinate Transformation	80
A.2	Derivation of Disturbance Term for Nominal System	82
A.3	Proof of System Stability for Disturbed System	83
B	Thermodynamics	85
B.1	Supercritical Water Injection	85
B.2	Full Derivation of Temperature Dynamics	86

B.3 Derivation of Nonlinear Flow Equation	88
C Control Parameters Applied for Measurements	91
D Fuel Cell System Definitions	92
List of Figures	92
List of Tables	98
Bibliography	100

Chapter 1

Introduction

In recent years the tightening of the automotive regulation standards [1, 2] led to increasing interest of automotive manufacturers in alternative propulsion systems. Polymer electrolyte membrane fuel cell (PEMFC) vehicles [3–6] are one of the most promising technologies, which could even replace internal combustion engines as power source. Compared to other fuel cell technologies, PEMFCs have the advantage of high power density, zero emission, operating at low temperature and fast response [7, 8].

In order to develop PEM fuel cell technologies, manufacturers rely on high-performance testing environments. The development of fuel cell systems require precise knowledge of the behaviour of the single components during operation. This applies to the fuel cell stack itself, but also for each subcomponent of the fuel cell system. Especially for automotive applications transient testing is of particular interest.

In this thesis, a novel approach for hardware and control design of the gas conditioning system of such a transient test infrastructure is proposed.

1.1 PEM Fuel Cell

Fuel cells are energy conversion devices that utilise a chemical reaction to convert fuels directly into electrical energy and produce water as byproduct. In the simplest design, a fuel cell consists of two electrodes (anode and cathode) and an electrolyte, which conducts positively charged hydrogen ions (protons). Polymer electrolyte membrane fuel cells (PEMFC) use hydrogen as fuel and convert it via oxygen to water and electrical and thermal energy [9, 10].

The hydrogen oxidation reaction (HOR) occurring at the anode in the presence of a catalyst is given by



The oxygen reduction reaction (ORR) occurring at the cathode in the presence of a catalyst is given by



the overall reactions accounts to



A state-of-the-art PEMFC design is shown in Fig. 1.1. In a PEMFC, the electrolyte is a solid membrane, which is sandwiched between the two electrodes. This is also referred to as membrane electrode assembly (MEA) [11], which is the heart of a PEM fuel cell. When it is supplied with fuel and air it generates electric power at cell voltages around 0.7 V [12, 13].

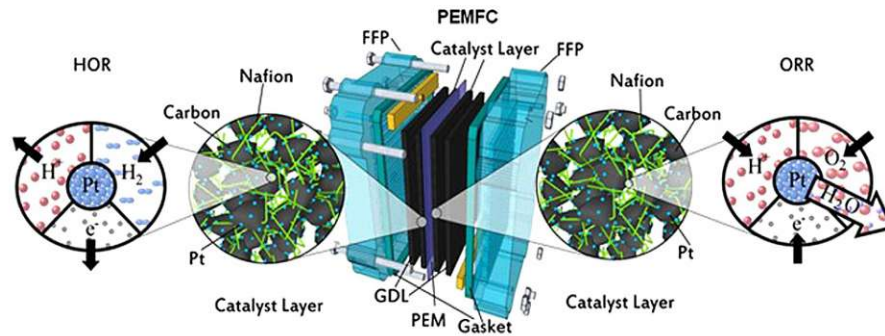


Figure 1.1: Explosive view of a membrane electrode assembly [14].

Low temperature operation of PEMFCs requires noble metal catalysts such as platinum (Pt) to catalyze the H_2 oxidation and O_2 reduction reactions. A great amount of research has been directed at reducing platinum loading in PEMFCs [15]. In the early days of development, Pt was used as both cathode and anode catalyst. This led to a large catalyst loading and high cost. The development of carbon-supported Pt reduced the catalyst loading significantly and at the same time, the fuel cell performance was greatly improved. Carbon-supported Pt can also be used as catalyst for the anode. However, this requires pure H_2 as fuel. Contaminants such as carbon monoxide (CO) poison the catalyst, because CO can strongly adsorb on Pt, blocking the catalytic sites and reducing the catalytic activity of platinum. To improve contaminant tolerance, carbon-supported platinum-ruthenium (PtRu) was developed and nowadays is always used as catalyst for the anode.

The catalyst layers are in close proximity of the membrane. The membrane separates the HOR from the ORR and allows the protons, which are produced at the anode side, to pass through to the cathode side and complete the overall reaction. The electrons are blocked by the membrane and are forced to pass through an electric circuit, where the electrical load is located. Therefore, the MEA is typically located between a pair of current collector plates. The membranes commonly used are Nafion[®] membranes, composed of a perfluorosulfonated polymer. The proton conductivity of the Nafion[®] membrane depends on its water content. The higher the water content, the higher the proton conductivity. Therefore, water management and gas transport are two important factors affecting PEMFC performance. Since the conductivity of the membrane depends on the water content, it can not be used at temperatures higher than 100 °C, which limits the operating temperature. A schematic of the overall working principle is shown in Fig. 1.2.

A porous gas diffusion layer (GDL) electrically connects the catalyst and current collector and ensures that the reactant gases can diffuse to the catalyst layer. The structure of the GDL allows the gas to spread out as it diffuses so that the hydrogen and air will be distributed uniformly across the anode and the cathode. An additional flow field plate (FFP) supports the distribution of the inflowing gas stream. Hereby the gas will be in contact with the entire surface area of the catalyzed membrane. Additionally it conducts the electrons to and from the catalyst layer and plays a crucial role during operation by assisting in the water

management of the membrane. It allows the appropriate amount of water vapour to reach the membrane and keep it humidified, which improves the efficiency of the fuel cell. It also allows the produced liquid water at the cathode to leave the cell so it does not flood, which would prevent the reactant gases to reach the membrane.

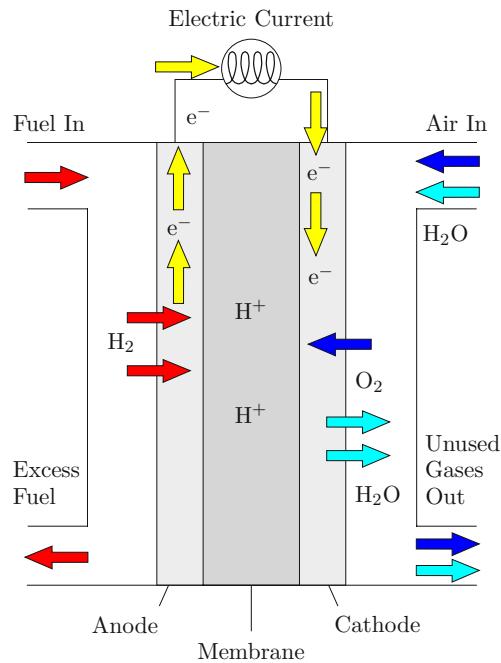


Figure 1.2: Schematic of fuel cell and working principle.

1.2 PEMFC Stack

A fuel cell generates electric power at cell voltages around 0.7 V and power densities of up to 1 Wcm⁻² electrode area [12]. In order to obtain a high power output, single fuel cells are combined together to a so called fuel cell stack (PEMFC stack). Therefore, the cathode of one cell is electrically connected to the anode of the adjacent cell. Thereby a series connection of the fuel cells is realised.

Some key aspects of the design of a fuel cell stack are

- Maintaining the required temperature for each cell during operation.
- Minimising the resistive losses (materials, configuration, contact pressure).
- Preventing internal (between cells) as well as external reactant gas leakage.
- Providing mechanical robustness against e.g. pressure, thermal expansion and external forces during operation and handling such as shocks and vibrations.
- Providing uniform distribution of reactants to each cell as well as inside the cells.

It must be ensured that the reactant gases can still reach the electrodes and that they are evenly distributed over the surface of the anode and cathode. Depending on the stack design fuel utilisation is in the range of 80 - 95 % [16, 17]. Specific design reach up to 96 % fuel utilisation [18].

1.3 PEMFC System

In order to operate a fuel cell stack properly, temperature, pressure, humidity and the supply with the reactant gases have to be controlled by balance of plant (BoP) components [19]. This combination of stack and BoP components is referred to as fuel cell system. PEM fuel cell systems are complex and highly integrated mechatronic systems.

The overall performance of the fuel cell stack not only depends on the dynamics of the integrated fuel cell stack and thus the dynamics of the fuel cells, but largely depends on the dynamics of the auxiliary units and the interaction of and with these units. Constraints or limitations in the dynamic behaviour of the auxiliary units lead to not optimal operating conditions of the stack and can also affect the degradation and, therefore, the lifetime of the fuel cell stack.

In Fig. 1.3, a schematic of a typical PEM fuel cell system for automotive application is shown. Hydrogen is stored in a pressurised tank and supplied with a pressure regulator to the stack, while a recirculation pump ensures a continuous circulation of the hydrogen and a purge valve enables the cleansing of the anode gas path. The air flow is supplied by an air blower and a passive humidifier additionally humidifies the inflowing gas by utilising the already humidified gas, which leaves the PEM fuel cell stack. An additional coolant loop ensures the operating temperature in a certain range. Further schematics of fuel cell system designs are given in Appendix D.

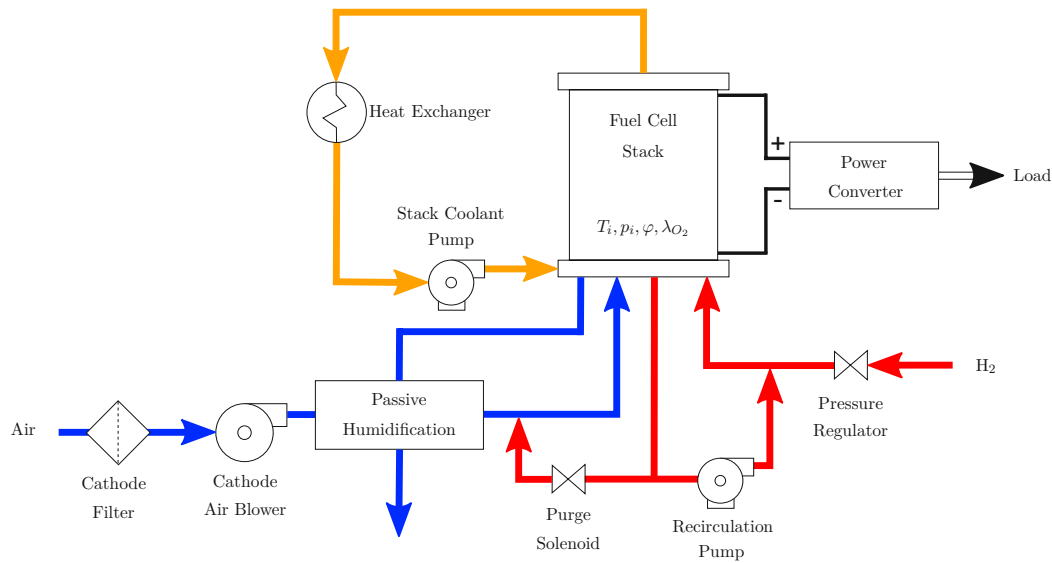


Figure 1.3: Schematic of a fuel cell system.

The fuel cell system can be divided into the following subsystems: reaction subsystem, thermal subsystem, water management subsystem and power management subsystem [20].

1.3.1 Reaction Subsystem

In the reaction subsystem, the reactants, air and hydrogen are fed to the PEMFC stack at a certain stoichiometric ratio, where they react according to Eq. (1.3) and generate electrical energy and water. Air is supplied to the cathode of the PEM fuel cell using a blower or a

compressed air tank, where the inlet pressure is controlled to deliver the required air mass flow for the air-hydrogen stoichiometric ratio. Hydrogen is supplied to the anode of the PEM fuel cell using a pressurised hydrogen tank, where the outlet pressure of the fuel cell stack is controlled by a backpressure regulator at the stack outlet.

1.3.2 Thermal Subsystem

The task of the thermal subsystem is to manage the heat dissipation of the fuel cell system subcomponents. Not only compressors and power electronics, but the fuel cell stack itself is a main source for heat. As a byproduct of the chemical reaction the PEM fuel cell produces thermal energy. To prolong the lifetime of the fuel cell stack, a thermal subsystem has to ensure that it is kept in the optimal operation range. The operating range for the temperature should be kept in a certain range to ensure optimal electrochemical reaction and to keep the integrity of the PEMFC stack material. An uneven temperature distribution affect the evaporation and condensation of water in the reactant gases and further leads to variations in the electrochemical reaction rates. Since the electrochemical reaction is faster at high temperatures, the PEM fuel cell performs better at high temperature ranges. But if the temperature is too high, the membrane dries, wrinkles, shrinks or ruptures. Further, the ohmic resistance of dry membranes is higher, the output voltage becomes lower. Hence, an effective thermal management subsystem can reduce the fuel consumption.

1.3.3 Water Management Subsystem

The membrane transfers protons from the anode to the cathode side. This proton transport is usually takes place in hydrated form, which is referred to as electroosmotic drag. To ensure high membrane conductivity, maintain better membrane stability and to prevent the membrane from drying out, the membrane must be kept saturated with moisture.

However, on the cathode side the water accumulates from the water formed by the ORR and the electroosmotic drag. This may flood the cathode and block O_2 reaching the catalyst layer and, therefore, result in a lower performance. The built-up water gradient inside the membrane can lead to water back-diffusion from cathode to anode. This can decrease cathode flooding and reduce the drying out of the anode caused by electroosmotic drag. At low air flow rates and low temperatures, flooding is increased since the slower water removal by the reduced gas stream and slower water evaporation rate, respectively. Similarly, liquid water formation in the porous GDL affects the PEMFC performance dramatically. To control the membrane humidity, the humidity of the reactant gases can additionally be manipulated to prevent flooding. A humidifying system is normally needed to maintain these requirements and achieve high performance.

1.3.4 Power Management Subsystem

The power management subsystem is used to control the flow of electric power from the PEM fuel cell stack via electronic power devices that process, filter, and deliver the electricity efficiently and smoothly [21–23]. The voltage of PEMFC stacks drops when high currents are drawn during higher load demands because of polarisation and ohmic losses. Therefore, the unstable direct current (DC) power generated from PEMFC stacks has to be controlled by power management subsystems that deliver sufficient power from the PEMFC to the load

and control the electric power output to satisfy load demands in terms of voltage, current, power quality and transients.

1.4 PEMFC Stack Test Bed

The development of fuel cell systems requires the exact knowledge of the behaviour of the components during system operation. This applies to the fuel cell stack itself, but also to the other subcomponents. Especially for automotive application the dynamic behaviour is a crucial property of the whole system.

Since the fuel cell system is operated dynamically, which means that the set point of the fuel cell stack is continuously changed during operation of the vehicle, the focus lies on the transient behaviour of the stack and the system subcomponents.

To prolong the lifetime and to successfully integrate a fuel cell stack into the electric power train, it is important to understand the transient behaviour of the fuel cell stack during set point changes. Stationary measurements of the fuel cell stack have little significance for the transient behaviour of the stack. Therefore, one of the main challenges in developing a fuel cell system for automotive application is transient testing of the stack.

Transient testing of the fuel cell stack yields results, which account for the effects of gas diffusion, membrane water diffusion, mechanical stress on the membrane and water management during set point changes. With these results, the fuel cell system can efficiently be designed to prolong the lifetime of the fuel cell stack. Therefore, to develop efficient fuel cell systems manufacturers rely on a high-performance testing environment during testing and development.

An automotive fuel cell stack test bed should enable to

- make specifications for subcomponents of FC systems,
- optimise system subcomponents in regard to price, power, dynamics, lifetime of the stack and components,
- optimise the stack for a specific system behaviour/dynamics,
- characterise stacks of different manufacturers,
- develop and optimise the control systems.

Therefore, a test bed should be able to

- operate different stacks,
- set thermodynamic quantities such as mass flow, relative humidity, temperature and pressure of reactants independent of each other,
- ensure exact and precise control of operation conditions,
- ensure repeatability of operation conditions.

In Fig. 1.4, a schematic of a fuel cell test bed is shown. To avoid the coupling of the thermodynamic states of the outflowing quantities to the thermodynamic states of the inflowing

quantities, back coupling of these quantities have to be avoided. Therefore, compared to Fig. 1.3, the outflowing quantities are not further utilised to e.g. humidify the inflowing gas stream. In particular, the test bed supplies the stack with air, fuel and cooling liquid with predefined condition.

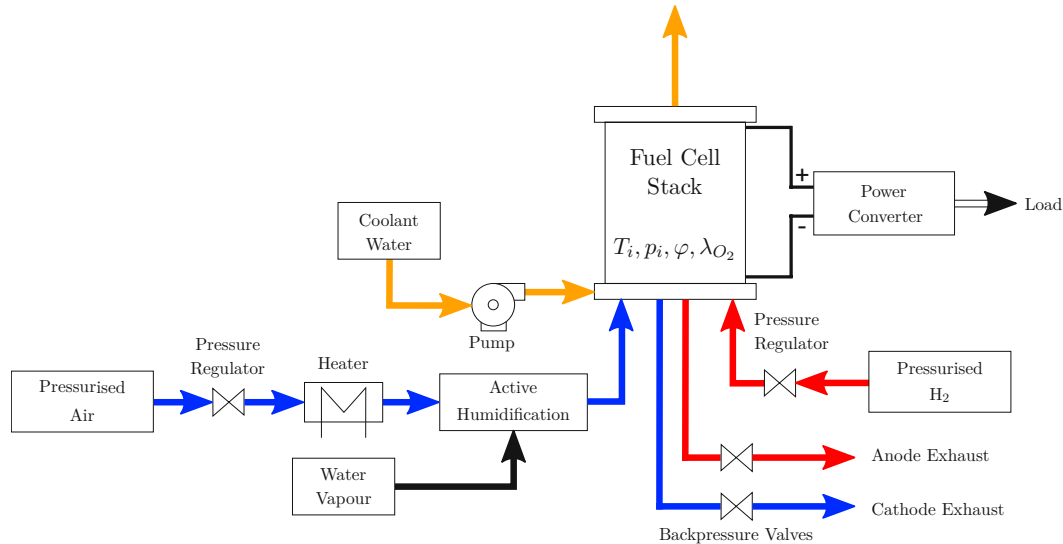


Figure 1.4: Schematic of a fuel cell test bed.

The fuel cell stack test bed itself provides the possibility to perform Hardware-in-the-Loop (HiL) tests with a fuel cell stack and conduct a wide range of experiments without being limited through *slow* BoP components. This enables more accurate tests of the fuel cell stack. The goal of the test bed is to provide a fast and highly dynamic environment to a fuel cell stack. This can be done in order to test the fuel cell stack at operating conditions, which can not be provided by usual BoP components. On the other hand, the test bed can be used to emulate specific BoP components (e.g. component behaviour and dynamics) to test the stack for the interaction with different BoP components without the need to actually build a test setup with all BoP components.

1.5 Contribution

The main component of a fuel cell stack test bed is the gas conditioning system for the inlet gas at the fuel cell stack. In the gas conditioning system, the thermodynamic states are coupled through various relations and represent a nonlinear multivariate control problem. The main control challenge lies in the decoupling of these quantities and in providing sufficiently accurate transitions between two states.

In this thesis, a novel concept for dynamic gas conditioning for transient PEMFC stack testing is proposed. A modular hardware design for the cathode gas conditioning is discussed and evaluated. Based on the evaluation, a hardware setup is realised and a dynamic nonlinear multivariate model of the test bed is derived, which describes the coupling of the thermodynamic quantities in the system. To yield a valid system description, the derived nonlinear model is parameterised with measurements from the test bed. Based on this dynamic model, a nonlinear multivariate control concept is proposed, which deals with the coupling of the

thermodynamic quantities. The stability properties of the proposed control concept are analysed and the control performance is validated with measurements on the realised test bed.

Articles in peer reviewed journals:

During the course of this thesis two journal publications were published. In the first publication, the developed dynamic nonlinear model of the test bed and the model-based nonlinear multivariate control concept have been published in [24].

János Kancsár, Martin Kozek and Stefan Jakubek, Flatness-based feedforward control of polymer electrolyte membrane fuel cell gas conditioning system, *International Journal of Hydrogen Energy* 2016, 41 (39): 17526 - 17538.

<https://dx.doi.org/10.1016/j.ijhydene.2016.06.086>

In the second publication, the hardware design, model parametrisation and validation of the nonlinear control concept with measurements on the test bed have been published in [25].

János Kancsár, Michael Striednig, David Aldrian, Alexander Trattner, Manfred Klell, Christoph Kügele, Stefan Jakubek, A novel approach for dynamic gas conditioning for PEMFC stack testing, *International Journal of Hydrogen Energy* 2017, 42 (48): 28898 - 28909.

<https://doi.org/10.1016/j.ijhydene.2017.09.076>

Patent applications:

In the course of this thesis, the following four patent applications were filed:

- Patent *AT 518518 B1 2017-11-15* describes a model-based nonlinear multivariate control concept for the gas conditioning system of fuel cell stack test beds. *Patent granted on 15.07.2017.*
- Patent PCT/EP2017/081122 (AV-3887AT) describes a novel concept for gas humidification based on supercritical water injection. *Pending patent application.*
- Patent A51007/2017 (AV-3947AT) describes a soft-sensor concept, which can be used to improve transient relative humidity measurements. *Pending patent application.*
- Patent A51040/2017 (AV-3957AT) describes a Power-Hardware-in-the-Loop (PHiL) concept for dynamic fuel cell stack testing. *Pending patent application.*

Chapter 2

Test Bed Hardware Design

The main component of a fuel cell stack test bed is the gas conditioning system for the inlet gas at the fuel cell stack. In the following, the requirements of a gas conditioning for the cathode of a fuel cell stack test bed are discussed and the main challenges are highlighted. Due to the similarity in design, the concepts can partly be applied also for the anode gas conditioning.

For each set point, a fuel cell gas conditioning system has to provide four thermodynamic quantities at the inlet of the fuel cell stack. These deduce from the main challenges to increase the performance and at the same time reduce the rate of degradation of the PEMFC membrane under load changes [26]. To prolong the lifetime of a fuel cell system, it is of utmost importance to understand these quantities and to control them during the operation of the fuel cell system.

First, the gas conditioning system has to provide the gas mass flow into the fuel cell stack. To avoid reactant shortage during operation, which would damage the stack, a sufficient mass flow has to be provided. The so called starvation of the fuel cell is an effect, which is caused by the undersupply of reactants during operation [27–29]. This undersupply reduces the lifetime of the fuel cell [30, 31].

Second, it has to provide the stack pressure. The pressure of a fuel cell stack is an important quantity for the power output of the stack. Low pressure would decrease the power output of the fuel cell system. The system pressure regulation is also essential for the lifetime of the fuel cell stack. A large pressure difference between anode and cathode would damage the membrane and reduce the lifetime of the stack [32].

Third, it has to provide the relative humidity of the inflowing gas. To avoid a dry out of the fuel cell membrane, the relative humidity of the inflowing gas has to be controlled. A dry out or swelling of the membrane would lead to damages of the membrane, which would reduce the lifetime of the fuel cell. The water management of the fuel cell is one of the most vital tasks in operating a fuel cell system [33–35].

Fourth, the gas conditioning system has to provide the temperature of the inflowing mass stream. The gas inlet temperature strongly couples to the relative humidity of the inflowing gas. Therefore, it is evident that the gas conditioning system has to provide the temperature of the inflowing gas mass stream.

In order to achieve a fast transient response of the gas conditioning system, the hardware components, which provide the gas temperature, stack pressure, relative humidity of the

inflowing gas and the total gas mass flow, have to be carefully designed. These quantities are coupled through various relations. By changing one of them, the others will be affected. This has to be considered for controller design, especially for transient operation of the test bed.

2.1 Hardware Concept

In order to meet the discussed requirements, a modular hardware concept for the gas conditioning system is designed. This hardware concept provides actuators to adjust the thermodynamic quantities pressure, temperature, relative humidity and mass flow. Therefore, the system is divided into four functional blocks, namely: flow control, thermal management, humidification and back pressure control. Fig. 2.1 depicts these functional blocks.



Figure 2.1: Schematic of functional blocks.

In the following, different possible hardware concepts for each block depicted in Fig. 2.1 are presented, discussed and a comparative evaluation is given. Based on this evaluations, an experimental hardware setup is realised. Further, in Section 4 a nonlinear multivariate control concept will be designed to enable the independent adjustment of the thermodynamic quantities. Particularly for transient operation of the test bed.

2.1.1 Flow Control

At the test facility the supply gas is provided in a high pressure reservoir. This has the advantage of having predefined thermodynamic conditions at the inlet interface of the test bed. Fig. 2.2 shows three different possible concepts to supply a mass flow to the gas conditioning system.

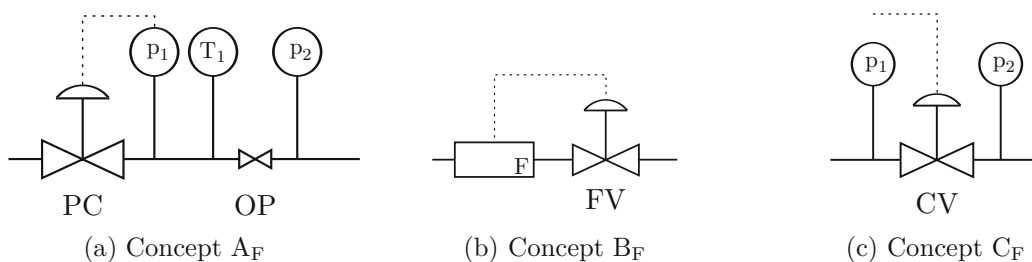


Figure 2.2: Flow control concepts.

In concept A_F (Fig. 2.2a), an orifice plate (OP) is combined with a remote pressure controller (PC) to control the mass flow. The mass flow is a function of the pressure ratio of the upstream pressure (p_1) and the downstream pressure (p_2), inlet temperature T_1 , cross-sectional area A of the orifice plate and thermo-physical properties of the medium (isentropic exponent κ , specific gas constant R). Therefore, the mass flow is controlled by varying the inlet pressure p_1

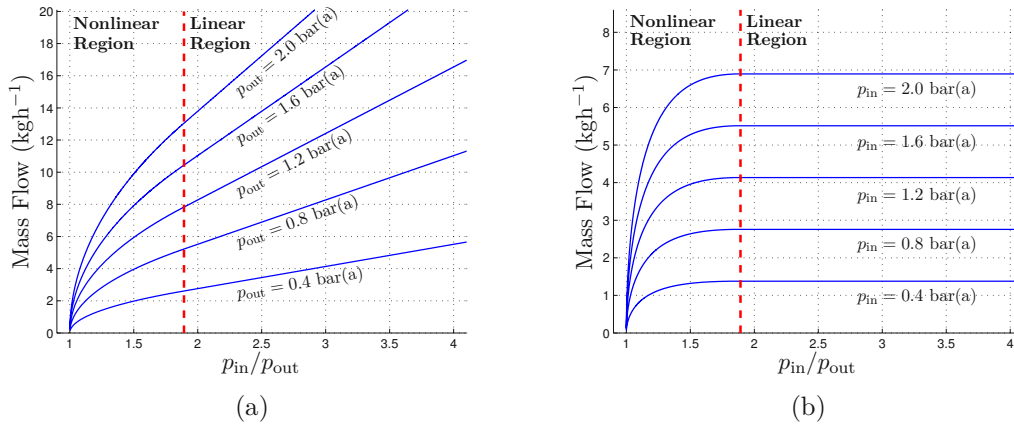


Figure 2.3: The plots show the nonlinear flow equation as a function of the pressure ratio of the upstream pressure (p_{in}) and the downstream pressure (p_{out}). Plot (a) shows the mass flow for varying the upstream pressure and keeping the downstream pressure constant. Plot (b) shows the mass flow for varying the downstream pressure and keeping the upstream pressure constant.

by the pressure regulator. The descriptive nonlinear flow equation is given by Eq. (2.1) [36]. A full derivation of the Eq. (2.1) is given in the Appendix (B.3).

$$\dot{m} = A p_1 \sqrt{\frac{2}{RT_1}} \psi, \quad (2.1)$$

with

$$\psi = \sqrt{\frac{\kappa}{\kappa - 1} \left(\Pi^{\frac{2}{\kappa}} - \Pi^{\frac{\kappa+1}{\kappa}} \right)}, \quad \Pi = \frac{p_2}{p_1}, \quad \kappa = \frac{c_p}{c_v}. \quad (2.2)$$

The function ψ has its maximum value at the so called critical pressure ratio, which is given by

$$\Pi_{\text{crit.}} = \left(\frac{p_2}{p_1} \right)_{\text{crit.}} = \left(\frac{2}{\kappa + 1} \right)^{\frac{\kappa}{\kappa-1}}. \quad (2.3)$$

From this, ψ_{max} for the critical flow derives as

$$\psi_{\text{max}} = \left(\frac{2}{\kappa + 1} \right)^{\frac{1}{\kappa-1}} \sqrt{\frac{\kappa}{\kappa + 1}}. \quad (2.4)$$

Fig. 2.3 shows the evaluation of Eq. (2.1) for different pressure set point variations. The aim is to highlight the physical properties of this nonlinear flow equation in regard to pressure variations above and below the critical pressure ratio given by Eq. (2.3).

In Fig. 2.3a, the upstream pressure is varied and the downstream pressure is kept constant, while in Fig. 2.3b, the downstream pressure is varied and the upstream pressure is kept constant. In both figures, it can be seen that above the critical pressure ratio, given by Eq. (2.3), the nonlinear flow becomes linear. Additionally, Fig. 2.3b shows that a further lowering of the downstream pressure has no effect on the mass flow. On the other hand, increasing the upstream pressure linearly increases the mass flow, as can be seen in Fig. 2.3a. This additionally facilitates control, due to the fact that above the critical pressure ratio the system pressure does not have an effect on the inflowing mass stream.

In concept B_F (Fig. 2.2b) the mass flow is set by a flow controller, which utilises a flow measuring transducer (F) (e.g. coriolis flow meter) and actuates a valve (FV) to control the mass flow. Compared to concept A_F , this concept shows poor response time as well as unstable and imprecise measurements as consequence of the slower mass flow measurement.

In concept C_F (Fig. 2.2c), the mass flow is controlled by directly changing the opening profile and respectively the flow coefficient of a proportional valve (CV). In the above discussed nonlinear flow equation, Eq. (2.1), this would be accounted for by changing the opening area A in the equation. The opening area for the whole operating range of the valve is difficult to obtain and prone to errors. Furthermore, results of various tests pointed out that the regulation of the mass flow via the inlet pressure in concept A_F instead of the opening profile of a pneumatic valve in concept C_F shows faster response time and, therefore, facilitates transient testing.

In consideration of the above discussed arguments, concept A_F was chosen for further implementation in to the test bed. Additionally, the applied pressure regulator has a built-in membrane to regulate the pressure mechanically, which enables fast pressure changes with no additional control loop.

2.1.2 Heating

The following heating concepts are based on heating or cooling of the inflowing gas with heat exchangers. Fig. 2.4 shows the investigated heating concepts.

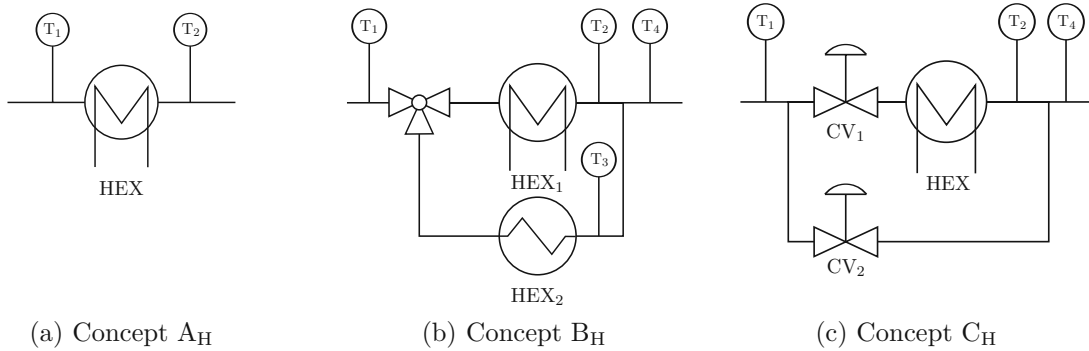


Figure 2.4: Thermal management concepts.

In concept A_H (Fig. 2.4a), the inflowing gas stream is heated, respectively cooled by a dynamic heating (heat exchanger (HEX)). The outflowing gas temperature T_2 depends in this concept on the inlet gas temperature T_1 , the mass flow \dot{m} and the thermal power flow \dot{Q}_{in} . The thermal inertia of the heat exchanger and the dependence of the mass flow temperature T_2 on the mass flow itself involve great challenges regarding the dynamics of the heat exchanger. This relation is given by Eq. (2.5) for ideal gases.

$$T_2 = \frac{\frac{\dot{Q}_{in}}{\dot{m}} + c_{p,1}T_1}{c_{p,2}}. \quad (2.5)$$

In concept B_H (Fig. 2.4b), the inflowing gas stream is split into two gas paths. The upper gas stream is heated to the temperatures T_2 , the lower gas stream is cooled to the temperatures T_3 . The required outlet temperature is provided by mixing the two gas streams with different temperature in a specific ratio to reach a predefined temperature. In contrast to concept A_H ,

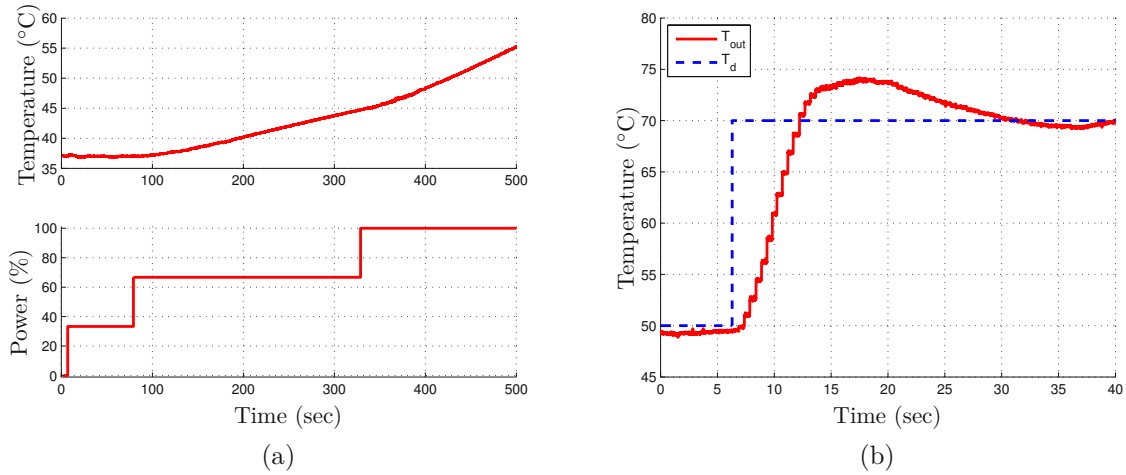


Figure 2.5: Plot (a) shows the step response of the heater. The upper subplot shows the gas temperature at the heater outlet, whereas the lower subplot shows the applied power of the heater. Plot (b) shows the step response of the concept C_H .

the output gas temperature T_4 in Fig. 2.4b, is largely unaffected by the total mass flow \dot{m} as long as the heat exchangers provide enough power to keep the temperatures T_2 and T_3 constant. In this concept, the temperature depends on the valve position $\zeta = \dot{m}_2/\dot{m}_3$ that defines the mass flow ratio of both streams. The corresponding equation is given by

$$T_4 = \frac{\zeta c_{p,2} T_2 + c_{p,3} T_3}{(\zeta + 1) c_{p,4}}, \quad \zeta = \frac{\dot{m}_2}{\dot{m}_3}. \quad (2.6)$$

Concept C_H (Fig. 2.4c) is a further development of concept B_H . The three-port valve is split up into two control valves (CV_1) and (CV_2). Further, due to the required temperature range of $40 - 80^\circ\text{C}$, the heat exchanger (HEX_2) in the colder gas path is not necessary, since the ambient temperature is below 40°C at all times. Although the availability of a colder gas would increase the temperature dynamics.

The three concepts were field-tested in the course of the test bed development. In the following, the results are summarised.

As described above, the thermal inertia of the heat exchanger and the dependence of the outflowing mass flow temperature on the mass flow itself presents a great challenge regarding the dynamics of the heat exchanger. In Fig. 2.5a, the step response of concept A_H is shown.

Due to the thermal inertia of the heater, this concept shows very slow dynamics. In comparison, by reducing these couplings with the approach taken in concept C_H , the step response can be vastly improved as shown in Fig. 2.5b. Additionally, the possibility to vary the temperature T_2 of the warmer stream up to a level of 200°C further facilitates dynamic temperature changes.

The comparison of concept B_H and concept C_H is shown in Fig. 2.6. It can be seen that the 3-Way-Valve allows only an adjustment of the temperature in the upper and lower 5% range of the valve stroke. Whereas concept C_H enables control almost over the whole range. The corresponding control of the two valves (cold and hot flow path) is given in Fig. 2.7a. To decrease the response time, the control of the two valves can further take into account the flat part in Fig. 3.9. This adaptation is shown in Fig. 2.7b.

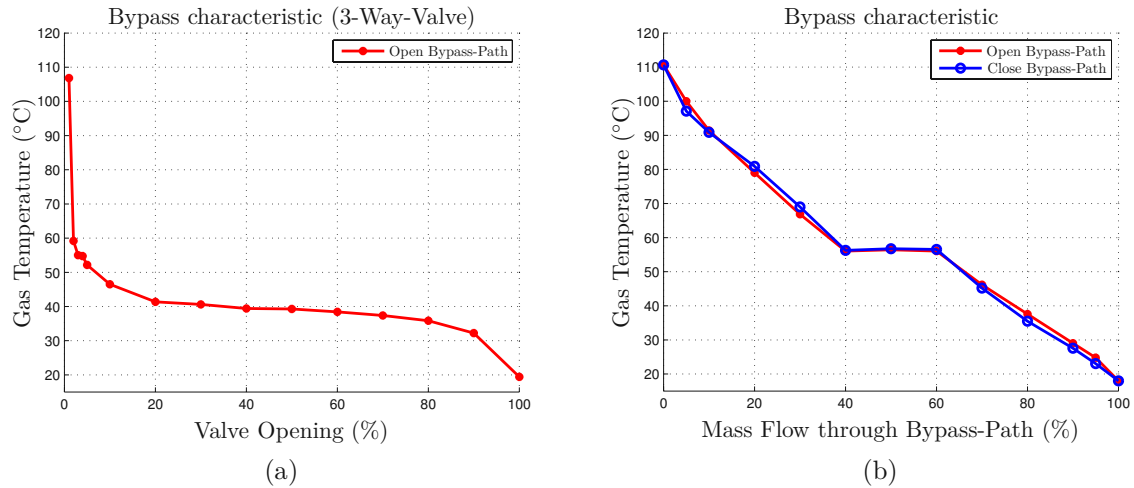


Figure 2.6: Plot (a) shows the characteristic of concept B_H obtained from stationary measurements. Plot (b) shows the characteristic of concept C_H obtained from stationary measurements.

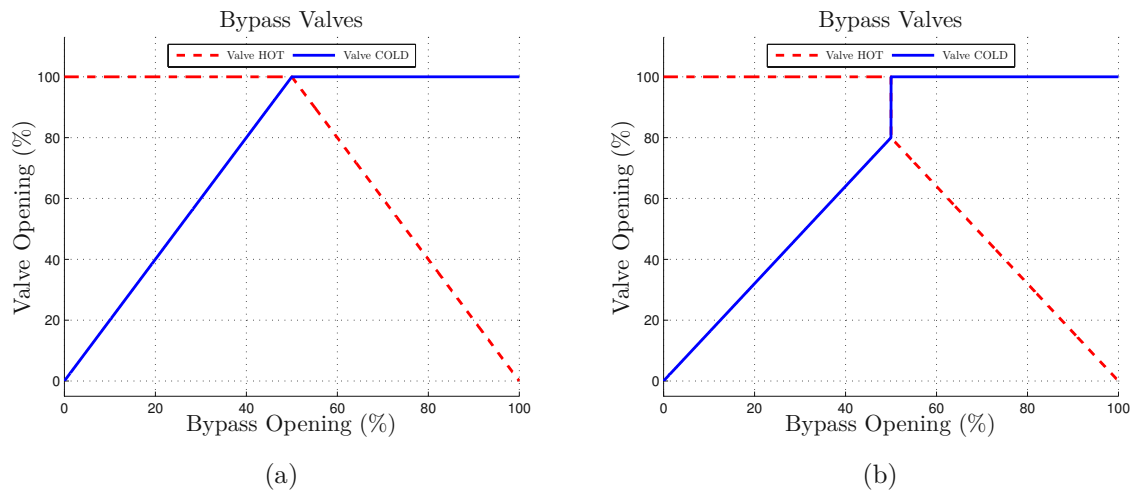


Figure 2.7: Plot (a) shows the valve positions for Bypass opening. Plot (b) shows adapted valve positions to account for the flat part in the Bypass characteristic.

In consideration of the above discussed arguments, concept C_H was chosen for further implementation in to the test bed.

2.1.3 Humidification

To decouple the thermodynamic states of the inflowing gas stream from the thermodynamic states of the outflowing gas stream in a fuel cell stack test bed, it is advantageous to not apply a gas recirculation or membrane humidifier to humidify the inflowing gas stream, which is a standard way in fuel cell applications to reuse the exhaust humidity. Therefore, various active humidification methods like saturated steam injection, liquid water injection and ultrasonic humidifiers, which are industrial standard in different applications, were evaluated theoretically with regard to the existing technical and economic boundary conditions.

The goal of the humidification process is to control the relative humidity of the gas at the fuel cell stack inlet. Since the relative humidity is a nonlinear function of the temperature and gas mass fractions, the dynamics of the humidification process is particularly important.

The main criteria for selecting a humidification process were:

- Avoid flooding of the fuel cell, which would decrease the performance. Therefore, the humidification method should not insert water droplets into the system.
- Due to different sizes of fuel cell stacks for different applications, the humidification method should be scalable to the fuel cell application.
- In order to increase the dynamic response, the process of steam production should not be affected by the current operating condition.

A comparison of liquid water injection and direct steam injection is shown in Fig. 2.8. The figure shows the Temperature-Entropy diagrams (TS-Diagram) for water. Fig. 2.8a shows the humidification process for liquid water injection. The injected water has to be evaporated, which means that the enthalpy of vapourisation has to be supplied by the gas stream. The evaporation time and, therefore, the length of travel depends on the droplet size. To reduce the droplet size, a high pressure injection with a multi-component nozzle can be applied. Compared to this, the concept of direct steam injection is shown in Fig. 2.8b. The injected steam is already in gas phase and includes the evaporation enthalpy. Further, by additionally overheating the steam, the chance of introducing water droplets into the system can be reduced.

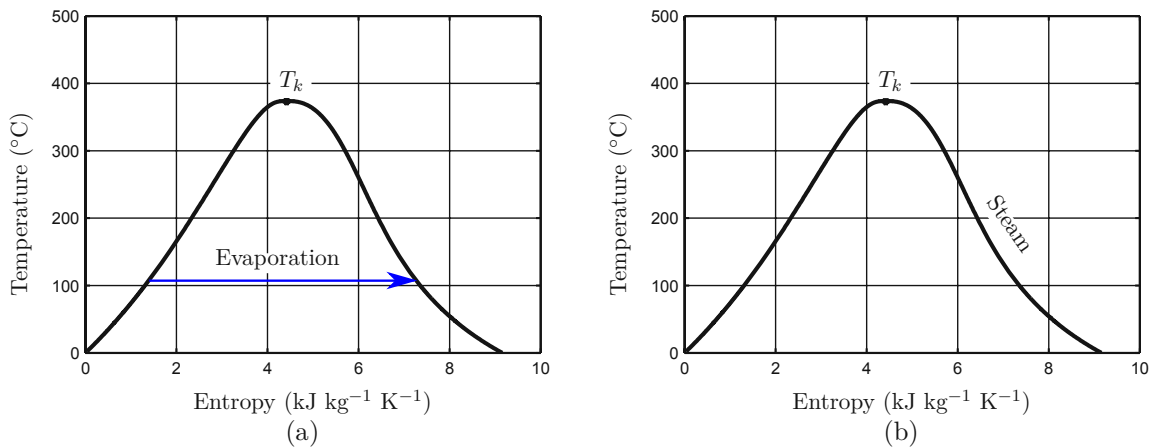


Figure 2.8: The plots show the TS-Diagram for Water. Plot (a) shows the evaporation process for liquid water injection. Plot (b) shows that for direct steam injection the evaporation enthalpy is already accounted for.

The concept of saturated steam injection fulfils the above introduced criteria. It provides the necessary steam mass flow and pressure, while at the same time having a low technical effort and lower costs compared to other methods. Furthermore, it allows a highly dynamic and precise injection of steam, and it minimises at the same time the risk of unintended droplets in the humid air. The insertion of unwanted droplets can further be reduced by overheating the saturated steam before injecting it into the system. The necessary steam mass flow is provided dynamically from an already existing steam reservoir. Therefore, the steam production is decoupled from the test bed and the current operating condition. The

steam boiler is easily scalable to the application and additionally, the steam pressure can be chosen such that for steam injection the critical pressure ratio is reached. This facilitates the control of the steam injection due to the linear characteristic of the nonlinear flow equation in that region.

In consideration of these arguments, the concept of saturated steam injection was chosen for further implementation in to the test bed.

The applied humidification method is shown in Fig. 2.9. It consists of an electrical pump P that feeds liquid water into the steam boiler (D_1). The heat exchanger (HEX) superheats the steam up to a temperature level of 160°C . Finally, the amount of steam fed to the air is controlled via a sliding gate control valve (CV). All pipes and valves are insulated and heated.

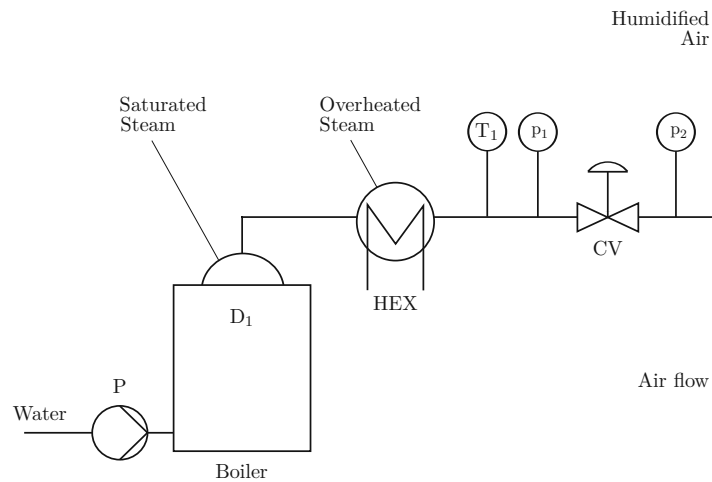


Figure 2.9: Humidification by steam boiler.

2.1.4 Back Pressure Control

The stack pressure has to be controlled in a range from 1.1 to 3 bar(a). Two concepts for backpressure control are shown in Fig. 2.10. In concept A_P (Fig. 2.10a), the pressure p_1 is adjusted by a back pressure regulator (BPC). In concept B_P (Fig. 2.10b), a sliding gate control valve (CV) is used. Here the opening area is controlled directly. Two requirements are essential for the control of the back pressure. First, the back pressure valve should not introduce additional dynamics through an underlying control loop. Second, the back pressure valve should be able to be actuated independently of the system pressure. Concept B_P fulfills both requirements, therefore it was chosen for further implementation in to the test bed.

2.1.5 Fuel Cell Stack

An applied measuring section represents the fuel cell stack as part of the hardware construction. It includes sensors for pressure p , air temperature T , humidity φ and mass flow \dot{m} . Since there is no gas recirculation or membrane humidifier, the outlet conditions do not affect the thermodynamic state at the stack inlet. Therefore, the integration of a real fuel cell stack would only result in a pressure coupling and. Hence, the fuel cell stack can be regarded as an additional pressure resistance, which is in series with the back pressure valve.

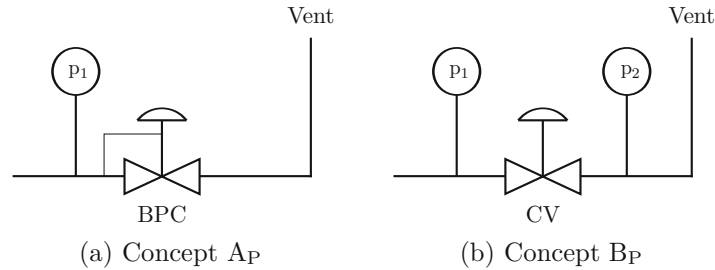


Figure 2.10: Back pressure control concepts.

2.2 Test Bed

The test bed was assembled at a test facility, which provides the necessary process gas, power connections and safety installations. The defined operating range for the cathode gas conditioning system is given in Table. 2.1.

Output	Range
System Temperature	20 – 100 °C
System Pressure	1.1 – 3 bar
Relative Humidity	0 – 100 %
Mass Flow	0 – 70 kgh ⁻¹

Table 2.1: System operating range.

Based on the defined operating range, the evaluated actuator ranges are given in Table. 2.2. The ranges are derived from stationary energy and flow calculations for the defined operating range and limitations imposed by the test facility.

Concept	Quantity	Range
Flow Control A _F	Gas Mass Flow	0 – 40 kgh ⁻¹
Heating C _H	Gas Temperature	0 – 120 °C
Humidification	Steam Mass Flow	0 – 30 kgh ⁻¹
Back Pressure Control B _P	Opening Area	0 – 2 cm ²

Table 2.2: Operating ranges and quantities that the different concepts should provide.

2.2.1 Test Bed Construction

Based on the evaluation in Section 2.1 the piping and instrumentation diagram (P&ID) of the cathode gas conditioning system is shown in Fig. 2.11. Although different hardware designs for the subsystems flow control, thermal management, humidification and back pressure control can be chosen, this design was chosen in order to provide the system with the most dynamic actuators.

The realised hardware setup was built modular and with sufficient piping. This ensured fast prototype and enabled on-site changes of modules, while reducing the downtime of the test bed. For a finalised product, the hardware setup can be realised in a much compacter design, which would increase the dynamic response of the test bed.

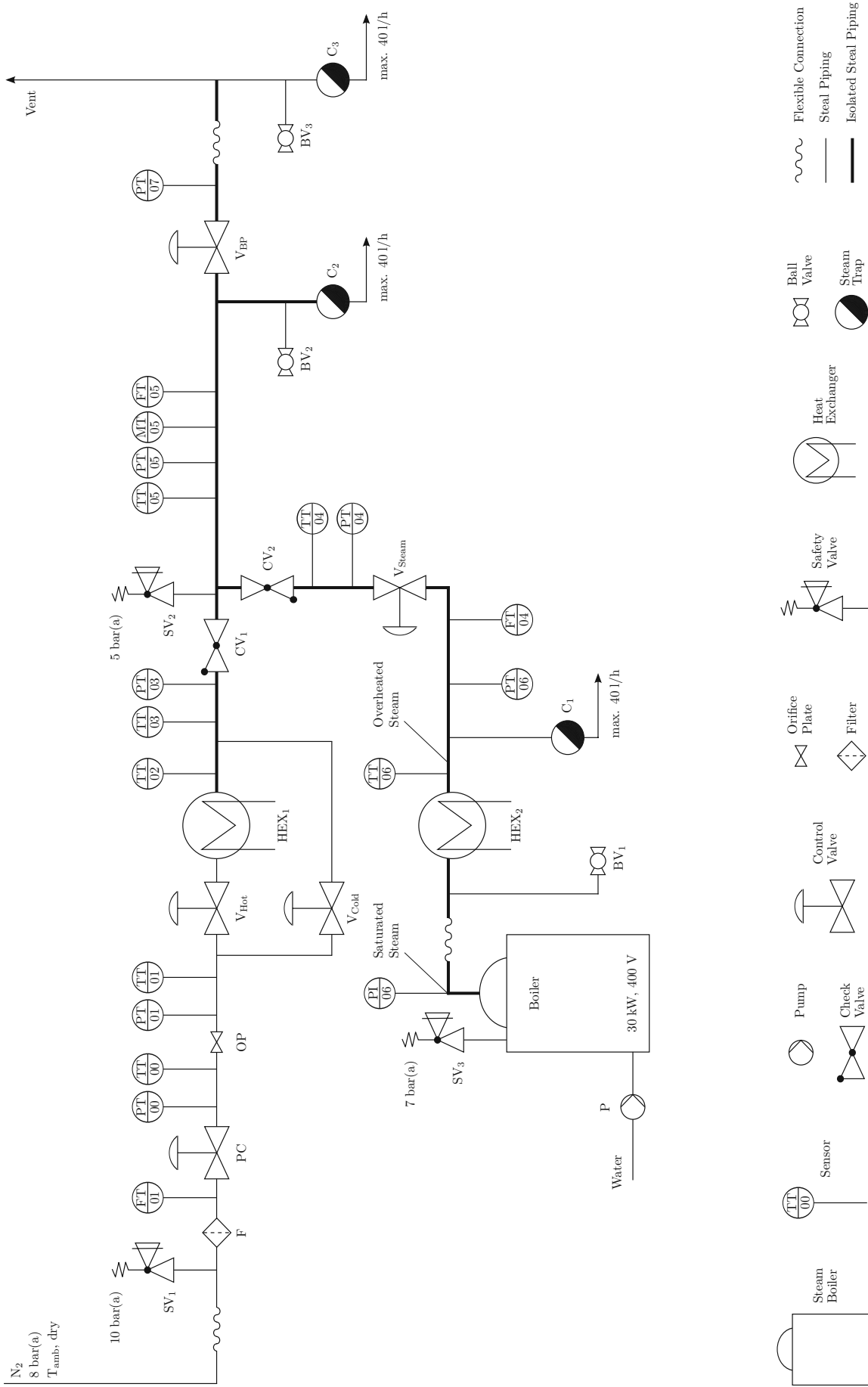


Figure 2.11: Piping and instrumentation diagram of cathode gas conditioning system.

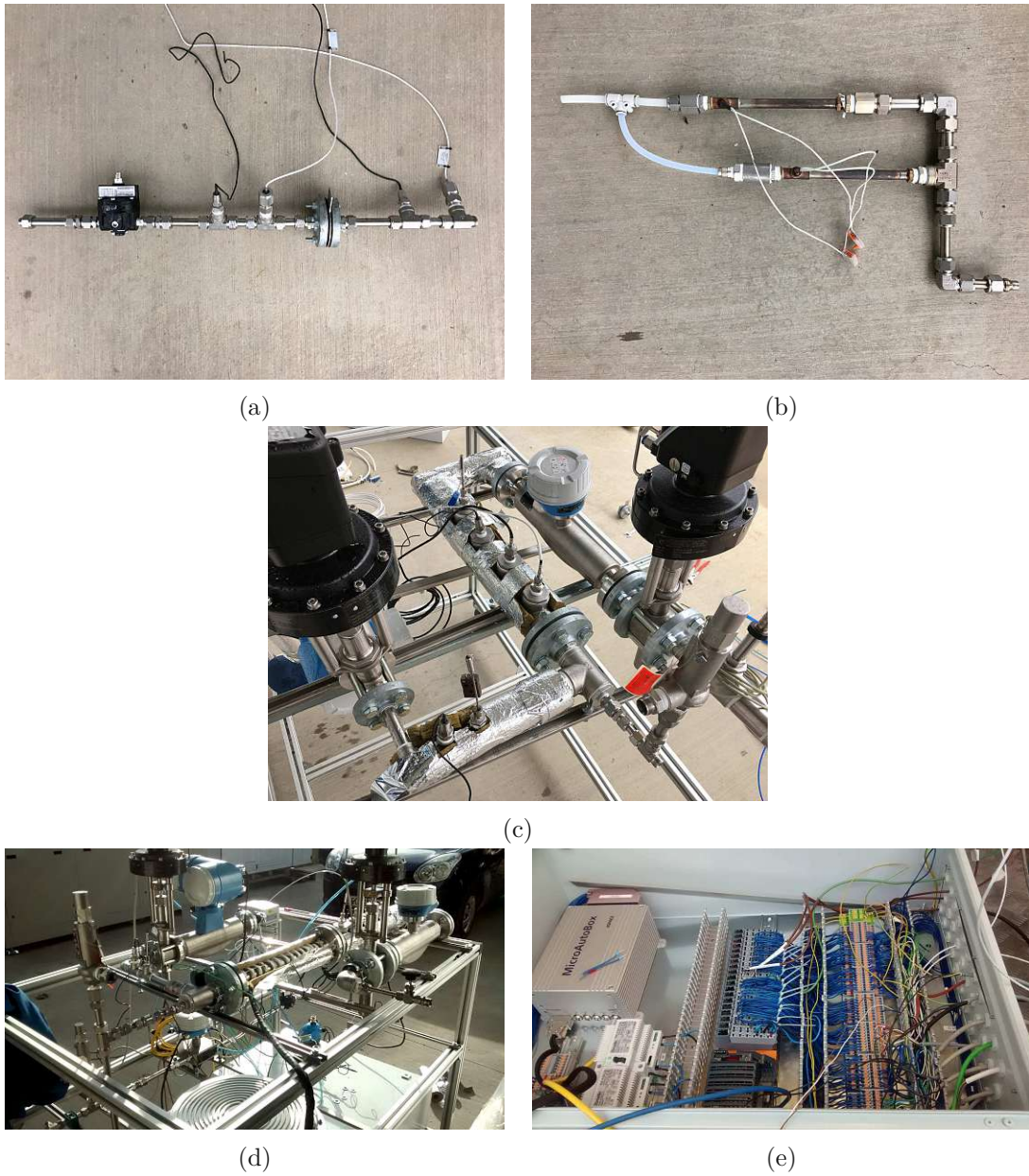


Figure 2.12: The figures show the applied hardware components for the realised hardware setup. In Fig. (a), the concept A_F with the pressure controller (PC), orifice plate (OP) and the sensors are shown. In Fig. (b), the gas heating elements are shown. In Fig. (c), the steam valve, backpressure valve and applied measuring section are shown. In Fig. (d), the overall hardware setup is shown and in Fig. (e), the real-time capable MicroAutoBox II with a programmable logic controller is shown, which has been used to implement the designed control algorithms.

Additionally to the described concepts, some safety measures were included into the hardware design. Namely, safety valves in different parts of the system to prevent an overpressure, which could damage the system, check valves to prevent the different gas path to be floated with other gases and steam traps to drain unwanted liquid water from the system. This is particularly needed during the start up procedure of the system. Additional ball valves were built-in to enable manual draining of the system.

The applied hardware components for the realised hardware setup are shown in Fig. 2.12. In Fig. 2.12a, the concept A_F , as discussed in Section 2.1.1, is shown. From left to right: pressure controller (PC), followed by temperature and pressure sensors, orifice plate (OP), which is followed by another temperature and pressure sensors. In Fig. 2.12b, the gas heating elements are shown. Two heating elements were connected parallel to supply the required thermal energy. Each of the heating elements supplies 400 W of thermal power. In Fig. 2.12c, the steam valve (on the left), the backpressure valve (on the right) and the applied measuring section is shown. The later consists of two temperature sensors, a pressure sensor, a relative humidity sensor and a coriolis sensor for the mass flow measurement. Fig. 2.12d shows the overall hardware setup, which was assembled on a rack. Fig. 2.12e shows the applied electronics, the real-time capable MicroAutoBox II and the programmable logic controller, which have been used to control the system.

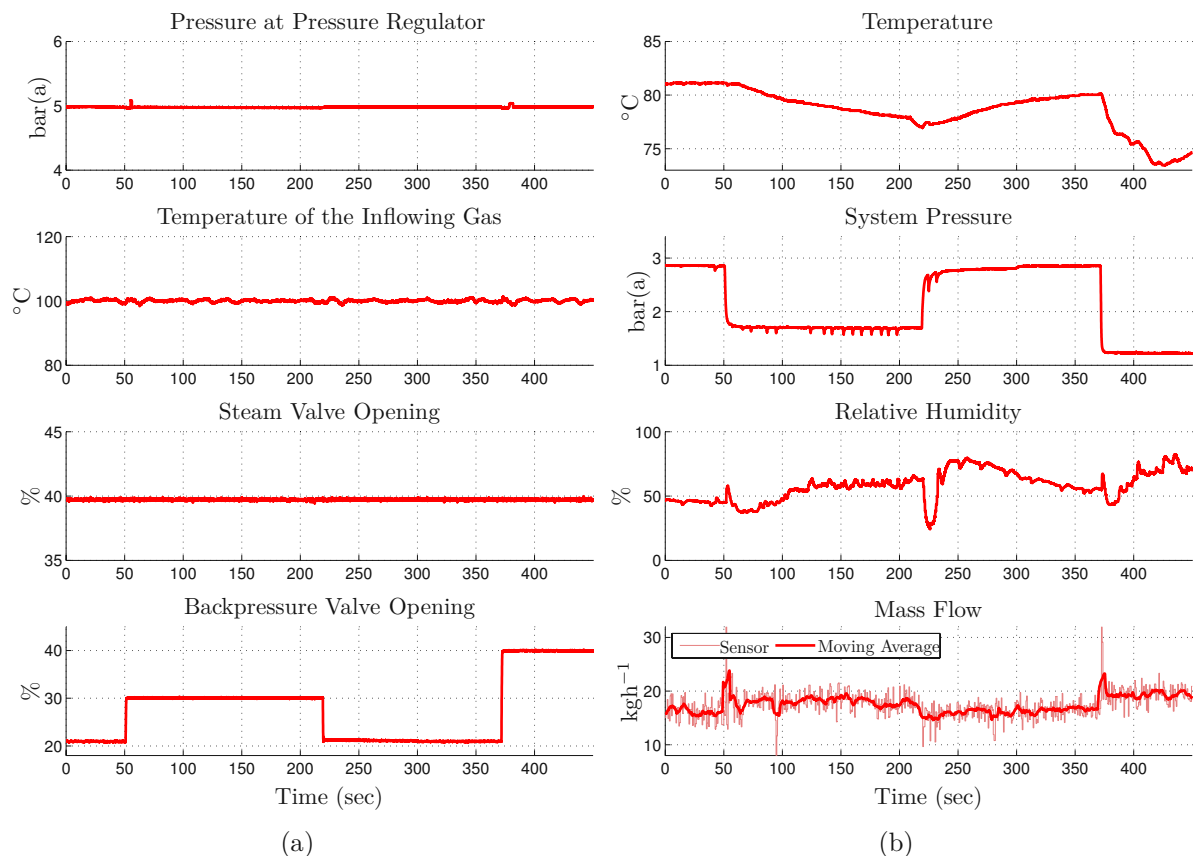


Figure 2.13: The measured step response of the system shows coupling of the system outputs. Plot (a) shows the sensor signals of the input variables, and plot (b) shows the measured step response of the system outputs. The variation of one input has an effect on all four outputs.

2.2.2 Test Bed Coupling

The realised system has multiple inputs and multiple outputs (MIMO). In Fig. 2.13, a measured step response of the test bed is shown.

The control variables are shown in Fig. 2.13a. It can be seen that the first three control variables are kept constant while the opening of the backpressure valve is varied. The effect of the variation of this single input on the multivariate system is shown in Fig. 2.13b. The plot shows that the thermodynamic quantities (pressure, temperature, relative humidity and mass flow) are physically coupled by various relations, and thus changing one quantity affects the others.

Due to the nonlinearity and the coupling of the system, linear control methods are not applicable. Especially not for transient control, which is the main requirement for a dynamic fuel cell test bed. Therefore, in Section 3 a dynamic nonlinear model of the realised system is derived. Based on this dynamic model, a model-based nonlinear multivariate control concept, which deals with the coupling of the thermodynamic quantities, is presented in Section 4.

Chapter 3

System Description and Modelling

In the following, a dynamic system model is derived from the hardware concept introduced in Section 2.1. The model will be used in Section 4 to introduce a model-based nonlinear multivariate control concept, which enables transient control of the fuel cell stack test bed. Therefore, the derived model has to include the essential dynamic properties and nonlinearities of the system. On the other hand, the system model has to have a manageable model complexity and fulfil certain criteria to be applied for control purposes. Further, the derived model has to be parameterised with measurements on the test bed to yield a valid system model.

3.1 Dynamic Model of Test Bed

The derivation of the dynamic system model is based on the hardware setup introduced in Section 2.1. A schematic block diagram is shown in Fig. 3.1. The hardware components described in Section 2.1 are represented by the blocks *Gas* (Concept A_F, Fig. 2.2a), *Heater* (Concept C_H, Fig. 2.4c) and *Steam* (Fig. 2.9).

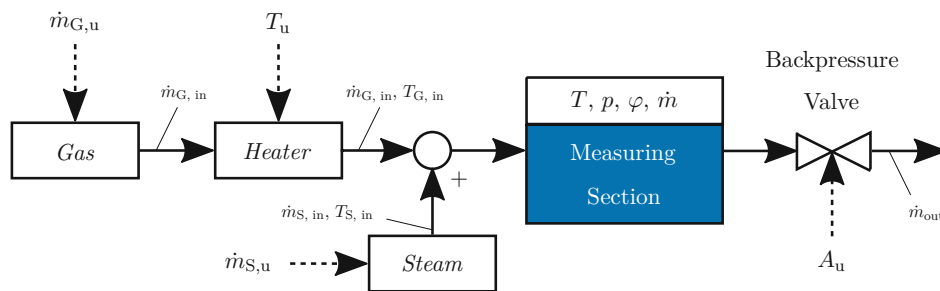


Figure 3.1: Schematic block diagram of dynamic gas conditioning system model.

This schematic is the basis for the derivation of the system model and further, for the design of the nonlinear control concept in Section 4.

3.1.1 Describing System Equations

From the schematic given in Fig. 3.1, the system dynamics can be derived. The total gas mass in the system is defined by

$$m = m_G + m_S, \quad (3.1)$$

where m_G represents the gas mass and m_S the steam mass. The mass balance equations of the gas components are given by

$$\frac{d}{dt}m_G = \dot{m}_{G, \text{ in}} - \dot{m}_{G, \text{ out}}, \quad (3.2)$$

$$\frac{d}{dt}m_S = \dot{m}_{S, \text{ in}} - \dot{m}_{S, \text{ out}}, \quad (3.3)$$

where the first terms represent the inflowing mass streams, and the second terms represent the outflowing mass streams. The outflowing gas streams are given by the mass fraction of the total outflowing mass stream

$$\dot{m}_{G, \text{ out}} = \frac{m_G}{m} \dot{m}_{\text{ out}}, \quad (3.4)$$

$$\dot{m}_{S, \text{ out}} = \frac{m_S}{m} \dot{m}_{\text{ out}}, \quad (3.5)$$

where $\dot{m}_{\text{ out}}$ is modelled by the nonlinear flow equation given by Eq. (2.1). For completeness, the equation is quoted again. A full derivation of the nonlinear flow equation is given in the Appendix (B.3).

$$\dot{m}_{\text{ out}} = A p_1 \sqrt{\frac{2}{RT_1}} \psi, \quad (3.6)$$

with

$$\psi = \sqrt{\frac{\kappa}{\kappa - 1} \left(\Pi^{\frac{2}{\kappa}} - \Pi^{\frac{\kappa+1}{\kappa}} \right)}, \quad \Pi = \frac{p_2}{p_1}, \quad \kappa = \frac{c_p}{c_v}. \quad (3.7)$$

The function ψ has its maximum value at the so-called critical pressure ratio, which is given by

$$\Pi_{\text{crit.}} = \left(\frac{p_2}{p_1} \right)_{\text{crit.}} = \left(\frac{2}{\kappa + 1} \right)^{\frac{\kappa}{\kappa - 1}}. \quad (3.8)$$

From this, $\psi_{\text{ max}}$ for the critical flow derives as

$$\psi_{\text{ max}} = \left(\frac{2}{\kappa + 1} \right)^{\frac{1}{\kappa - 1}} \sqrt{\frac{\kappa}{\kappa + 1}}. \quad (3.9)$$

The energy balance equation for the system is given by

$$\frac{dU}{dt} = \dot{m}_{G, \text{ in}} h_{G, \text{ in}} + \dot{m}_{S, \text{ in}} h_{S, \text{ in}} - \dot{m}_{\text{ out}} h_{\text{ out}}, \quad (3.10)$$

$$\frac{dU}{dt} = \frac{d}{dt}(m_G u_G + m_S u_S), \quad (3.11)$$

where U is the internal energy of the system, $h_{G, \text{ in}}$ is the specific enthalpy of the inflowing gas, $h_{S, \text{ in}}$ is the specific enthalpy of the inflowing steam, $h_{\text{ out}}$ is the specific enthalpy of the outflowing gas mixture and u_G and u_S represent the specific internal energy of the gas and steam, respectively.

With Eq. (3.4) and Eq. (3.5) the outflowing enthalpy stream in Eq. (3.10) can be written as

$$\dot{m}_{\text{out}} h_{\text{out}} = \frac{1}{m} \dot{m}_{\text{out}} (m_G h_{G,\text{out}} + m_S h_{S,\text{out}}). \quad (3.12)$$

By inserting the specific internal energy into Eq. (3.11) and assuming constant specific heat capacities c_p and c_v one obtains

$$\begin{aligned} \frac{d}{dt} (m_G u_G + m_S u_S) &= \left(\frac{d}{dt} m_G \right) c_{v,G} T + \left(\frac{d}{dt} m_S \right) (c_{v,S} T + r_0) \\ &+ \left(\frac{d}{dt} T \right) (m_G c_{v,G} + m_S c_{v,S}), \end{aligned} \quad (3.13)$$

where T is the temperature in the system, $c_{v,G}$ and $c_{v,S}$ are the specific heat capacities at constant volume, $c_{p,G}$ and $c_{p,S}$ are the specific heat capacities at constant pressure and r_0 is the latent heat of steam. Combining this with Eq. (3.10), one obtains

$$\begin{aligned} \frac{d}{dt} T &= \frac{1}{m_G c_{v,G} + m_S c_{v,S}} \\ &\cdot \left(\dot{m}_{G,\text{in}} c_{p,G} T_{G,\text{in}} + \dot{m}_{S,\text{in}} (c_{p,S} T_{S,\text{in}} + r_0) \right. \\ &- \frac{1}{m} \dot{m}_{\text{out}} (m_G c_{p,G} T + m_S (c_{p,S} T + r_0)) \\ &\left. - \frac{d}{dt} m_G c_{v,G} T - \frac{d}{dt} m_S (c_{v,S} T + r_0) \right), \end{aligned} \quad (3.14)$$

where $T_{G,\text{in}}$ is the temperature of the inflowing gas mass stream, $T_{S,\text{in}}$ is the temperature of the inflowing steam mass stream. This represents the describing state equation for the system temperature. A full derivation of the above equation is given in Appendix B.2.

The system pressure p can be determined by using the ideal gas law

$$pV = (m_G R_G + m_S R_S) T, \quad (3.15)$$

where V represents the volume and R_G and R_S are the gas constants of the gas and steam, respectively. In this equation, the volume also accounts for the piping in the system. Therefore, by changing the piping volume, the dynamics of the system will be affected.

The relative humidity in the system is given by

$$\varphi = \frac{X}{\frac{R_G}{R_S} + X} \cdot \frac{p}{p_W^s(T)}, \quad X = \frac{m_S}{m_G}, \quad (3.16)$$

where X represents the vapour content in the gas, and $p_W^s(T)$ represents the saturation partial pressure given by Magnus' formula

$$p_W^s(T) = p_m e^{\frac{C_1 \cdot T}{C_2 + T}}. \quad (3.17)$$

The parameters p_m , C_1 and C_2 for Eq. (3.17) are taken from Ref. [37]. Here, instead of the relative humidity, it would also be possible to regard the dew point temperature as system output.

Additionally, it has to be noted that Eq. (3.16) is an algebraic relation and, therefore, does not contribute to the dynamics of the system model. Although Eq. (3.6) and Eq. (3.15)

are also algebraic relations and similarly system outputs, they enter the system dynamics through Eq. (3.4) and Eq. (3.5) and, therefore, contribute to the dynamic behaviour of the system model.

The actuator dynamics are included in the system model as first order lag elements with time constants τ_{1-4} . These additional differential equations are given by

$$\tau_i \frac{d}{dt} \xi_i = (\xi_i - u_i), \quad i = 1, \dots, 4 \quad (3.18)$$

with

$$\xi = [\dot{m}_{G, \text{ in}}, T_{G, \text{ in}}, \dot{m}_{S, \text{ in}}, A_{\text{Nozzle}}]^T, \quad (3.19)$$

$$u = [\dot{m}_{G, \text{ u}}, T_{\text{u}}, \dot{m}_{S, \text{ u}}, A_{\text{u}}]^T, \quad (3.20)$$

where A_{Nozzle} represents the nozzle opening of the backpressure valve and u represent the input variables for the *Gas* block, *Heater* block, *Steam* block and backpressure valve shown in Fig. 3.1.

The above derived equations represent a multivariate nonlinear system model for the test bed discussed in Section 2.1. They can be written in compact form as

$$\dot{x} = f(x, u), \quad (3.21a)$$

$$y = h(x), \quad (3.21b)$$

where the state vector x , input vector u and output vector y are given by

$$x = \begin{bmatrix} m_G \\ m_S \\ T \\ \xi \end{bmatrix}, \quad u = \begin{bmatrix} \dot{m}_{G, \text{ u}} \\ T_{\text{u}} \\ \dot{m}_{S, \text{ u}} \\ A_{\text{u}} \end{bmatrix}, \quad y = \begin{bmatrix} T \\ p \\ \varphi \\ \dot{m}_{\text{out}} \end{bmatrix}. \quad (3.22)$$

Whereas Eq. (3.21a) consist of the coupled set of differential equations given by Eq. (3.2), Eq. (3.3), Eq. (3.14) and Eq. (3.18). The coupled output equations Eq. (3.21b) consist of the algebraic relationships for temperature, pressure, relative humidity and mass flow and do not contribute to the system dynamics described by Eq. (3.21a). The different couplings of the state and output equations represent the fact that the physical quantities at the test bed are coupled.

The described system has four input variables, four output variables and seven states. Whereas four states are first order lag elements, describing the actuator dynamics, and the remaining three states are describing the thermodynamic properties of the system. This derived system model of the hardware setup will be used to design a model-based nonlinear multivariate control concept, which enables transient control of the fuel cell stack test bed. The necessity of such a controller will be highlighted in the following sections.

3.1.2 Model Modularity

The presented dynamic system model is designed in such a way that changes in the test bed hardware have a minimal effect on the model structure itself. Such hardware changes could e.g. occur due to a malfunction of an actuator, which would require replacing a valve, the steam boiler or the mass flow controller/pressure regulator. Hardware changes would also be necessary if the test bed is rescaled to a different fuel cell stack or a redesign of the test

bed is done in order to increase the system dynamics. Structurally the system model would not be affected by such changes, the only adaptation has to be done by adapting the system model to the *new* system parameters.

The implementation of the actuator dynamics as first order lag elements enables the model to be modular and easily adaptable to such hardware changes. The assumption of a first order lag behaviour is a typical approach in control theory and the adaptation of a new submodule can be done by measuring the time constant of the new module and adapt the corresponding parameter in the system model. Further, the division in submodules makes the model scalable. For instance, valves can be put in parallel and controlled via a separate controller to emulate a *large* valve, which is also able to control low mass flow ranges. This can be done in order to account for large set point changes, which can not be sufficiently controlled with a single valve.

The submodules themselves are independent of each other and independent (in the sense of couplings) of the nonlinear system model. They can therefore be implemented with *low level* controllers as lookup tables, linear or nonlinear controllers, cascade controllers or multivariate cascade controllers. The implementation, which has been done on the realised test bed, is discussed in Section 5.2. The coupling of the thermodynamic states occurs on a *higher* level in the system model and therefore the *high level* nonlinear multivariate controller will deal with these couplings.

The *high level* control concept, which is introduced in Section 4, is based on the presented system model. Since the model consists of submodules, which are independent of the realised hardware implementation, the control concept itself will therefore be independent of the realised hardware implementation.

3.1.3 Model Couplings and Nonlinearities

The system equations given by Eq. (3.21) are coupled through various relations. This leads to the fact that one input variable can not be associated straight forward with one output variable. By changing one input variable, all the output variables are affected in one or another way. These effects impact the system on different levels. These levels can be categorised in to three classes: First, the input-to-state behaviour. Second, the state-to-output behaviour. Third, the input-to-output behaviour. Whereas the last two levels give the most insight into the system and are therefore further discussed below.

The two state-to-output nonlinearities are the outflowing mass stream \dot{m}_{out} and the relative humidity φ . The first has already been discussed in Section 2.1.1 for the design of the hardware setup. The second algebraic output nonlinearity is illustrated in Fig. 3.2. The plot shows the relative humidity Eq. (3.16) as function of the temperature T and the steam mass m_S , while the pressure p and the gas mass m_G are kept constant. This not only illustrates the nonlinear output function, but also highlights the high steam volume requirements for a fuel cell stack. Due to the fact that the required steam, for a certain relative humidity, grows exponentially, the scaling of the steam subsystem in Section 2.1.3 has to take into account the maximum steam demand for the operating range defined in Table 2.1. This can be a limiting factor for a fuel cell stack test bed. For example, at 95 % relative humidity almost twenty times as much water is needed if the outlet temperature is doubled from 45 °C to 90 °C.

The input-to-output behaviour is illustrated in two ways. First, a classical input-output evolution along the time axis is discussed. Second, a high dimensional input-output space

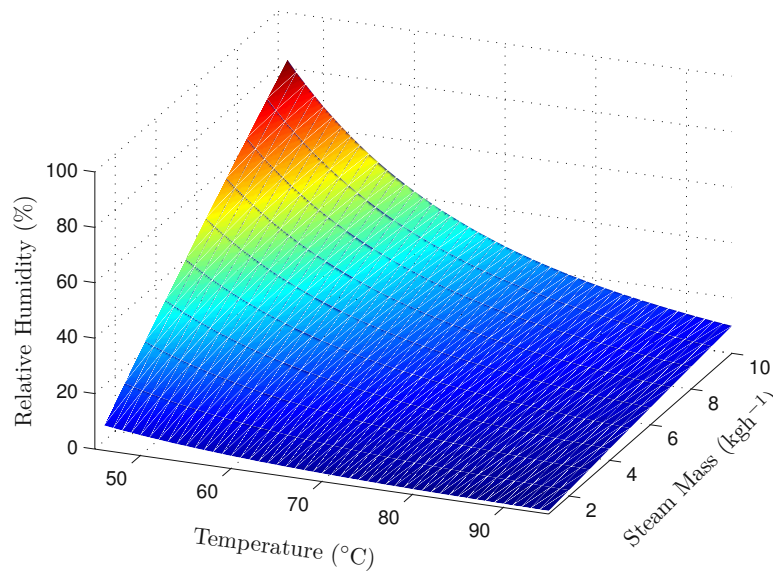


Figure 3.2: The figure illustrates the nonlinearity of the relative humidity φ given by Eq. (3.16). The variables gas mass m_G and pressure p are fixed and the function is evaluated by iterating through the steam mass m_S and the temperature T .

representation is introduced. In this representation, the nonlinearity in the input-output space can be seen and additionally, the time evolution of the resulting surfaces is depicted.

The first illustration is depicted in Fig. 3.3. The figure shows the system response for step changes of the input variables. The inputs variables u are shown in Fig. 3.3a, and the corresponding evolution of the system outputs y is shown in Fig. 3.3b. For each change of the input variables, all system outputs are affected. This is commonly understood as coupling of the system.

The second illustration of the coupling and the nonlinearity of the system is given in Fig. 3.4. In the figure, the input-to-output behaviour of the system is depicted. In the simulations, a set point change is shown, whereas the different grey surface areas illustrate the time evolution of the system with the final steady state depicted as coloured surface. For the simulation, the two input variables T_u and A_u are kept constant and the other two input variables \dot{m}_G and \dot{m}_S are varied. As illustrated in the plots, each output shows a different dynamic behaviour. This can be seen by the different dynamics of the surfaces (i.e. time evolution of the grey surface plots) in each plot. Further, the plots show the coupling of the system and illustrate the different nonlinear behaviours of the system outputs.

3.2 Model Stability

Since the introduced system model consists of a set of nonlinear differential equations, the property of system stability has to be analysed. Therefore, in the following a method will be introduced to analyse the stability properties of the presented model. This stability method will be expanded further in Section 4.6 and used to analyse the stability of the control concept, which will be introduced in Section 4.

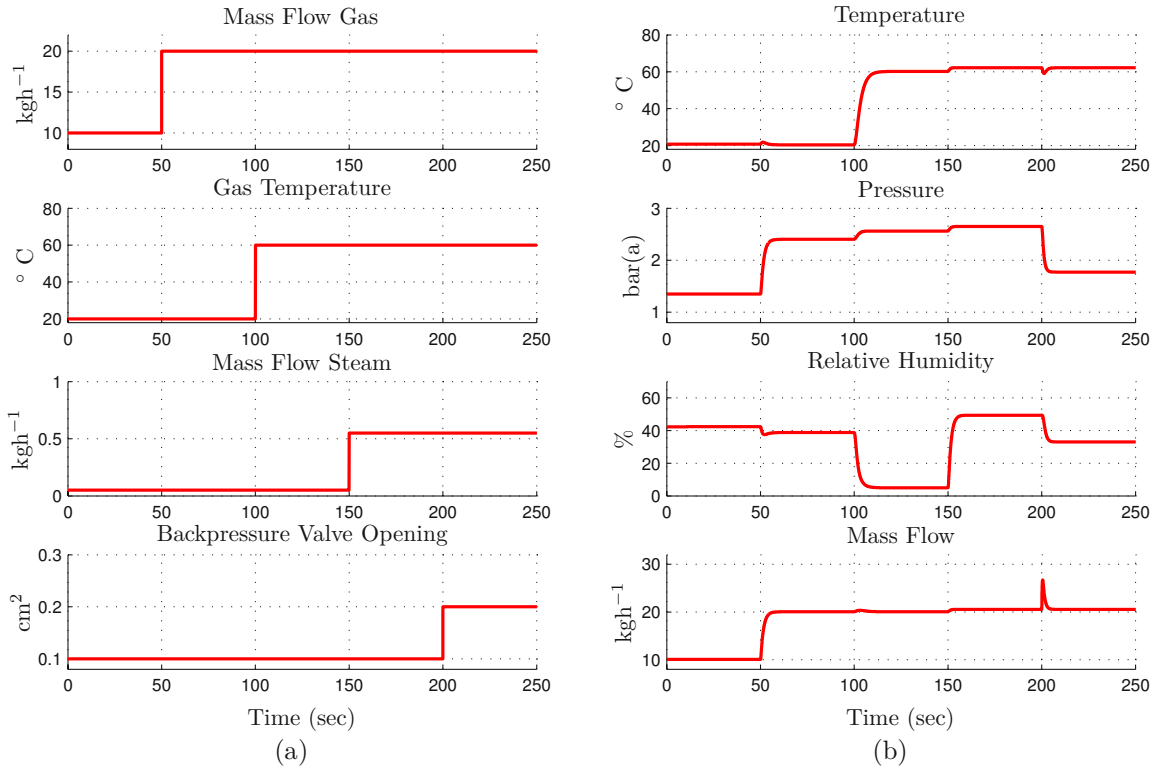


Figure 3.3: Step response of the system model. Plot (a) shows the input variables u of the system, and plot (b) shows the system outputs y .

The following theoretical considerations and definitions are based on [38,39]. The full derivations, proofs and further readings can be found in the quoted literature.

3.2.1 Lyapunov Stability Analysis

The Lyapunov stability theory was introduced in 1892 by A. M. Lyapunov [40,41] and has since then found its way into a wide field of applications [42–44]. The Lyapunov method analyses system stability in the sense of stability of equilibrium points. An equilibrium point is stable if all solutions starting at a nearby point stay nearby. If not, it is unstable. Further, it is asymptotically stable if all solutions starting at a nearby point not only stay nearby (e.g. orbit around the equilibrium point), but converge to the equilibrium point with time progressing.

For the stability analysis, the system equation Eq. (3.21) can be regarded as an autonomous system of the form $\dot{x} = f(x)$, since the input variables u are constant for an equilibrium point.

Theorem 3.1: Let $x = 0$ be an equilibrium point for $\dot{x} = f(x)$ and $D \subset \mathbb{R}^n$ be a domain containing $x = 0$. Let $V : D \rightarrow \mathbb{R}$ be a continuously differentiable function such that

$$V(0) = 0 \quad \text{and} \quad V(x) > 0 \quad \text{in} \quad D - \{0\}, \quad (3.23)$$

$$\dot{V}(x) \leq 0 \quad \text{in} \quad D. \quad (3.24)$$

Then, $x = 0$ is stable. Moreover, if

$$\dot{V}(x) < 0 \quad \text{in} \quad D - \{0\} \quad (3.25)$$

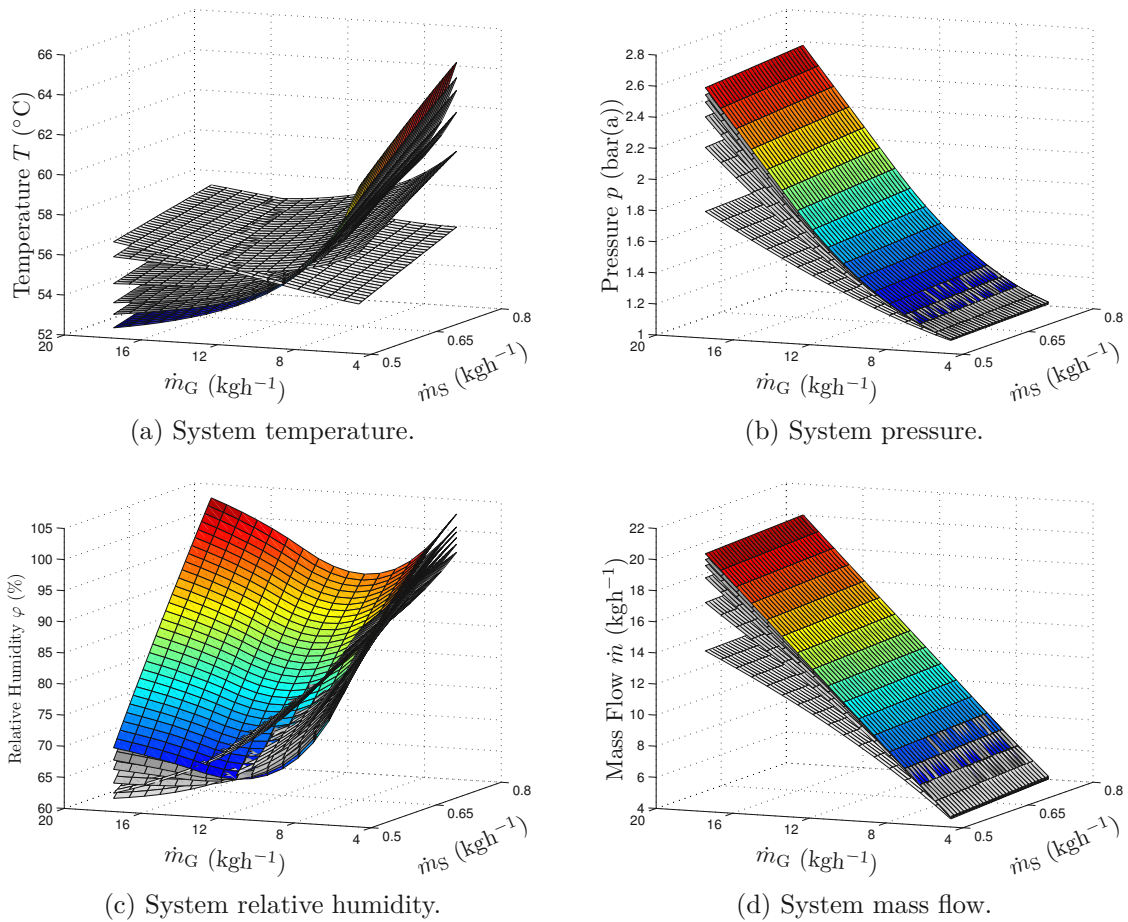


Figure 3.4: The figures show the coupled nonlinear input-to-output behaviour of the system. For the plots, a set point change was performed, where the two input variables T_u and A_u were kept constant and the other two input variables \dot{m}_G and \dot{m}_S were varied. The different grey surface areas illustrate the time evolution of the system with the final steady state as coloured surface.

then $x = 0$ is asymptotically stable.

The proof of this theorem can be found in [38]. The assumption of an equilibrium point at $x = 0$ is not a restriction of generality, because every equilibrium point can be easily transformed to $x = 0$.

If a continuously differentiable function $V(x)$ satisfies Eq. (3.23) and Eq. (3.24), it is called a *Lyapunov function*. The so called *Lyapunov Surfaces* are given by $V(x) = c$, with $c > 0$. Fig. 3.5 shows Lyapunov surfaces for decreasing values of c . The condition $\dot{V}(x) < 0$ ensures that once a trajectory crosses a Lyapunov surface $V(x) = c$ it moves inside the set $\Omega_c = \{x \in \mathbb{R}^n \mid V(x) \leq c\}$ and therefore, can never leave this set. If $\dot{V}(x) < 0$, then the trajectory continuously moves to Lyapunov surfaces with a smaller c . Therefore, the Lyapunov surface shrinks to the origin, showing that the trajectory approaches the origin as time progresses.

The Lyapunov stability conditions are only sufficient. If a Lyapunov function candidate fails to satisfy the conditions for stability or asymptotic stability, it does not mean that the equilibrium is not stable or asymptotically stable. It only means that such a stability

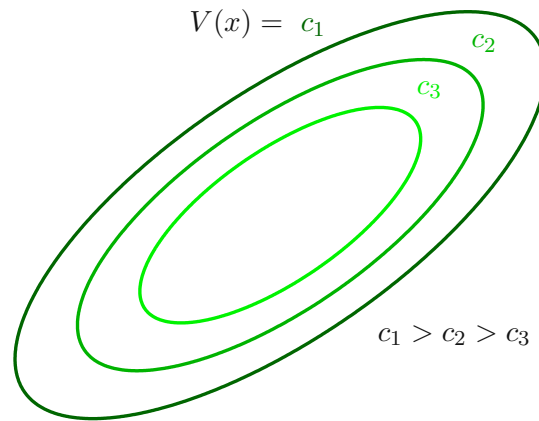


Figure 3.5: Lyapunov function surface levels.

property can not be established by using this specific Lyapunov function candidate. Lyapunov functions are sometimes difficult to find for a system, since there is no systematic method for finding these functions.

Once a Lyapunov function is found the time derivation can be written as

$$\begin{aligned}\dot{V}(x) &= \frac{d}{dt}V(x) = \sum_{i=1}^n \frac{\partial V}{\partial x_i} \dot{x}_i = \sum_{i=1}^n \frac{\partial V}{\partial x_i} f_i(x) \\ &= \left[\frac{\partial V}{\partial x_1}, \frac{\partial V}{\partial x_2}, \dots, \frac{\partial V}{\partial x_n} \right] \begin{bmatrix} f_1(x) \\ f_2(x) \\ \vdots \\ f_n(x) \end{bmatrix} = \frac{\partial V}{\partial x} f(x),\end{aligned}\quad (3.26)$$

which utilises $\dot{x} = f(x)$. This can be used to check if $\dot{V} \leq 0$. The application of Eq. (3.26) does not require the solution of the differential equation, which often can not be determined analytically for nonlinear systems. The *direct use* of the differential equations to get the derivative of the Lyapunov function gives the method its name - *direct method of Lyapunov*.

For a linear system $\dot{x} = Ax$, where A is a *Hurwitz matrix*, a quadratic Lyapunov candidate can be written as

$$V(x) = x^T P x, \quad (3.27)$$

where P is a real symmetric positive definite matrix. The derivative of V along the trajectories is given by

$$\begin{aligned}\dot{V}(x) &= x^T P \dot{x} + \dot{x}^T P x \\ &= x^T (PA + A^T P) x \\ &= -x^T Q x,\end{aligned}\quad (3.28)$$

where Q is a symmetric matrix defined by

$$PA + A^T P = -Q. \quad (3.29)$$

If Q is positive definite, then $\dot{V} < 0$ and the system is asymptotically stable. Eq. (3.29) is called *Lyapunov Equation*. Although the Lyapunov equation provides a method to analyse

the stability of a linear system, its main advantage is that it can also be applied in the stability analysis of nonlinear systems, e.g. if the right-hand side of $\dot{x} = Ax$ is perturbed, whether such perturbation is a linear perturbation in the coefficients of A or a nonlinear perturbation. This will be used in the Section 4.6, where a method to analyse the stability of the closed loop system is introduced.

3.2.2 System Model Analysis

For the system model stability only the first three states are considered. The remaining states of the system are first order lag elements and therefore, do not contribute to this analysis. As a Lyapunov function candidate, a quadratic function is used. To apply Theorem 3.1, the states have to be transformed to new coordinates. This is done by simply shifting the state vector by its steady state value. Hence, the new states are given by $\bar{x} = x - x^{\text{ss}}$, where the steady state values x^{ss} can be shifted through changing the input variables u of the system. This can also be interpreted as a set point change of the nonlinear system. With these new variable, the Lyapunov function candidate can be written as

$$\begin{aligned} V(\bar{x}) &= \bar{x}^T P \bar{x} \\ &= p_{1,1}(x_1 - x_1^{\text{ss}})^2 + p_{2,2}(x_2 - x_2^{\text{ss}})^2 + p_{3,3}(x_3 - x_3^{\text{ss}})^2, \quad p_{i,j} = 0, \quad \forall i \neq j \end{aligned} \quad (3.30)$$

with the parameters $p_{1,1}$, $p_{2,2}$ and $p_{3,3}$ given in Table 3.1. The time derivative of the Lyapunov function is given by

$$\dot{V}(\bar{x}) = \frac{dV}{dt} = \frac{\partial V}{\partial \bar{x}} f(\bar{x}) \leq 0, \quad (3.31)$$

which utilises the right-hand side of $\dot{x} = f(x)$. Since $f(x)$ is highly nonlinear and the states are coupled through various relations, the evaluation can only be performed numerically. The numerical evaluation shows that in the given operating range, furthermore for $x_1, x_2, x_3 > 0$, $\dot{V} < 0$ is ensured. This agrees with the thermodynamic properties of the system. Since each deviation of the states from the thermodynamic equilibrium has either less or more energy than currently supplied to the system, the system would converge to the equilibrium point. In the former case, the states would converge by absorbing the supplied energy from the inflowing mass stream, in the latter case, the surplus energy would be transported out of the system by the outflowing mass stream. This consideration was also the basis for choosing this mathematical structure (i.e. quadratic difference to thermodynamic steady state) for the Lyapunov function candidate in Eq. (3.30).

Parameter	Value
$p_{1,1} = p_{2,2}$	10^8
$p_{3,3}$	1

Table 3.1: Lyapunov function parameters.

In Fig. 3.6, the state evolution of the nonlinear system for a set of set point changes is shown. The trajectory colours indicate the value of the Lyapunov function (evaluation of Eq. (3.30)) at the given coordinates. The system boundaries are indicated by grey surface areas and consist of the upper and lower pressure boundary and the dew point temperature. For convenience reasons, the temperature boundaries are not shown. These can be directly taken from the z-axis. In the left column (Fig. 3.6a, Fig. 3.6c and Fig. 3.6e) three dimensional plots are depicted, while in the right column (Fig. 3.6b, Fig. 3.6d and Fig. 3.6f) the corresponding two dimensional projections are depicted.

In Fig. 3.6a, and Fig. 3.6b, a set of set point changes to a low set point is shown. The trajectories start at a high Lyapunov function value and converge towards the low set point with decreasing values of their Lyapunov functions. Although the starting points and the end point are in the operating range of the system, the system crosses the dew point temperature during the transition. This would lead to condensation and water flooding in the real system. This must be avoided to protect the fuel cell stack.

In Fig. 3.6c, and Fig. 3.6d, a set of set point changes to a high set point is shown. Similarly to the above case, the trajectories start at a high Lyapunov function value and converge towards the high set point with decreasing values of their Lyapunov functions. During the transition one trajectory crosses the dew point temperature.

Comparing Fig. 3.6a and Fig. 3.6c, it can be seen that the change of the final set point (i.e. thermodynamic equilibrium of the system) is reflected by the shape (in particular the centre) of the Lyapunov function.

A further property of the nonlinear system is shown in Fig. 3.6e, and Fig. 3.6f, where a double set point change is depicted. This means that two set point changes are depicted in the figure. First, the system leaves the current set point. Second, the system returns back to the same set point. Here, it can be observed that the paths the system takes differ for both directions. On one path, the system states stay in the operating range, on the other path they cross the dew point temperature and condensation occurs.

The exact path the system takes, to change from one set point to another, results from the dynamics of the system equations. Therefore, the system parameters have an effect on the trajectories shape.

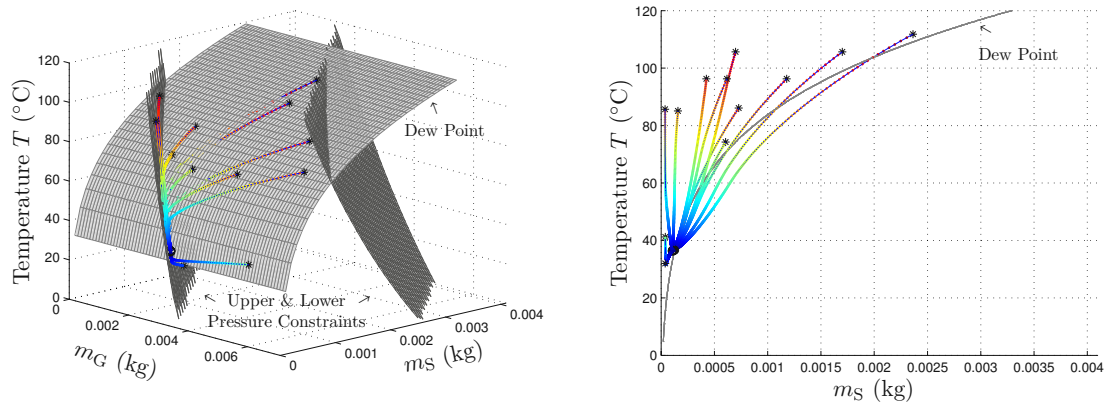
The simulation results clearly show that a set point change can lead to condensation in the system, which would reduce the fuel cell stack performance or even damage the stack. Thus, the control strategy has to consider these couplings and nonlinearities of the system and a path has to be chosen, such that the degradation of the fuel cell stack can be avoided.

3.3 Model Adaptation and Parametrisation

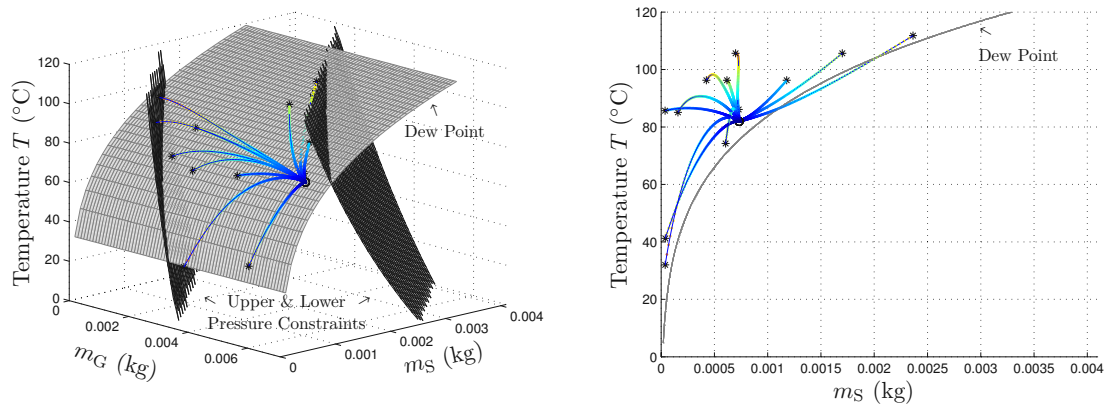
In the following the system model is slightly adapted to account for the thermal inertia of the system, the model equations are parameterised with measurements from the test bed and simulation results with different parameter sets are shown to get a qualitative understanding of the effect of the system parameters on the overall system dynamics.

3.3.1 Thermal Inertia Adaptation

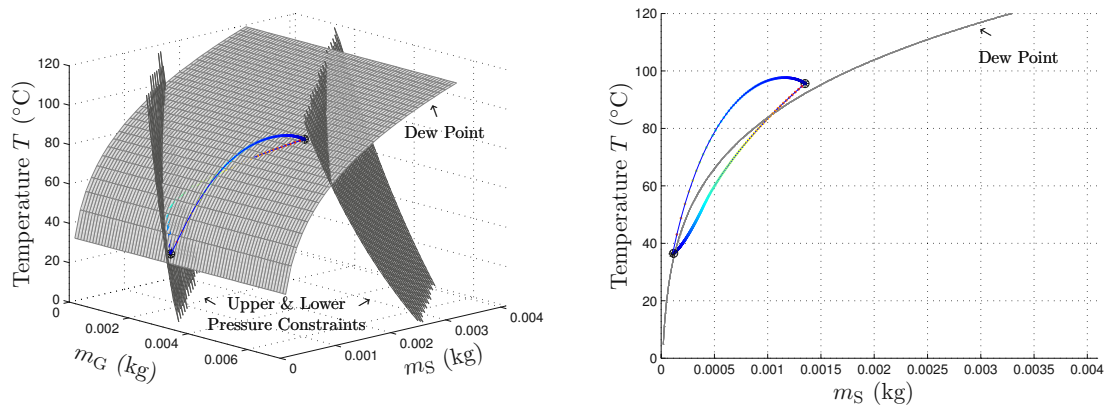
During the derivation of Eq. (3.14) the thermal inertia of the system has been neglected. Therefore, this equation has to be adapted to include the thermal inertia of the test bed. A



(a) Set point changes to low set point - 3D view. (b) Set point changes to low set point - 2D view.



(c) Set point changes to high set point - 3D view. (d) Set point changes to high set point - 2D view.



(e) Double set point change - 3D view. (f) Double set point change - 2D view.

Figure 3.6: The figures show the state trajectories for set point changes of the nonlinear system. The colour of the trajectories indicate the value of the Lyapunov function at the given point. The boundaries of the system are indicated by the grey surface areas. Fig. (a) and (b) show a set of set point changes to a low set point. Fig. (c) and (d) show a set of set point changes to a high set point. Fig. (e) and (f) show a double set point change.

straight forward possibility is to modify Eq. (3.14) as follows:

$$\begin{aligned} \frac{d}{dt}T = & \frac{1}{m_G c_{v,G} + m_S c_{v,S}} \\ & \cdot \left(\gamma_G \dot{m}_{G, \text{in}} c_{p,G} T_{G, \text{in}} + \gamma_S \dot{m}_{S, \text{in}} (c_{p,S} T_{S, \text{in}} + r_0) \right. \\ & - \frac{1}{m} \dot{m}_{\text{out}} \left(\gamma_G m_G c_{p,G} T + \gamma_S m_S (c_{p,S} T + r_0) \right) \\ & \left. - \gamma_G \frac{d}{dt} m_G c_{v,G} T - \gamma_S \frac{d}{dt} m_S (c_{v,S} T + r_0) \right), \end{aligned} \quad (3.32)$$

where γ_G and γ_S are additional factors introduced to the gas component and the steam component, respectively. These factors account for the thermal inertia of the system, which arises mainly from the hardware realisation of the test bed (e.g. piping material and cross sections/volume). The introduced γ factors can be thought of as modified time constants for the differential equation.

3.3.2 Model Parametrisation

To yield a valid system model the derived equations have to be parameterised with measurements on the test bed. This is done by a combination of physical parameters taken from literature and measuring step responses of the system to various input steps and performing a multivariate optimisation offline. The so obtained parameters are listed in Table 3.2. The heat capacities $c_{p,G}$ and $c_{p,S}$ are taken from [45]. An exemplary step response of the system is given in Fig. 2.13. The plot clearly shows the coupling of the physical quantities in the system.

Parameter	Value
Volume	2 972.34 cm ³
T_S	106 °C
γ_G	0.003
γ_S	0.010
τ_1	0.08 sec
τ_2	2.50 sec
τ_3	0.30 sec
τ_4	0.30 sec

Table 3.2: Model parameters estimated from measurements.

The model derived in Section 3.1 has a modular design and is therefore independent of the realised hardware concepts discussed in Section 2. By replacing one submodule (e.g. heater) or implementing a different subconcept (e.g. concept B_F instead of concept A_F), the *high level* nonlinear control concept can easily be adapted by adjusting the corresponding time constant in Eq. (3.21a).

To implement the overall control concept on the realised test setup, the control variables u given by Eq. (3.22) have to be mapped to the actuator signals available at the test bed. This is done, as discussed in Section 5.2, by a combination of cascade controllers and characteristic maps obtained from measurements of the realised concepts. The submodules, as well as the

derived dynamic system model itself, need to be parameterised to yield a valid model of the test bed.

The *Gas* block in Fig. 3.1 is realised by concept A_F given in Fig. 2.2a. Therefore, the model input $\dot{m}_{G, u}$ (inflowing gas mass stream) has to be mapped to a pressure, which then can be applied as control signal to the pressure regulator.

The orifice plate in concept A_F (Fig. 2.2a) is modelled by the nonlinear flow equation given in Eq. (3.6). The opening area A of the orifice plate has been obtained by performing stationary mass flow measurements and applying an offline optimisation. The result is shown in Fig. 3.7. The different colours show the different pressure set points of the stationary measurements. The dashed lines show the fitted nonlinear flow equation with the optimised area A . By inverting the nonlinear flow equation (Eq. (3.6)), the pressure signal for the pressure regulator can be calculated as a function of the desired mass flow and the measured backpressure.

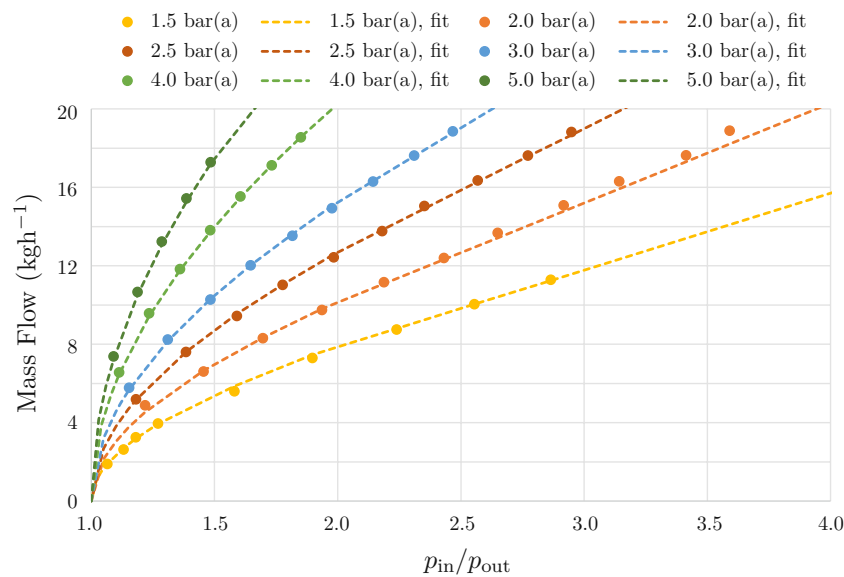


Figure 3.7: Parametrisation of nonlinear flow equation with measurements of the aperture. Plot shows measured data points and the (best) fit result.

The *Steam* block in Fig. 3.1 is realised by direct steam injection from a steam boiler as described in Section 2.1.3. Hence, the model input $\dot{m}_{S, u}$ (inflowing steam mass stream) has to be mapped to a valve, which is controlled by a control signal in the range of 0 – 100 % of the valve stroke.

The steam valve in Fig. 2.9 is modelled by Eq. (3.6). But in contrast to the orifice plate from concept A_F , the opening area A is not fixed, but can be changed by applying a different control signal to the valve. Therefore, to obtain the nonlinear opening area of the steam valve as function of the valve stroke, a set of similar measurements, as for the orifice plate, have to be performed. Each measurement provides the opening area A for the current valve stroke. To perform these measurements, the valve stroke is increased in 5 % increments and the stationary mass flow is measured. An offline optimisation calculates the opening area for the current valve stroke. To obtain the opening area as a function of the valve stroke, the points are linearly interpolated. For the steam valve, this characteristic map can further be used to calculate the valve stroke as function of the desired inflowing steam mass stream and measured pressure drop across the valve.

The *Backpressure Valve* in Fig. 3.1 (concept B_P , Fig. 2.10b) has, similarly to the steam valve, a control input in the range of 0 – 100 % of the valve stroke. Therefore, it is similarly modelled by Eq. (3.6) and by changing the valve stroke the opening area A of the valves will also change. To obtain the nonlinear opening area of the backpressure valve as function of the valve stroke, similar measurements, as for the steam valve, have to be performed. For the measurements, the valve stroke is increased in 5 % increments and the stationary mass flow is measured. An offline optimisation calculates the opening area for the current valve stroke. To obtain the opening area as a function of the valve stroke, the points are linearly interpolated. For the backpressure valve, the nonlinear opening area is directly used in the model derived in Section 3.1.

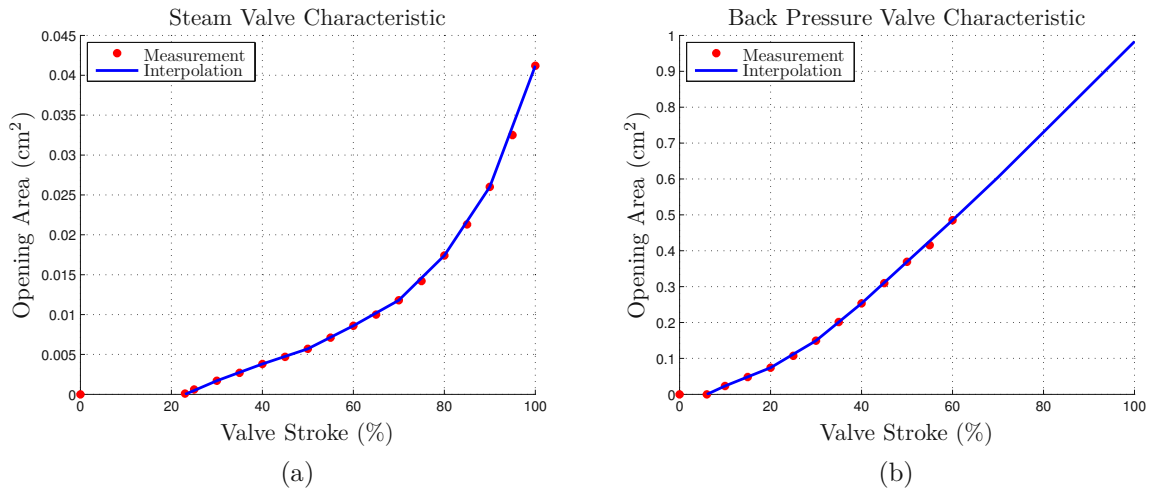


Figure 3.8: Plot (a) shows the steam valve characteristic obtained from stationary measurements. Plot (b) shows the back pressure valve characteristic obtained from stationary measurements. Measurements in (b) could only be obtained up to 60 % valve opening. The valve characteristic above this point was linearly extrapolated.

The so obtained valve characteristics are shown in Fig. 3.8. Fig. 3.8a and Fig. 3.8b show the valve characteristic of the steam valve and valve characteristic of the backpressure valve, respectively. Due to the limited mass flow at the test facility, the valve characteristic of the backpressure valve could only be obtained up to 60 % of the valve stroke. The valve characteristic above this point was linearly extrapolated. Since the mass flow was limited at the test facility, this region of the valve characteristic was not used in the further measurements.

The *Heater* block in Fig. 3.1 is realised by concept C_H given in Fig. 2.4c. As described in Section 2.1.2, the heating of the inflowing gas is implemented with a heating element, two valves and a bypass path. The different components are controlled with a cascade controller, which will be highlighted in Section 5.2. This control structure has the advantage that the components can easily be exchanged without the need to remodel and recalculate the *high level* nonlinear multivariate controller. The *Heater* block maps the inflowing gas mass temperature T_u to all the different components controlled by the former mentioned cascade controller.

For parametrisation, the heater characteristic is obtained from stationary measurements. The measurement results are shown in Fig. 3.9. The plot shows measurements for opening and for closing of the bypass-path. The hysteresis behaviour is caused by the thermal inertia of the *Heater*. To increase the temperature dynamics of the gas, the flat part in Fig. 3.9 can be eliminated by adapting the valve control of the valves in Fig. 2.4c as shown in Fig.

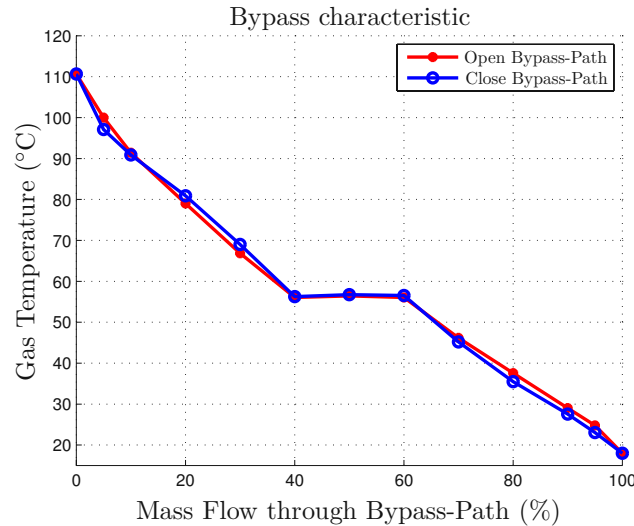


Figure 3.9: Characteristic of the *Heater* (concept C_H , Fig. 2.4c) obtained from stationary measurements. Data points taken for opening and for closing of the bypass.

2.7b. To further improve the dynamics, the characteristic map of Fig. 3.9 can be used as a feedforward signal. Since the valves implemented in the *Heater* have no feedback signal, the output temperature is given as reference value for the control signal.

The parametrisation of the dynamics of each *block* can be done by performing open loop step responses for each submodule and optimising the time constants of Eq. (3.18). Here, it is to be noted that the submodule dynamics have been modelled by first order lag elements, which is an assumption about the more complex behaviour of these modules. By having more information about the submodule dynamics, it would be possible to replace Eq. (3.18) by more complex relations. This would increase the dynamic response, but at the cost of reduced modularity of the system model and further, a reduced modularity of the nonlinear multivariate control concept.

The obtained model parameters are given in Table 3.2. Exemplary comparisons of the obtained parameterised system model with measurement data for the test bed are shown in Fig. 3.10.

3.3.3 Simulation Results

The described parameters enter into the model equations and affect the dynamic behaviour of the describing differential equations in various ways. To illustrate the effect of different system parameters on the system dynamics, a set of different system parameter variations is investigated. In Fig. 3.11, the system response to six different sets of system parameters are shown. The used deviation factors for the model parameters, which have been used to generate the step responses, are listed in Table 3.3. The parameters and deviation factors have been chosen such that the occurring impact on the system trajectories show fundamentally different effects. On a real system, or a change of more than one system parameter, these effects superimpose and can not be separated that clearly. As step response sequence, the same inputs are used as shown in Fig. 3.3a.

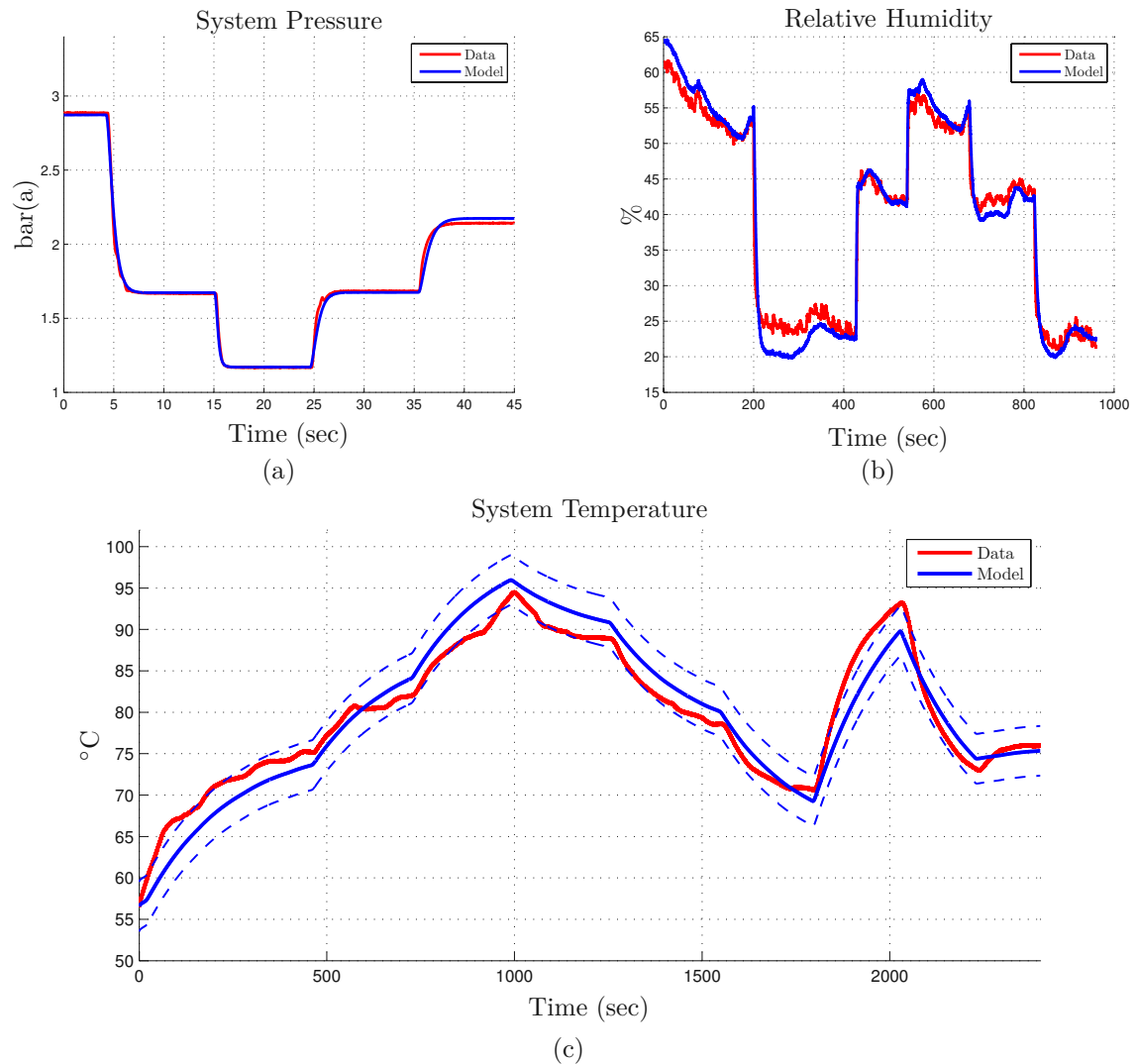


Figure 3.10: Comparison of parametrised model with measurement data. The red line shows the measured system output. The blue line shows the corresponding system model output. For the temperature, a dashed blue line indicates a $\pm 3^\circ\text{C}$ temperature band for the model output.

Trajectory	Volume (Fig. 3.11a)	T_{Steam} (Fig. 3.11b)
Red	1	1
Green	2	1.5
Blue	5	2

Table 3.3: Deviation factors of model parameters used for step response simulations of parameter varied system.

In Fig. 3.11a, the volume V of the system is changed and three different cases are investigated. The plot shows that for increasing volume (red - green - blue lines in the plots) the system dynamics is reduced. For systems with large volumes, it takes longer to reach the specified set points. The physical interpretation is the following: By increasing the volume of the system, and applying at the same time the same control inputs, the larger volume needs *longer* to be filled with gas. This results in slower pressure build-ups, slower enthalpy changes of the system (i.e. temperature), slower increase in relative humidity and slower mass flow changes. The latter is particularly affected by the slower pressure build-ups, since the outflowing mass stream depends on the pressure ratios as described by Eq. (3.6).

In Fig. 3.11b, the steam temperature $T_{S, in}$ of the system is changed and three different cases are investigated. The plot shows that for increasing steam temperature (red - green - blue lines in the plots) the system shows an offset behaviour. The physical interpretation is the following: The change of the steam enthalpy leads to an increase in the system temperature. Due to the strong coupling of the temperature to the relative humidity, the effect is largest in this two outputs. The system pressure is marginally affected, since it is immediately compensated by a change in mass flow.

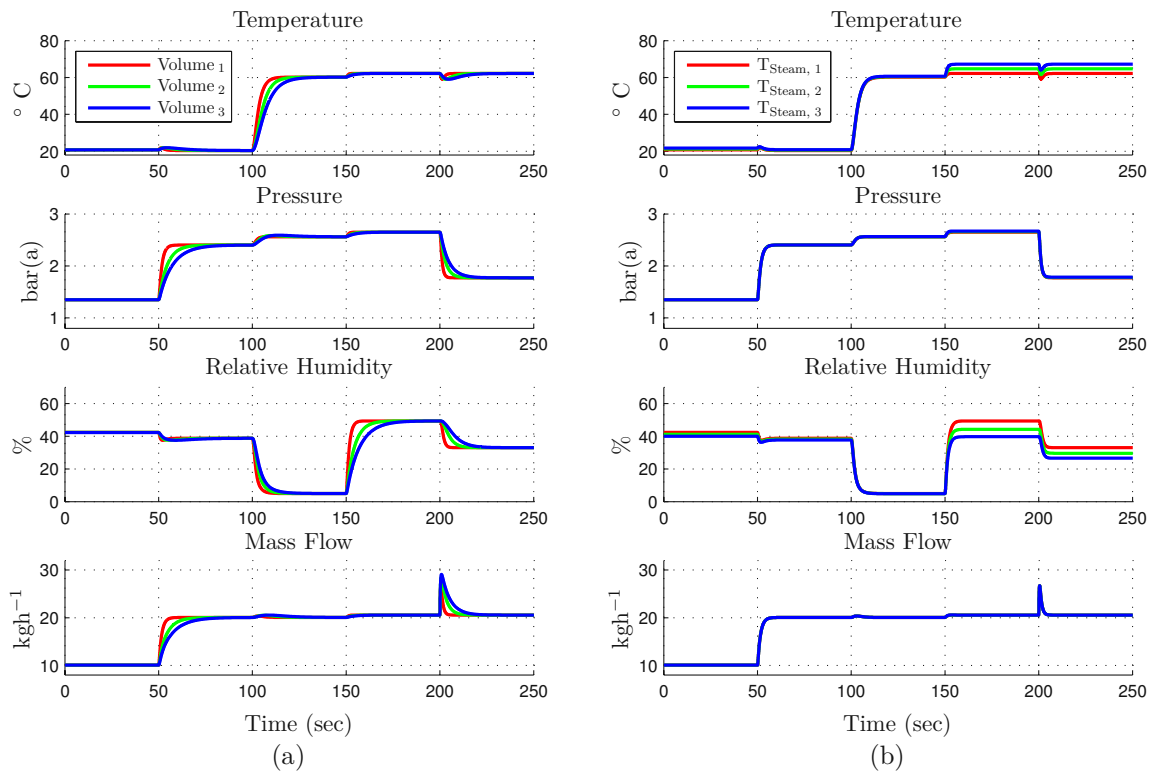


Figure 3.11: Step response of the system model with different system parameters. Plot (a) shows the output trajectories y for the variation of the system volume, and plot (b) shows the output trajectories y for the variation of the steam temperature.

Chapter 4

Control Design - Nonlinear Multivariate Control

The designed gas conditioning system presented in Section 2 is intended to provide a transient testing facility for fuel cell stacks. Therefore, it requires a control concept, which is able to provide a transient control of the test bed. The designed system has multiple inputs and multiple outputs (MIMO), is nonlinear and the thermodynamic states are coupled through various relations. Therefore, a dynamic system model was proposed in Section 3, based on which a model-based nonlinear multivariate control concept will be introduced. This is necessary, since due to the nonlinearity and the coupling of the system, linear control methods are not applicable. Especially not for transient control, which is the main requirement for a dynamic fuel cell stack test bed. Further, a Two-Degree-of-Freedom (2 DoF) controller is designed to provide trajectory tracking for system transients.

In the following, the concept of exact input-output linearisation will be introduced and extended to multivariate systems. Further, a feedback and feedforward controller will be designed for the system and the property of differential flatness will be discussed. Finally, the stability and robustness of the proposed nonlinear controller in the closed loop system will be analysed.

4.1 Feedback Linearisation

The basic idea of feedback linearisation is to transform a nonlinear system into an equivalent linear system. Therefore, the nonlinear controller is designed in such a way that it compensates the nonlinearity of the state equations and the resulting system is linear.

Consider the nonlinear single-input single-output (SISO) system given by

$$\begin{aligned}
 \dot{x} &= f(x) + g(x)u, \\
 y &= h(x),
 \end{aligned}
 \tag{4.1}$$

where $x \in \mathbb{R}^n$ is an n -dimensional state vector, $u \in \mathbb{R}$ is the input vector, $y \in \mathbb{R}$ is the output vector, $f(x)$ and $g(x)$ are smooth vector fields and $h(x)$ is a smooth function. This system is nonlinear in x and linear in u . Such a system is also called *affine* input system. A wide range of technical system are of this structure.

The goal is now to find a state feedback control

$$u = \alpha(x) + \beta(x)\nu \quad (4.2)$$

and a nonlinear change of variables

$$z = T(x) \quad (4.3)$$

that transforms the above nonlinear system into an equivalent linear system. Therefore, the goal of the further investigation is to derive an input-output relation for the described system.

By applying the time derivative to the output y , one obtains

$$\begin{aligned} \dot{y} &= \frac{\partial h}{\partial x} \frac{dx}{dt} = \frac{\partial h}{\partial x} \left(f(x) + g(x) u \right) \\ &= \frac{\partial h}{\partial x} f(x) + \frac{\partial h}{\partial x} g(x) u \\ &= L_f h(x) + L_g h(x) u, \end{aligned} \quad (4.4)$$

where L_f and L_g represent the *Lie* derivatives of the scalar output functions h with respect to $f(x)$ and $g(x)$, respectively. If $L_g h(x) \neq 0$ holds in the neighbourhood of x , then Eq. (4.4) can be reformulated to

$$u(x) = \frac{1}{L_g h(x)} \left(-L_f h(x) + \nu \right), \quad (4.5)$$

where ν is called the new *synthetic* input. Inserting this control law into Eq. (4.4), one obtains

$$\dot{y} = \nu, \quad (4.6)$$

which represents the input-output relation as integrator.

If $L_g h(x) = 0$ in the neighbourhood of x , then the input vector u does not have an effect on the corresponding time derivative. Hence, the time derivative is applied again to Eq. (4.4). This yields

$$\begin{aligned} \ddot{y} &= \frac{\partial L_f h(x)}{\partial x} \frac{dx}{dt} = \frac{\partial L_f h_j(x)}{\partial x} \left(f(x) + g(x) u \right) \\ &= L_f^2 h(x) + L_g L_f h(x) u. \end{aligned} \quad (4.7)$$

Once again, if $L_g L_f h(x) = 0$, then the input vector u does not have an effect on the corresponding time derivative. Repeating this process leads to the recursive definition

$$y = h(x) \quad (4.8)$$

$$\dot{y} = L_f h(x) + \underbrace{L_g h(x)}_{=0} u \quad (4.9)$$

$$\ddot{y} = L_f^2 h(x) + \underbrace{L_g L_f h(x)}_{=0} u \quad (4.10)$$

⋮

$$y^{(\delta-1)} = L_f^{\delta-1} h(x) + \underbrace{(L_g L_f^{\delta-2} h(x))}_{=0} u \quad (4.11)$$

$$y^{(\delta)} = L_f^{\delta} h(x) + \underbrace{(L_g L_f^{\delta-1} h(x))}_{\neq 0} u, \quad (4.12)$$

where the input vector u appears in Eq. (4.12) with a nonzero coefficient. Therefore, the state feedback control can be formulated as

$$u(x) = \frac{1}{L_g L_f^{\delta-1} h(x)} \left(-L_f^{\delta} h(x) + \nu \right), \quad (4.13)$$

whereas the input-output relation is given by

$$y^{(\delta)} = \nu, \quad (4.14)$$

which is a chain of δ integrators. Further, the integer δ is called the *relative degree* of the system. The relative degree defines the number of time derivations, which have to be performed on the system output y , such that the input variable u appears the first time explicitly in the time derivation. If $\delta = 0$, the system has direct feedthrough, which means that the system input directly acts on the system output. If $\delta = 1$, the input variable acts on the first time derivative of y and, therefore, acts on the slope of the system output. If $\delta = 2$, the second time derivative of y is affected - and so on. In that sense, one can think of the relative degree as a distance of the system input to the system output.

The nonlinear state transformation for systems with *full relative degree* ($\delta = n = \dim(x)$) is given by

$$z = T(x) = \begin{bmatrix} z_1 \\ z_2 \\ \vdots \\ z_\delta \end{bmatrix} = \begin{bmatrix} h(x) \\ L_f h(x) \\ \vdots \\ L_f^{\delta-1} h(x) \end{bmatrix}. \quad (4.15)$$

By applying the time derivative to the above introduced state transformation one obtains

$$\dot{z} = \dot{T}(x) = \frac{\partial T(x)}{\partial x} \dot{x} = \begin{bmatrix} L_f h(x) \\ \vdots \\ L_f^{\delta-1} h(x) \\ L_f^{\delta} h(x) + (L_g L_f^{\delta-1} h(x)) u \end{bmatrix}, \quad (4.16)$$

which transforms the nonlinear system into the controllable canonical form [46] given by

$$\begin{bmatrix} \dot{z}_1 \\ \vdots \\ \dot{z}_{\delta-1} \\ \dot{z}_\delta \end{bmatrix} = \begin{bmatrix} z_2 \\ \vdots \\ z_\delta \\ L_f^{\delta} h(x) \end{bmatrix} + \begin{bmatrix} 0 \\ \vdots \\ 0 \\ L_g L_f^{\delta-1} h(x) \end{bmatrix} u, \quad (4.17)$$

$$y = z_1.$$

By applying the control law defined in Eq. (4.13) the system can be represented as

$$\begin{bmatrix} \dot{z}_1 \\ \dot{z}_2 \\ \vdots \\ \dot{z}_{\delta-1} \\ \dot{z}_\delta \end{bmatrix} = \begin{bmatrix} 0 & 1 & 0 & \dots & 0 \\ 0 & 0 & 1 & \dots & 0 \\ \vdots & \vdots & \vdots & \ddots & \vdots \\ 0 & 0 & 0 & \dots & 1 \\ 0 & 0 & 0 & \dots & 0 \end{bmatrix} z + \begin{bmatrix} 0 \\ 0 \\ \vdots \\ 0 \\ 1 \end{bmatrix} \nu, \quad (4.18)$$

$$y = z_1.$$

This transformed system is linear and represents the system as chain of δ integrators. Eq. (4.13) can be interpreted as nonlinear input transformation, which transforms the system input u to the new *synthetic* input ν .

For systems which do not have full relative degree the so called *internal dynamics* has to be investigated [38, 39].

4.2 Feedback Linearisation for Multivariate Systems

The former introduced feedback linearisation for single-input single-output system can now be extended to multivariate systems. Consider the nonlinear multiple-input multiple-output (MIMO) system given by

$$\begin{aligned}\dot{x} &= f(x) + \sum_{i=1}^m g_i(x) u_i, \\ y_j &= h_j(x), \quad j = 1, \dots, m,\end{aligned}\tag{4.19}$$

where $x \in \mathbb{R}^n$ is an n -dimensional state vector, $u \in \mathbb{R}^m$ is an m -dimensional input vector, $y \in \mathbb{R}^m$ is an m -dimensional output vector, $f(x)$ and $g_i(x)$ are smooth vector fields and $h_j(x)$ is a smooth function. This system is nonlinear in x and linear in all system inputs u . Therefore, it is an affine input system.

To establish an input-output relation, the time derivative is applied to each of the system outputs y_j . This yields

$$\begin{aligned}\dot{y}_j &= \frac{\partial h_j}{\partial x} \frac{dx}{dt} = \frac{\partial h_j}{\partial x} \left(f(x) + \sum_{i=1}^m g_i(x) u_i \right) \\ &= \frac{\partial h_j}{\partial x} f(x) + \sum_{i=1}^m \frac{\partial h_j}{\partial x} g_i(x) u_i \\ &= L_f h_j(x) + \sum_{i=1}^m L_{g_i} h_j(x) u_i,\end{aligned}\tag{4.20}$$

where L_f and L_{g_i} represent again the *Lie* derivatives of the scalar output functions h with respect to $f(x)$ and $g_i(x)$, respectively. Similarly to the SISO case, if $L_{g_i} h_j(x) = 0, \forall i$ in the neighbourhood of x , then the input vector u_i does not have an effect on the corresponding time derivative. Hence, the time derivative is applied again

$$\begin{aligned}\ddot{y}_j &= \frac{\partial L_f h_j(x)}{\partial x} \frac{dx}{dt} = \frac{\partial L_f h_j(x)}{\partial x} \left(f(x) + \sum_{i=1}^m g_i(x) u_i \right) \\ &= L_f^2 h_j(x) + \sum_{i=1}^m L_{g_i} L_f h_j(x) u_i.\end{aligned}\tag{4.21}$$

Once again, if $L_{g_i}L_f h_j(x) = 0, \forall i$, then the input vector u_i does not have an effect on the corresponding time derivative. Repeating this process leads to the recursive definition

$$y_j = h_j(x) \quad (4.22)$$

$$\dot{y}_j = L_f h_j(x) + \underbrace{\sum_{i=1}^m L_{g_i} h_j(x)}_{=0} u_i \quad (4.23)$$

$$\ddot{y}_j = L_f^2 h_j(x) + \underbrace{\sum_{i=1}^m L_{g_i} L_f h_j(x)}_{=0} u_i \quad (4.24)$$

⋮

$$y_j^{(\delta_j-1)} = L_f^{\delta_j-1} h_j(x) + \underbrace{\sum_{i=1}^m (L_{g_i} L_f^{\delta_j-2} h_j(x))}_{=0} u_i \quad (4.25)$$

$$y_j^{(\delta_j)} = L_f^{\delta_j} h_j(x) + \underbrace{\sum_{i=1}^m (L_{g_i} L_f^{\delta_j-1} h_j(x))}_{\neq 0 \text{ for at least one } i} u_i, \quad (4.26)$$

where at least one input vector u_i appears in Eq. (4.26) with a nonzero coefficient and δ_j represents the corresponding relative degree of the y_j -th system output. By performing this process on all system outputs y_j , the resulting system of equations can be written as

$$y^{(\delta)} = l(x) + J(x) u, \quad (4.27)$$

with

$$y^{(\delta)} = \begin{bmatrix} y_1^{(\delta_1)} \\ y_2^{(\delta_2)} \\ \vdots \\ y_m^{(\delta_m)} \end{bmatrix}, \quad l(x) = \begin{bmatrix} L_f^{\delta_1} h_1(x) \\ L_f^{\delta_2} h_2(x) \\ \vdots \\ L_f^{\delta_m} h_m(x) \end{bmatrix} \quad (4.28)$$

and the $(m \times m)$ matrix $J(x)$ is given by

$$J(x) = \begin{bmatrix} L_{g_1} L_f^{\delta_1-1} h_1(x) & \dots & L_{g_m} L_f^{\delta_1-1} h_1(x) \\ L_{g_1} L_f^{\delta_2-1} h_2(x) & \dots & L_{g_m} L_f^{\delta_2-1} h_2(x) \\ \vdots & \ddots & \vdots \\ L_{g_1} L_f^{\delta_m-1} h_m(x) & \dots & L_{g_m} L_f^{\delta_m-1} h_m(x) \end{bmatrix}. \quad (4.29)$$

This matrix is referred to as *decoupling matrix*. The properties of the decoupling matrix play an important role in the multivariate case. It indicates, if the different system outputs can be decoupled from one another completely or not.

If the decoupling matrix is regular, then a new *synthetic* input vector ν can be introduced by expressing Eq. (4.27) as

$$u = \alpha(x) + \beta(x) \nu, \quad (4.30)$$

with $\alpha(x)$ and $\beta(x)$ defined as

$$\alpha(x) = -J^{-1}(x) l(x), \quad (4.31)$$

$$\beta(x) = J^{-1}(x). \quad (4.32)$$

Inserting the nonlinear input transformation Eq. (4.30) into Eq. (4.27) the input output relations are given by

$$\begin{bmatrix} y_1^{(\delta_1)} \\ y_2^{(\delta_2)} \\ \vdots \\ y_m^{(\delta_m)} \end{bmatrix} = \begin{bmatrix} \nu_1 \\ \nu_2 \\ \vdots \\ \nu_m \end{bmatrix}, \quad (4.33)$$

which shows that each *synthetic* input ν_j acts on the derivative $y_j^{(\delta_j)}$ of the output y_j . Therefore, each output y_j is obtained by δ_j -th integrations of the new *synthetic* input ν_j . Hence, each equation in Eq. (4.33) represents an integrator chain of the length δ_j .

If the decoupling matrix is not regular, literature suggests the so called *dynamic extension algorithm*.

The overall relative degree of the system is defined by $\Delta = \sum_{j=1}^m \delta_j$. If $\Delta = n = \dim(x)$, the system is to be said to have *full relative degree*. For a system with full relative degree, the nonlinear state transformation $T(x)$ is given by

$$z = T(x) = \begin{bmatrix} z_1 \\ z_2 \\ \vdots \\ z_{\delta_1} \\ z_{\delta_1+1} \\ z_{\delta_1+2} \\ \vdots \\ z_{\delta_1+\delta_2} \\ \vdots \\ z_{\delta_1+\dots+\delta_{n-1}+1} \\ z_{\delta_1+\dots+\delta_{n-1}+2} \\ \vdots \\ z_n \end{bmatrix} = \begin{bmatrix} h_1(x) \\ L_f h_1(x) \\ \vdots \\ L_f^{\delta_1-1} h_1(x) \\ h_2(x) \\ L_f h_2(x) \\ \vdots \\ L_f^{\delta_2-1} h_2(x) \\ \vdots \\ h_m(x) \\ L_f h_m(x) \\ \vdots \\ L_f^{\delta_m-1} h_m(x) \end{bmatrix}. \quad (4.34)$$

By applying the time derivative to the above state transformation, one obtains

$$\dot{z} = \dot{T}(x) = \frac{\partial T(x)}{\partial x} \dot{x} = \begin{bmatrix} L_f h_1(x) \\ \vdots \\ L_f^{\delta_1-1} h_1(x) \\ L_f^{\delta_1} h_1(x) + \sum_{i=1}^m (L_{g_i} L_f^{\delta_1-1} h_1(x)) u_i \\ L_f h_2(x) \\ \vdots \\ L_f^{\delta_2-1} h_2(x) \\ L_f^{\delta_2} h_2(x) + \sum_{i=1}^m (L_{g_i} L_f^{\delta_2-1} h_2(x)) u_i \\ \vdots \\ L_f h_m(x) \\ \vdots \\ L_f^{\delta_m-1} h_m(x) \\ L_f^{\delta_m} h_m(x) + \sum_{i=1}^m (L_{g_i} L_f^{\delta_m-1} h_m(x)) u_i \end{bmatrix}, \quad (4.35)$$

which transforms the system into the controllable canonical form, which can further be written as

$$\begin{bmatrix} \dot{z}_1 \\ \dot{z}_2 \\ \vdots \\ \dot{z}_{\delta_1} \\ \dot{z}_{\delta_1+1} \\ \dot{z}_{\delta_1+2} \\ \vdots \\ \dot{z}_{\delta_1+\delta_2} \\ \vdots \\ \dot{z}_{\delta_1+\dots+\delta_{m-1}+1} \\ \dot{z}_{\delta_1+\dots+\delta_{m-1}+2} \\ \vdots \\ \dot{z}_n \end{bmatrix} = \begin{bmatrix} z_2 \\ z_3 \\ \vdots \\ L_f^{\delta_1} h_1(x) \\ z_{\delta_1+2} \\ z_{\delta_1+3} \\ \vdots \\ L_f^{\delta_2} h_2(x) \\ \vdots \\ z_{\delta_1+\dots+\delta_{m-1}+2} \\ z_{\delta_1+\dots+\delta_{m-1}+3} \\ \vdots \\ L_f^{\delta_m} h_m(x) \end{bmatrix} + \begin{bmatrix} 0 \\ 0 \\ \vdots \\ \sum_{i=1}^m (L_{g_i} L_f^{\delta_1-1} h_1(x)) u_i \\ 0 \\ 0 \\ \vdots \\ \sum_{i=1}^m (L_{g_i} L_f^{\delta_2-1} h_2(x)) u_i \\ \vdots \\ 0 \\ 0 \\ \vdots \\ \sum_{i=1}^m (L_{g_i} L_f^{\delta_m-1} h_m(x)) u_i \end{bmatrix}, \quad (4.36)$$

$$y = [z_1, z_{\delta_1+1}, z_{\delta_1+\delta_2+1}, \dots, z_{\delta_1+\delta_2+\dots+\delta_{m-1}+1}]^T.$$

This can be written in a compact form as new state space representation of the system

$$\dot{z} = A_c z + B_c \beta(x)^{-1} (u - \alpha(x)), \quad (4.37a)$$

$$u = \alpha(x) + \beta(x) \nu, \quad (4.37b)$$

$$y = C_c z. \quad (4.37c)$$

By inserting the nonlinear input transformation, given by Eq. (4.37b), into Eq. (4.37a), the system transforms into

$$\begin{aligned} \dot{z} &= A_c z + B_c \nu, \\ y &= C_c z, \end{aligned} \quad (4.38)$$

which is a linear system in the new coordinates z and input affine in the new *synthetic* inputs ν . The matrices A_c , B_c and C_c are given by

$$A_c = \begin{bmatrix} A_{c,1} & 0 & \dots & 0 \\ 0 & A_{c,2} & \dots & 0 \\ \vdots & \vdots & \ddots & \vdots \\ 0 & 0 & \dots & A_{c,m} \end{bmatrix}, \quad B_c = \begin{bmatrix} B_{c,1} & 0 & \dots & 0 \\ 0 & B_{c,2} & \dots & 0 \\ \vdots & \vdots & \ddots & \vdots \\ 0 & 0 & \dots & B_{c,m} \end{bmatrix}, \quad (4.39)$$

$$C_c = \begin{bmatrix} C_{c,1} & 0 & \dots & 0 \\ 0 & C_{c,2} & \dots & 0 \\ \vdots & \vdots & \ddots & \vdots \\ 0 & 0 & \dots & C_{c,m} \end{bmatrix},$$

where the matrix $A_{c,j}$ is a $(\delta_j \times \delta_j)$ matrix, $B_{c,j}$ is a $(\delta_j \times 1)$ vector and $C_{c,j}$ is a $(1 \times \delta_j)$ vector given by

$$A_{c,j} = \begin{bmatrix} 0 & 1 & 0 & \dots & 0 \\ 0 & 0 & 1 & \dots & 0 \\ \vdots & \vdots & \vdots & \ddots & \vdots \\ 0 & 0 & 0 & \dots & 1 \\ 0 & 0 & 0 & \dots & 0 \end{bmatrix}, \quad B_{c,j} = \begin{bmatrix} 0 \\ 0 \\ \vdots \\ 0 \\ 1 \end{bmatrix}, \quad C_{c,j} = [1, 0, \dots, 0]. \quad (4.40)$$

The transformed system (Eq. (4.38)) consists of a block diagonal structure composed of the decoupled subsystems. Each subsystem is a linear SISO system with the new *synthetic* input ν_j as input variable and y_j as output variable.

The resulting linear and decoupled system is shown in Fig. 4.1. The block Σ represents the nonlinear system given by Eq. (4.19). The nonlinear input transformation is given by the Σ^{-1} block, which represents Eq. (4.37b). The overall resulting system is given by Eq. (4.38) and has as input vector the new *synthetic* input vector ν and as system output the output vector y .

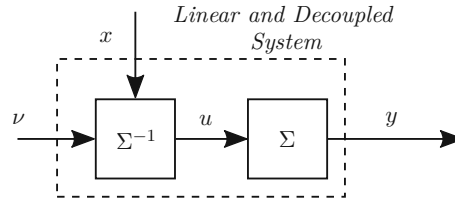


Figure 4.1: The figure depicts the linear and decoupled MIMO system. Σ represents the nonlinear system given by Eq. (4.19). Σ^{-1} represents the nonlinear input transformation, which transforms the whole system into a linear and decouple system.

One can think of the nonlinear input transformation as system inversion, hence the labeling of the block as Σ^{-1} .

4.3 Flatness

Differential flatness is a property of a class of multivariate nonlinear systems and has first been introduced in [47–51]. The concept of *flatness*, or *differential flatness*, describes systems, where the dynamic system equations can be rewritten such that the input variables and all states of the system can be expressed as functions of the system output and its time derivatives. This is of high importance for practical use, since if a system is flat the required input variables and the evolution of the system states can be directly calculated from the desired output trajectories.

Considering a nonlinear system of the form

$$\dot{x} = f(x, u), \quad x(0) = x_0, \quad (4.41)$$

where $x \in \mathbb{R}^n$ and $u \in \mathbb{R}^m$. This system is said to be differentially flat, if there exists a set of output variables

$$y = h(x, u, \dot{u}, \dots, u^{(\alpha)}), \quad (4.42)$$

which are differentially independent

$$\varphi(y, \dot{y}, \dots, y^{(\gamma)}) = 0, \quad (4.43)$$

and the system states x and input variables u are functions of these flat outputs and a finite number of their derivatives

$$x = \Phi(y, \dot{y}, \dots, y^{n-1}), \quad (4.44)$$

$$u = \Psi(y, \dot{y}, \dots, y^n). \quad (4.45)$$

In that case, y represents the *flat outputs* of the system, and the system is called *differential flat* or *flat system*.

One major property of flat systems is that due to Eq. (4.44) and Eq. (4.45) the evolution of the state variables x and input variables u can be calculated directly from a given trajectory y and its derivatives without the need to integrate the differential equations given by (4.41). Hence, the denotation as *differential flat*.

Since the flat coordinates y are differentially independent, they do not possess system dynamics i.e. they do not depend on a differential equations. Therefore, they represent a dynamic free system, which is called a *trivial* system. Both system descriptions Eq. (4.41) and Eq. (4.42), Eq. (4.44) and Eq. (4.45) are equivalent and can be transformed into each other. This transformation is done by the *Lie-Bäcklund-Transformation*. Fig. 4.2 illustrates both coordinate spaces with the coordinate vectors x and y and the *Lie-Bäcklund-Transformation*. The plot also illustrates the origin of the denotation of the described system property as *flatness*.

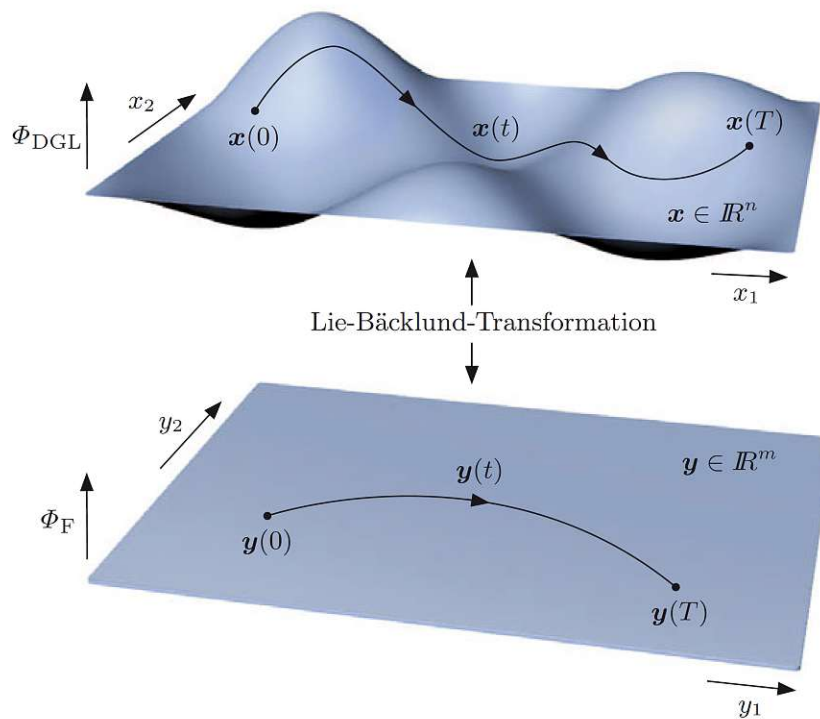


Figure 4.2: The Lie-Bäcklund transformation transforms the system from the state space coordinates into flat coordinates. To visualise this, the potential Φ_{DGL} of the conservative differential equation $\dot{x} = f(x, u)$ with $\nabla\Phi_{\text{DGL}} = f(x, 0)$ and the potential Φ_{F} of the trivial system in flat coordinates with $\nabla\Phi_{\text{F}} = 0$ is plotted on the z-axis [39].

Since the system property of flatness allows to solve a set of algebraic equations instead of solving a set of differential equations, it has found a wide field of applications [52–58].

4.4 Feedforward Control

Feedforward control (FFC) is a powerful way to control or enhance the control of a dynamic system. In a feedforward control scheme, the control input adjustment is not error-based, but based on process knowledge in form of a system model of the process. This knowledge is exploited to calculate a control input, which steers the system into the desired set point. Since the system model never matches the real system perfectly, feedforward control is usually applied additionally to a feedback control (FBC) structure. This combined control structure is called Two-Degree-of-Freedom (2 DoF) control. Fig. 4.3 illustrates such a control structure for a SISO system.

Exemplary, if the system can be modelled as an integrator, a straight forward feedforward design would be to use the first time derivative of the desired output trajectory (corresponds to the inverse of the system) as system input. The system would integrate the applied control input and the resulting system output would be exactly the desired trajectory.

Applying feedforward control together with feedback control does not influence the stability of the feedback loop because the feedforward control does not introduce additional dynamics in the closed loop system.

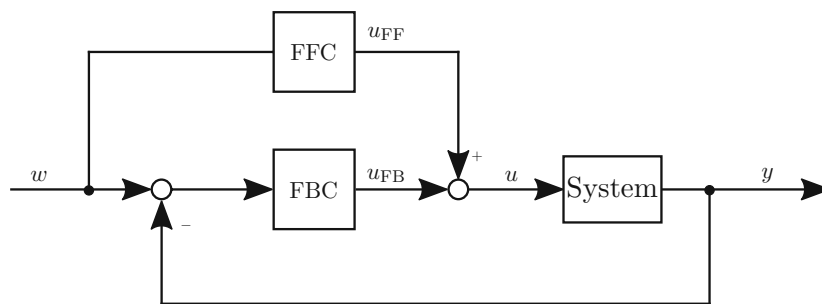


Figure 4.3: Illustration of a Two-Degree-of-Freedom (2DoF) control structure for a SISO system.

The feedforward function can be developed in two main ways: First, by deriving a system model. This will be done for the *high level* control scheme. Second, by measuring experimental data. This is applied in the *low level* sub-controllers discussed in Section 5.2

4.5 Controller Design for the Nonlinear System Model

In the following the previously introduced methods will be applied to the nonlinear system model derived in Section 3. First, the nonlinear state transformation will be introduced, which transforms the system into linear and decoupled SISO subsystems. Second, a 2DoF control structure will be introduced, which controls the decoupled subsystems. Third, constraints on the system inputs and parameter sensitivity of the resulting closed loop system will be discussed.

4.5.1 Exact Linearisation and Nonlinear State Transformation

The derived system model Eq. (3.21a) and Eq. (3.21b) from Section 3 can be written in the form

$$\begin{aligned} \dot{x} &= f(x) + \sum_{i=1}^4 g_i(x) u_i, \\ y &= h(x), \end{aligned} \quad (4.46)$$

where the state vector $x \in \mathbb{R}^7$, input vector $u \in \mathbb{R}^4$ and output vector $y \in \mathbb{R}^4$ are given by

$$x = \begin{bmatrix} m_G \\ m_S \\ T \\ \xi \end{bmatrix}, \quad u = \begin{bmatrix} \dot{m}_{G,u} \\ T_u \\ \dot{m}_{S,u} \\ A_u \end{bmatrix}, \quad y = \begin{bmatrix} T \\ p \\ \varphi \\ \dot{m}_{\text{out}} \end{bmatrix}. \quad (4.47)$$

The system equations are linear in the input variables u , but nonlinear in the state variables x . Therefore, the system is an affine input system. To establish an input-output relation, the time derivative is applied to each of the system outputs y_j .

$$\begin{aligned} \dot{y}_j &= \frac{\partial h_j}{\partial x} \frac{dx}{dt} = \frac{\partial h_j}{\partial x} \left(f(x) + \sum_{i=1}^4 g_i(x) u_i \right) \\ &= L_f h_j(x) + \sum_{i=1}^4 L_{g_i} h_j(x) u_i, \end{aligned} \quad (4.48)$$

This is performed until at least one input vector u_i appears explicitly in the time derivatives. This can be written in the generalised form

$$y_j^{(\delta_j)} = L_f^{\delta_j} h_j + \sum_{i=1}^4 (L_{g_i} L_f^{\delta_j-1} h_j) u_i, \quad (4.49)$$

where δ_j is the relative degree of the output vector y_j . This can be done for all four output variables. The obtained relative degrees of the system outputs and the resulting total relative degree of the system are

$$\delta_{1,2,3} = 2, \quad \delta_4 = 1, \quad \Delta = \sum_{j=1}^4 \delta_j = 7. \quad (4.50)$$

Therefore, the system can be written in compact form as

$$y^{(\delta)} = l(x) + J(x) u \quad (4.51)$$

with

$$y^{(\delta)} = \begin{bmatrix} y_1^{(\delta_1)} \\ y_2^{(\delta_2)} \\ y_3^{(\delta_3)} \\ y_4^{(\delta_4)} \end{bmatrix} = \begin{bmatrix} \dot{y}_1 \\ \dot{y}_2 \\ \dot{y}_3 \\ \dot{y}_4 \end{bmatrix}, \quad l(x) = \begin{bmatrix} L_f^2 h_1(x) \\ L_f^2 h_2(x) \\ L_f^2 h_3(x) \\ L_f h_4(x) \end{bmatrix}. \quad (4.52)$$

The elements of the decoupling matrix $J(x)$ are given by

$$\begin{aligned} J_{i,k}(x) &= L_{g_k} L_f h_i(x), \quad k = 1, \dots, 4, \quad i = 1, 2, 3, \\ J_{4,k}(x) &= L_{g_k} h_4(x), \quad k = 1, \dots, 4. \end{aligned} \quad (4.53)$$

As a result of the dimension of the state vector x ($n = \dim(x) = 7$), the relative degree of the outputs and the complex couplings in the output functions the resulting expression in Eq. (4.51) are large and not insightful. For the reason of readability, the detailed calculations of the *Lie* derivatives are not given.

Since $\Delta = n = \dim(x)$ holds for the system given in Eq. (4.46), the system has full relative degree. Therefore, the nonlinear state transformation $T(x)$ is given by

$$z = T(x) = \begin{bmatrix} h_1(x) \\ L_f h_1(x) \\ h_2(x) \\ L_f h_2(x) \\ h_3(x) \\ L_f h_3(x) \\ h_4(x) \end{bmatrix}. \quad (4.54)$$

This transforms the system into the controllable canonical form. Further, by applying the nonlinear input transformation the system can be transformed into a linear and decoupled system. This can be written in a compact, with the new state space representation of the system as

$$\dot{z} = A_c z + B_c \beta(x)^{-1} (u - \alpha(x)), \quad (4.55a)$$

$$u = \alpha(x) + \beta(x) \nu, \quad (4.55b)$$

$$y = C_c z, \quad (4.55c)$$

with $\alpha(x)$ and $\beta(x)$ defined as

$$\alpha(x) = -J^{-1}(x) l(x), \quad (4.56)$$

$$\beta(x) = J^{-1}(x), \quad (4.57)$$

and the matrices A_c , B_c and C_c given by

$$A_c = \begin{bmatrix} A_{c,1} & 0 & 0 & 0 \\ 0 & A_{c,2} & 0 & 0 \\ 0 & 0 & A_{c,3} & 0 \\ 0 & 0 & 0 & A_{c,4} \end{bmatrix}, \quad B_c = \begin{bmatrix} B_{c,1} & 0 & 0 & 0 \\ 0 & B_{c,2} & 0 & 0 \\ 0 & 0 & B_{c,3} & 0 \\ 0 & 0 & 0 & B_{c,4} \end{bmatrix}, \quad (4.58)$$

$$C_c = \begin{bmatrix} C_{c,1} & 0 & 0 & 0 \\ 0 & C_{c,2} & 0 & 0 \\ 0 & 0 & C_{c,3} & 0 \\ 0 & 0 & 0 & C_{c,4} \end{bmatrix}$$

with the matrix $A_{c,1-4}$, $B_{c,1-4}$ and $C_{c,1-4}$ given by

$$A_{c,j} = \begin{bmatrix} 0 & 1 \\ 0 & 0 \end{bmatrix}, \quad B_{c,j} = \begin{bmatrix} 0 \\ 1 \end{bmatrix}, \quad C_{c,j} = [1, 0], \quad j = 1, 2, 3 \quad (4.59)$$

$$A_{c,4} = 0, \quad B_{c,4} = 1, \quad C_{c,4} = 1$$

The newly introduced vector ν represents the new *synthetic* input of the system. By inserting Eq. (4.55b) into Eq. (4.55a), the system transforms into

$$\begin{aligned} \dot{z} &= A_c z + B_c \nu, \\ y &= C_c z. \end{aligned} \quad (4.60)$$

The new *synthetic* input to output relations for the resulting linear and decoupled SISO systems are given by a chain of δ_j integrators. The transformation from the nonlinear system Eq. (4.46) to the linear and decoupled system Eq. (4.60) is depicted in Fig. 4.4. Fig. 4.4a shows the nonlinear system, where the input variables u can not be linked to a specific output variable y . In Fig. 4.4b, the resulting input to output relations as integrator chains for each linear and decoupled SISO system are shown. Each new *synthetic* input variable ν_j is directly associated with the system output y_j . Fig. 4.4b is a different representation of Fig. 4.1. While the former is a representation of the resulting *structure* of the transformed system, the latter is a representation of the concrete realisation of the nonlinear transformation. The control inputs u in Fig. 4.1 are real quantities at the test bed, while the integrator chains represent the resulting input to output behaviour of the systems.

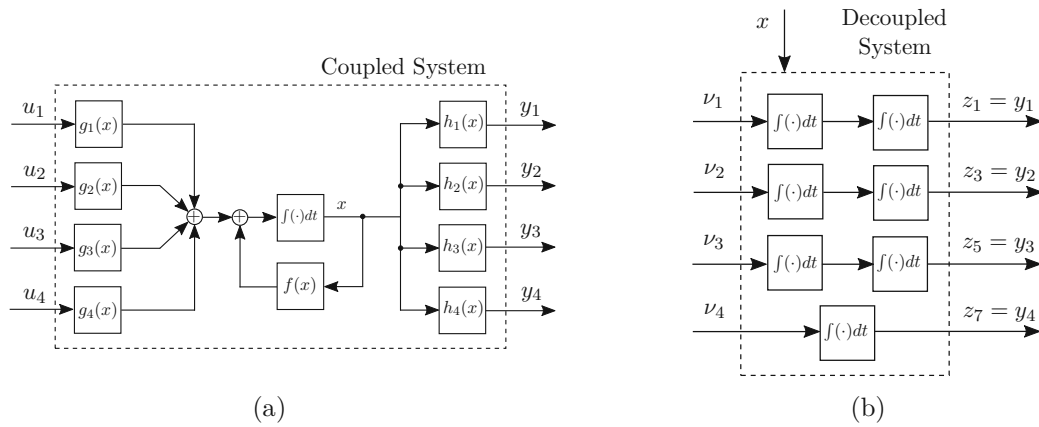


Figure 4.4: Schematic view of the transformation of the coupled system (a) into the decoupled system (b). The decoupled system is represented as chain of integrators with the new input variable ν . The length of the chain of integrators is equal to the *relative degree* δ_j of the output y_j .

4.5.2 Trajectory Tracking and Error Dynamics

To achieve both good trajectory tracking and good disturbance rejection, a Two-Degree-of-Freedom (2 DoF) controller is designed for each of the decoupled subsystems. The output $y(t)$ should track a reference signal $r(t)$. For each of the decoupled subsystems, the new *synthetic* input variable ν_j represents the input to δ_j chain of integrators. Therefore, the feedforward signal has to be the δ_j -th derivative of the reference trajectory to be followed by the output y_j . This can be directly seen in Fig. 4.4b.

Therefore, the knowledge of the input-output behaviour of the system as chain of δ_j integrators is utilised to design a feedforward control for each of the decoupled subsystems. The feedforward input is given by

$$r^{(\delta)} = \begin{bmatrix} r_1^{(\delta_1)} \\ r_2^{(\delta_2)} \\ r_3^{(\delta_3)} \\ r_4^{(\delta_4)} \end{bmatrix} = \begin{bmatrix} \ddot{r}_1 \\ \ddot{r}_2 \\ \ddot{r}_3 \\ \dot{r}_4 \end{bmatrix} = \begin{bmatrix} \nu_{\text{FF},1} \\ \nu_{\text{FF},2} \\ \nu_{\text{FF},3} \\ \nu_{\text{FF},4} \end{bmatrix} = \nu_{\text{FF}}, \quad (4.61)$$

where r_{1-4} represent the four reference trajectories for the subsystems.

For controller designed the tracking error e is defined as

$$e = y(t) - r(t), \quad (4.62)$$

where $r(t)$ are the reference trajectories, which the system outputs $y(t)$ should follow. The tracking error vector for each component can be expanded by the additional terms

$$e_{j,0} = \int_0^t e_j(\tau) d\tau, \quad e_{j,1} = e_j, \quad e_{j,2} = \dot{e}_j, \quad (4.63)$$

which can be used to design the 2 DoF controller. The new *synthetic* input ν can be written as a combination of the feedforward part Eq. (4.61) and a feedback part

$$\nu = \nu_{\text{FF}} + \nu_{\text{FB}}. \quad (4.64)$$

The feedforward part exploits the knowledge that the transformed system is represented as chain of integrators. The feedback part is designed as a PID controller [59, 60]:

$$\begin{aligned} \nu_k &= \ddot{r}_k - K_{I,k} e_{k,0} - K_{P,k} e_{k,1} - K_{D,k} e_{k,2}, \quad k = 1, 2, 3, \\ \nu_4 &= \dot{r}_4 - K_{I,4} e_{4,0} - K_{P,4} e_{4,1} - K_{D,4} e_{4,2}, \end{aligned} \quad (4.65)$$

where $K_{P,1-4}$, $K_{I,1-4}$ and $K_{D,1-4}$ represent the gains of the four PID controllers. The equation can be written in the compact form as

$$\nu = r^{(\delta)} - Ke \quad (4.66)$$

with the feedback gain matrix defined as

$$K = \begin{bmatrix} K_1^{\text{PID}} & 0 & 0 & 0 \\ 0 & K_2^{\text{PID}} & 0 & 0 \\ 0 & 0 & K_3^{\text{PID}} & 0 \\ 0 & 0 & 0 & K_4^{\text{PID}} \end{bmatrix} \quad (4.67)$$

with the components K_j^{PID} given by

$$K_j^{\text{PID}} = [K_{I,j} \quad K_{P,j} \quad K_{D,j}], \quad j = 1, \dots, 4. \quad (4.68)$$

The error vector e is given by

$$e = [e_1, e_2, e_3, e_4]^T, \quad (4.69)$$

with the components given by

$$e_j = [e_{j,0}, e_{j,1}, e_{j,2}]^T, \quad j = 1, \dots, 4. \quad (4.70)$$

The resulting control structure is shown in Fig. 4.5. Since the system outputs y_{1-4} are flat outputs of the system, the system property of flatness can be utilised to minimise the feedback disturbance on the decoupling of the system. Therefore, a flatness-based feedforward calculation of the states x is applied. Instead of using a state vector feedback for the nonlinear input transformation, the so calculated states x_{FF} are applied in Eq. (4.55b). The states x_{FF} are calculated offline by solving the set of equations given by Eq. (4.54). This leads to the functional dependency given in Eq. (4.44). The so obtained states are then fed into the system.

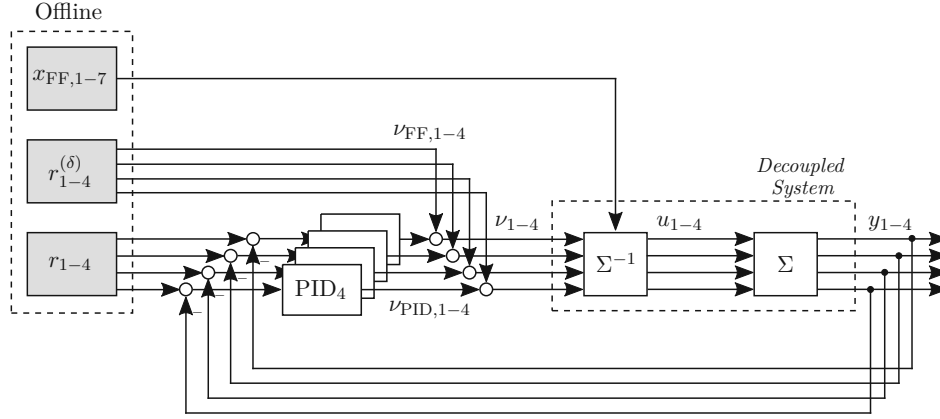


Figure 4.5: Block diagram of the Two-Degree-of-Freedom (2DoF) controller. To each decoupled linear system, a PID controller is applied.

The above introduced coordinate transformation transforms the system equation

$$\dot{z} = A_c z + B_c \beta(x)^{-1} (u - \alpha(x)) \quad (4.71)$$

from the z coordinates into the error coordinates e . The full system transformation is derived in Appendix A.1. The resulting error dynamics is given by

$$\dot{e} = A_c e + B_c [\beta(x)^{-1} (u - \alpha(x)) - r^{(\delta)}] \quad (4.72)$$

with

$$u = \alpha(x) + \beta(x) \nu, \quad (4.73)$$

$$\nu = \nu_{FF} + \nu_{FB} = r^{(\delta)} - K e, \quad (4.74)$$

which, inserted into Eq. (4.72), transforms the system into

$$\dot{e} = (A_c - B_c K) e. \quad (4.75)$$

The above equation represents a linear error dynamics and the gain matrix K can be chosen such that the system is stable. E.g. such that $(A_c - B_c K)$ is *Hurwitz*.

4.5.3 System Input Constraints

During system operation the following two problems arise in determining the system input u .

First, the decoupling matrix $J(x)$, as introduced in Eq. (4.51), is not invertible for all states x . Although this is not the case, if the system is in the operating range described in Table 2.1, during startup the system has to cross a region, where $J(x)$ does not have full rank. The physical interpretation is the following: During startup the system pressure p is equal to the ambient pressure p_0 , and therefore, the actuation of the backpressure valve has no effect on the outflowing mass flow \dot{m}_{out} . Hence, the decoupling matrix $J(x)$ does not have full rank. Therefore, an additional condition is required to invert the decoupling matrix. So the system can be steered into the operating range, where the decoupling matrix $J(x)$ has full rank and the additional condition can be dropped.

Second, constraints on the actuators limit the available input range and therefore, lead to deviations of the system outputs from the reference trajectories. In order to achieve a better trajectory tracking, these deviations have to be minimised.

Both of the problems can be solved by introducing the following *Lagrange* function

$$\begin{aligned}\mathcal{L} &= \alpha \frac{1}{2} u^T R u \\ &+ \frac{1}{2} (y^{(\delta)} - r^{(\delta)})^T Q (y^{(\delta)} - r^{(\delta)}) \\ &+ \lambda^T (Mu - \gamma).\end{aligned}\quad (4.76)$$

In the first term, α is active ($\alpha = 1$) if the decoupling matrix is not invertible, otherwise $\alpha = 0$ and R is (4×4) symmetric and positive definite matrix, which is used as weighting matrix. This term additionally minimises the input vector u in the optimisation function. This additional condition is responsible for the invertibility of the decoupling matrix $J(x)$, if it does not have full rank.

The second term minimises the deviation of the trajectory curvature. Q is (4×4) symmetric and positive definite matrix, which is used as weighting matrix, $y^{(\delta)}$ is given by Eq. (4.51) and $r^{(\delta)}$ is defined in Eq. (4.61).

In the third term, λ represents the *Lagrange Multiplier*, which is used for the active constraints. If the constraints are reached by one or more input variables, the constraints are added using the *active-set-method*. M is a (4×4) identity matrix, and γ is a (4×1) vector of the actuator constraints listed in Table 2.2.

By reformulating Eq. (4.76) into

$$\mathcal{L} = \frac{1}{2} u^T E u + \frac{1}{2} u^T F + \lambda^T (Mu - \gamma) \quad (4.77)$$

with

$$E = R + J(x)^T Q J(x), \quad (4.78)$$

$$F = J(x)^T Q (l(x) - r^{(\delta)}), \quad (4.79)$$

the solution can be written as

$$u = -E^{-1} (M_{\text{act}}^T \lambda_{\text{act}} + F) \quad (4.80)$$

with

$$\lambda_{\text{act}} = -(M_{\text{act}} E^{-1} M_{\text{act}}^T)^{-1} (\gamma_{\text{act}} + M_{\text{act}} E^{-1} F), \quad (4.81)$$

where M_{act} and λ_{act} represent the active constraints. The so obtained Eq. (4.80) for the constrained control input replaces Eq. (4.73) in Σ^{-1} in Fig. 4.5.

4.5.4 Closed Loop Simulation Results

In the following simulation results for the proposed nonlinear multivariate control strategy are shown to evaluate the closed loop performance of the system. The simulations have been performed with set point changes in the operating range defined in Table 2.1. Whereas the reference trajectories for the set point changes have been calculated in accordance to the *relative degree* of the corresponding output. Fig. 4.6 shows a series of step changes of the

closed loop system. Fig. 4.6b shows the comparison of the reference trajectories r (blue dashed line) and the achieved output trajectories y (red full line) of the system. The plot shows good agreement for all trajectories. The poles of the controllers have been placed as following: For the channels $y_{1,2,3}$ with $\delta_{1,2,3} = 2$, the poles are at $s_1 = -1$, $s_{2,3} = -8 \pm 1j$, and for the channel y_4 with $\delta_4 = 1$, the poles are at $s_{1,2} = -5$. This configuration is robust for a wide range of tested parameter variations.

The corresponding control inputs u are shown in Fig. 4.6a. The coupling of the system can be seen on the control inputs. For each alteration of the trajectories shown in Fig. 4.6b, all control inputs have to be altered in order to achieve the decoupling and hence, the desired output trajectory y .

The limitation on the trajectory shape of the system output y_j derives from the applied mathematical concept and demands that the reference trajectories are at least δ_j times differentiable. This allows a wide range of feasible trajectories. The limiting factors for the trajectory slopes are the actuator dynamics, which have been modelled by first order lag elements. In order to achieve a fast response of the system, the actuators have to be able to follow the rapid change of the control inputs.

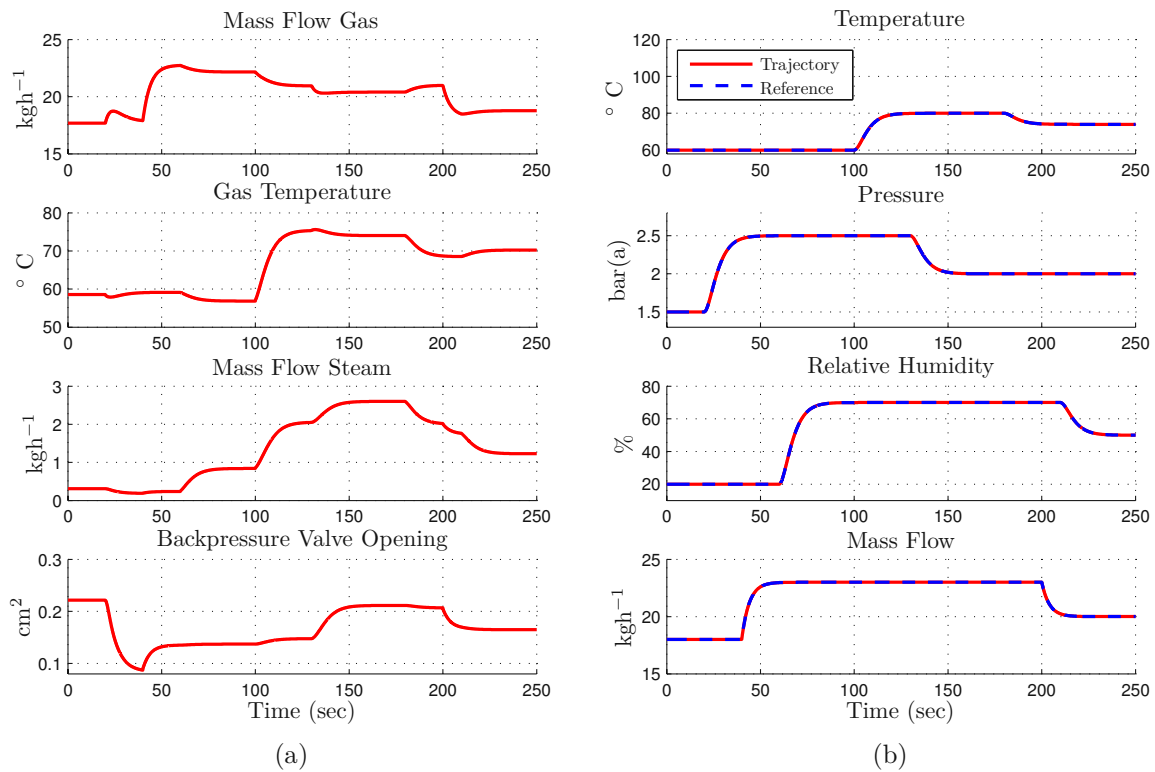


Figure 4.6: The plot shows a series of step changes of the closed loop system. Plot (a) shows the control input u . Plot (b) shows the system output y , with the reference trajectory in dashed blue and the achieved system output in red.

To compare the performance with the open loop system response, in Fig. 4.7, the closed loop performance is illustrated in the system state space, similar to Fig. 3.6 in Section 3.2. In the left column (Fig. 4.7a and Fig. 4.7c) three dimensional plots are shown, while in the right column (Fig. 4.7b and Fig. 4.7d) the corresponding two dimensional projections are shown.

In Fig. 4.7a, and Fig. 4.7b, the set point change of the *double set point change* (Fig. 3.6e and Fig. 3.6f), which leads to condensation in the system, is compared to three possible closed

loop trajectories (blue full lines), which avoid the crossing of the dew point and therefore are safe for the system. The plots clearly show that the proposed control concept not only ensures that the set point transients stay within the boundaries, but also enables the system to follow a specific path during transitions.

To further illustrate this, a more complex system trajectory is shown in Fig. 4.7c and Fig. 4.7d. It can be seen that the controller ensures that the system follows a specific path during the set point transients. This enables the system to perform transitions such that the degradation of the fuel cell stack can be prevented or specific test cycles can be applied.

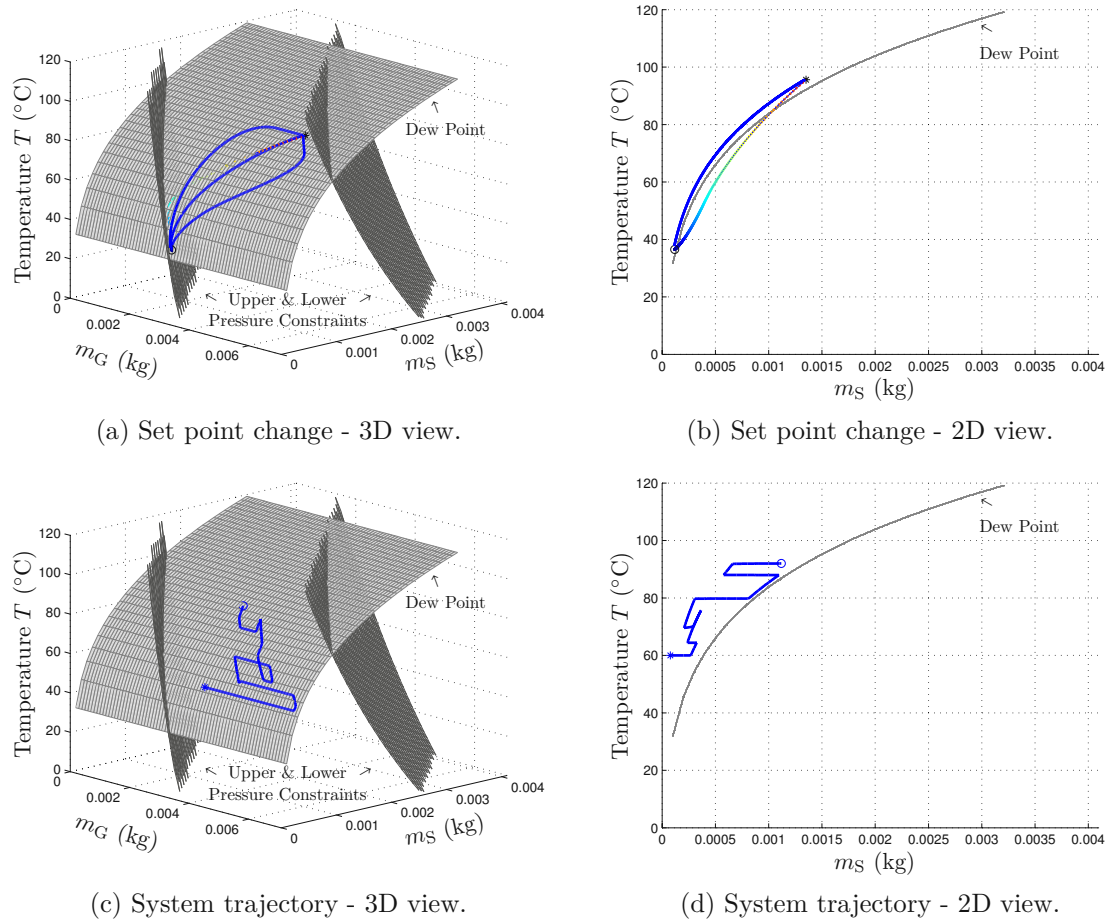


Figure 4.7: The figure shows different closed loop trajectories of the system. Fig. (a) and (b) show a comparison of an open loop set point change (from Fig. 3.6e) with three different closed loop trajectories (blue full lines). In contrast to the open loop system, the closed loop trajectories stay within the operation range. Fig. (c) and (d) show a more complex system trajectory, which demonstrates the closed loop system performance.

4.6 Stability Analysis of Closed Loop System

Stability analysis plays an important role in control theory and in the study of dynamic systems. In Section 3.2.1, the Lyapunov stability theory was introduced and applied to analyse the stability of the derived nonlinear system model. Here, this concept will be expanded by the notion of boundedness in the sense of Lyapunov. This will further be used

to analyse the closed loop stability of the presented nonlinear multivariate control concept. Further, simulation results are presented to get a qualitative understanding of the effects of parameter deviations and the resulting closed loop performance.

The following theoretical considerations and definitions are based on [38]. The full derivations, proofs and further readings can be found in the quoted literature.

4.6.1 Boundedness

Lyapunov stability analyses can be applied to show the boundedness of the states equations, even when there is no equilibrium point at the origin.

Definition The solutions of $\dot{x} = f(t, x)$ are

- uniformly bounded if there exists a positive constant c , independent of $t_0 \geq 0$, and for every $a \in (0, c)$, there is $\beta = \beta(a) > 0$, independent of t_0 , such that

$$\|x(t_0)\| \leq a \quad \Rightarrow \quad \|x(t)\| \leq \beta, \quad \forall t \geq t_0 \quad (4.82)$$

- globally uniformly bounded if Eq. (4.82) holds for arbitrary large a .
- uniformly ultimately bounded with ultimate bound b if there exist positive constant b and c , independent of $t_0 \geq 0$ and for every $a \in (0, c)$, there is $T = T(a, b) \geq 0$, independent of t_0 , such that

$$\|x(t_0)\| \leq a \quad \Rightarrow \quad \|x(t)\| \leq b, \quad \forall t \geq t_0 + T \quad (4.83)$$

- globally uniformly ultimately bounded if Eq. (4.83) holds for arbitrary large a .

To study the boundedness in the sense of Lyapunov, a brief consideration is given. A Lyapunov function $V(x)$ is considered with $V(x) \leq c$, for some $c > 0$. Defining the set Λ as

$$\Lambda = \{\epsilon \leq V(x) \leq c\} \quad (4.84)$$

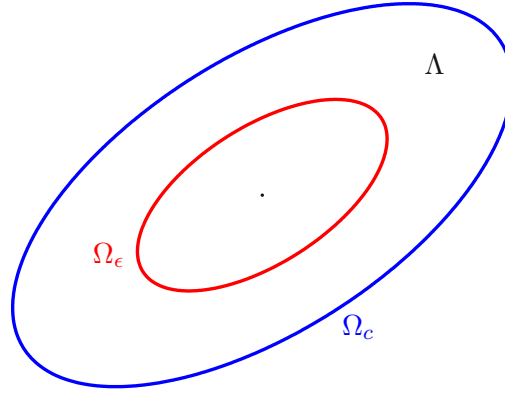
for $0 \leq \epsilon \leq c$ and supposing that the derivative of V along the trajectories of the system $\dot{x} = f(t, x)$ satisfies

$$\dot{V}(t, x) < 0, \quad \forall x \in \Lambda, \quad \forall t \geq t_0. \quad (4.85)$$

This implies that at the boundaries of the sets $\Omega_c = \{V(x) \leq c\}$ and $\Omega_\epsilon = \{V(x) \leq \epsilon\}$ the derivative \dot{V} is negative. A schematic of the sets Λ , Ω_ϵ and Ω_c is given in Fig. 4.8.

Since \dot{V} is negative in the set Λ , a trajectory starting in this set must move in direction of decreasing $V(x)$. In fact, the trajectory behaves as if the origin was uniformly asymptotically stable. Therefore, the function $V(x)$ will continue to decrease until it enters the set Ω_ϵ and stays there for all future time.

In other words: The trajectory starting in Λ converges towards the origin as if it would be stable. After entering the set Ω_ϵ the derivative \dot{V} is not necessarily negative, but on the boundary $\partial\Omega_\epsilon$ the derivative is negative. Therefore, the trajectory stays in this set and is called bounded.

Figure 4.8: Schematic of the set Λ , Ω_ϵ and Ω_c .

4.6.2 Analysis of System Decoupling

In the following the robustness of the closed loop system with respect to parameter uncertainty is analysed. The decoupling of the system is affected if the system parameters deviate from the parameters applied to determine the nonlinear input transformation, which transforms the nonlinear system into linear and decoupled subsystems. To analyse the robustness of the system, the parameter vector is defined as

$$\Theta = [V, \Theta_R, \Theta_c, T_S, \Theta_\gamma, p_0, \Theta_\tau]^T, \quad (4.86)$$

where V is the system volume, p_0 denotes the ambient pressure and Θ_R , Θ_c , Θ_γ and Θ_τ are given by

$$\Theta_R = [R_G, R_S]^T, \quad (4.87)$$

$$\Theta_c = [c_{p,G}, c_{p,S}]^T, \quad (4.88)$$

$$\Theta_\gamma = [\gamma_G, \gamma_S]^T, \quad (4.89)$$

$$\Theta_\tau = [\tau_1, \tau_2, \tau_3, \tau_4]^T, \quad (4.90)$$

where the entries are defined as introduced in Section 3.

As derived in Section 4.5.2, the error dynamics of the system is given by

$$\dot{e} = A_c e + B_c [\beta(x)^{-1} (u - \alpha(x)) - r^{(\delta)}], \quad (4.91a)$$

$$u = \alpha(x) + \beta(x) \nu, \quad (4.91b)$$

$$\nu = \nu_{FF} + \nu_{FB} = r^{(\delta)} - K e, \quad (4.91c)$$

where the determination of the control input u is based on the same parameter set as the system itself and the *synthetic* input ν is a superimposition of feedback and feedforward control. By combining these equations, the resulting error dynamics can be written as

$$\dot{e} = (A_c - B_c K) e, \quad (4.92)$$

where $(A_c - B_c K)$ can be chosen such that the system is stable. This system is referred to as the *nominal* system.

The method of exact linearisation relies on the exact cancelation of $\alpha(x)$ and $\beta(x)$ in Eq. (4.91a), when the control input u given by Eq. (4.91b) is applied. If the determination of the control input is based on a different set of system parameters, than the system itself, than a coupling of the system outputs y will remain.

Considering the system

$$\dot{e} = A_c e + B_c \left[\beta(x)^{-1} (u - \alpha(x)) - r^{(\delta)} \right], \quad (4.93a)$$

$$u = \hat{\alpha}(x) + \hat{\beta}(x) \nu, \quad (4.93b)$$

$$\nu = \nu_{FF} + \nu_{FB} = r^{(\delta)} - K \hat{e}, \quad (4.93c)$$

where $\hat{\alpha}(x)$ and $\hat{\beta}(x)$ denote the parameter variation of the nonlinear decoupling and \hat{e} describes the deviation of the disturbed system output to the reference trajectory. Combining the above equations, the resulting system yields

$$\dot{e} = (A_c - B_c K) e + B_c \delta(e), \quad (4.94)$$

where an additional disturbance term $\delta(e)$ arises, which is given by

$$\delta(e) = \beta(x)^{-1} \left[(\hat{\alpha}(x) - \alpha(x)) + (\hat{\beta}(x) - \beta(x)) (r^{(\delta)} - K e) + \hat{\beta} K (e - \hat{e}) \right]. \quad (4.95)$$

The full derivation of the disturbance term is given in Appendix A.2. The disturbed system Eq. (4.94) appears as a perturbation of the nominal system Eq. (4.92). The disturbance term $\delta(e)$ arises from the incomplete decoupling of the nonlinear system and affects all four decoupled systems. Fig. 4.9 illustrates this effect in the closed loop system. While the nonlinear system (Σ_{Θ_0} block) is based on a parameter set Θ_0 the nonlinear input transformation ($\Sigma_{\Theta_1}^{-1}$ block) is based on a second parameter set Θ_1 . The resulting transformed system is not fully linear and decoupled.

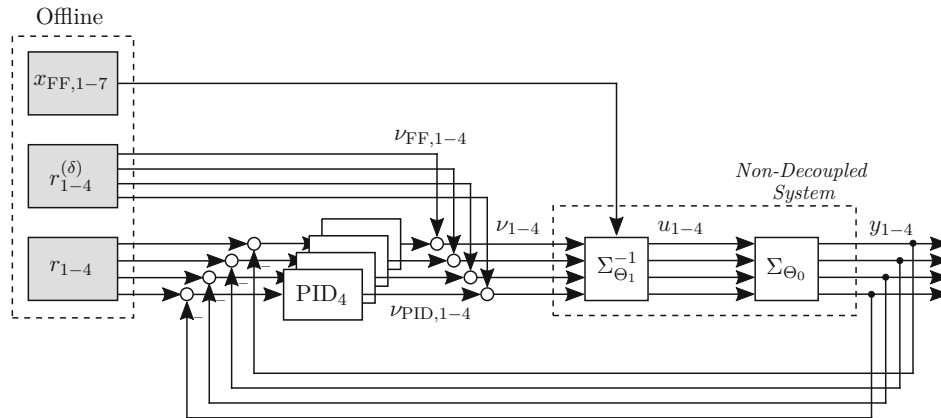


Figure 4.9: Non-Decoupled closed loop system. System parameters Θ_0 differ from parameters Θ_1 , which are used to determine the nonlinear input transformation.

To investigate the stability of the disturbed system Eq. (4.94), the following Lemma from [38] is applied.

Lemma 4.1 Consider the closed-Loop system (4.94), where $(A_c - B_cK)$ is Hurwitz. Let $P = P^T > 0$ be the solution of the Lyapunov equation

$$P(A - BK) + (A - BK)^T P = -I$$

and k be a nonnegative constant less than $1/(2\|PB\|_2)$.

- If $\|\delta(e)\| \leq k\|e\|$ for all e , the origin of (4.94) will be globally exponentially stable.
- If $\|\delta(e)\| \leq k\|e\| + \epsilon$ for all e , the state e will be globally ultimately bounded by ϵc for some $c > 0$.

The proof of this Lemma can be found in the Appendix A.3. For each reference trajectory r , an upper boundary can be calculated in accordance to the Lemma. Fig 4.10 shows the calculated value of $\|\delta(e)\| - k\|e\|$. The plot illustrates that for the reference trajectory r an ϵ can be found, which fulfils the Lemma. Therefore, the closed loop system along this trajectory is robust against this perturbation of the parameters.

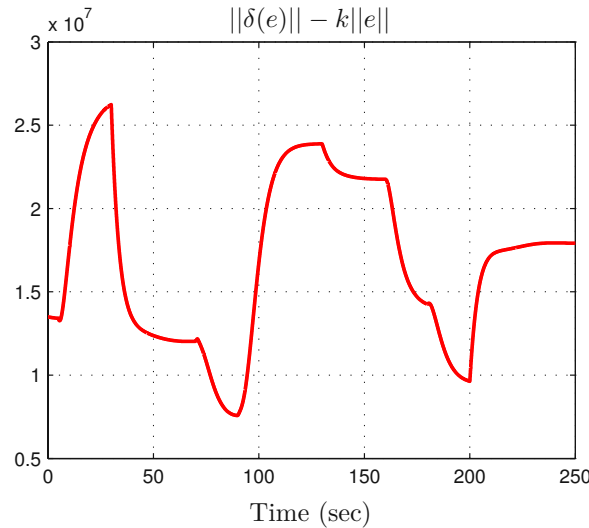


Figure 4.10: Calculated trajectory $\|\delta(e)\| - k\|e\|$ in accordance to Lemma 4.1. For the trajectory, an ϵ can be found, which fulfils the Lemma.

4.6.3 Simulation Results

To analyse the effect of different system parameter deviations and get a qualitative understanding of the impact on the overall system dynamics, sets of different system parameter variations are investigated. Therefore, simulations with a wide variety of parameter sets have been performed. Fig. 4.11 shows a comparison of two parameter varied systems. The system parameters have been varied according to Table 3.3 and the reference trajectories are the same as for the undisturbed closed loop system shown in Fig. 4.6.

The upper plots (Fig. 4.11a and Fig. 4.11b) show the decoupled system, where only feedforward control is applied. The lower plots (Fig. 4.11c and Fig. 4.11d) show the closed loop system with 2DoF control, where feedforward and feedback control is applied. Therefore, the effect of the parameter variation is larger in the upper than in the lower plots. The parameter variations lead to similar results as discussed for the open loop system in Section 3.3.

In Fig. 4.11a, the system volume V is increased and three different cases are investigated. The plot shows that for increasing volume (red - green - blue lines in the plots) the system dynamics is reduced. Since the calculation of the feedforward input, as well as the nonlinear input transformation, does not *know* about the increased system volume, the control input u is calculated based on the parameter set with the low system volume. Therefore, by increasing the system volume the system dynamics is reduced. Additionally, due to the different parameter sets, which are used to calculate the nonlinear decoupling of the system, the decoupling of the system is not perfect and a remaining coupling of the system outputs can be seen. The outflowing mass flow is affected strongest, since the slow pressure build-up directly enters into the nonlinear flow equation.

In Fig. 4.11b, the steam temperature $T_{S, in}$ of the system is changed and three different cases are investigated. The plot shows that for increasing steam temperature (red - green - blue lines in the plots) the system shows an offset behaviour. Since an increased steam temperature introduces additional enthalpy into the system, the system temperature is affected strongest. Due to the strong coupling of the temperature to the relative humidity, an increase in the temperature leads to a decrease in the relative humidity. Additionally, due to the imperfect decoupling, the coupling of the system outputs can be seen.

By applying the designed 2DoF controller to both parameter varied systems, the deviations in the system outputs can be reduced. Fig. 4.11c and Fig. 4.11d show the resulting systems. Due to the feedback part in the control structure, the system output deviations are fed back and a correcting input signal is determined. The plots show that small deviations from the desired trajectories appear, and the controller has to correct the trajectories. The largest deviation is around 1 – 2%, which is sufficiently small. The simulations also show that the flatness-based feedforward calculation of the states x stabilises the decoupling of the system, and no feedback disturbances affect the decoupling matrix. Overall, the resulting closed loop performance shows good performance, even for large parameter deviations.

The effect of measurement noise on the performance of the closed loop system is investigated by applying a normal distributed noise on the system outputs y . The standard deviations for the noise are given in Table 4.1. The deviation is evaluated as the mean squared error of the system output y and the reference trajectories r . Due to the flatness-based calculation of the states x , the noise does not affect the decoupling and the closed loop system shows stable performance for the investigated noise levels.

Measurement Noise	Case 1	Case 2	Case 3
σ_1	0.1 °C	0.5 °C	1 °C
σ_2	0.002 bar	0.01 bar	0.1 bar
σ_3	0.2 %	1 %	5 %
σ_4	0.07 kgh ⁻¹	0.1 kgh ⁻¹	1 kgh ⁻¹
MSE Temperature	$1.6 \cdot 10^{-3}$ °C	$4.0 \cdot 10^{-3}$ °C	$4.6 \cdot 10^{-2}$ °C
MSE Pressure	$2.8 \cdot 10^{-6}$ bar	$3.8 \cdot 10^{-6}$ bar	$6.4 \cdot 10^{-5}$ bar
MSE Relative Humidity	$6.4 \cdot 10^{-4}$ %	$9.5 \cdot 10^{-3}$ %	0.3 %
MSE Mass Flow	$1.3 \cdot 10^{-3}$ kgh ⁻¹	$1.5 \cdot 10^{-3}$ kgh ⁻¹	$3.6 \cdot 10^{-2}$ kgh ⁻¹

Table 4.1: Mean squared error for different magnitudes of measurement noise. The magnitude is given as standard deviation of the normal distribution.

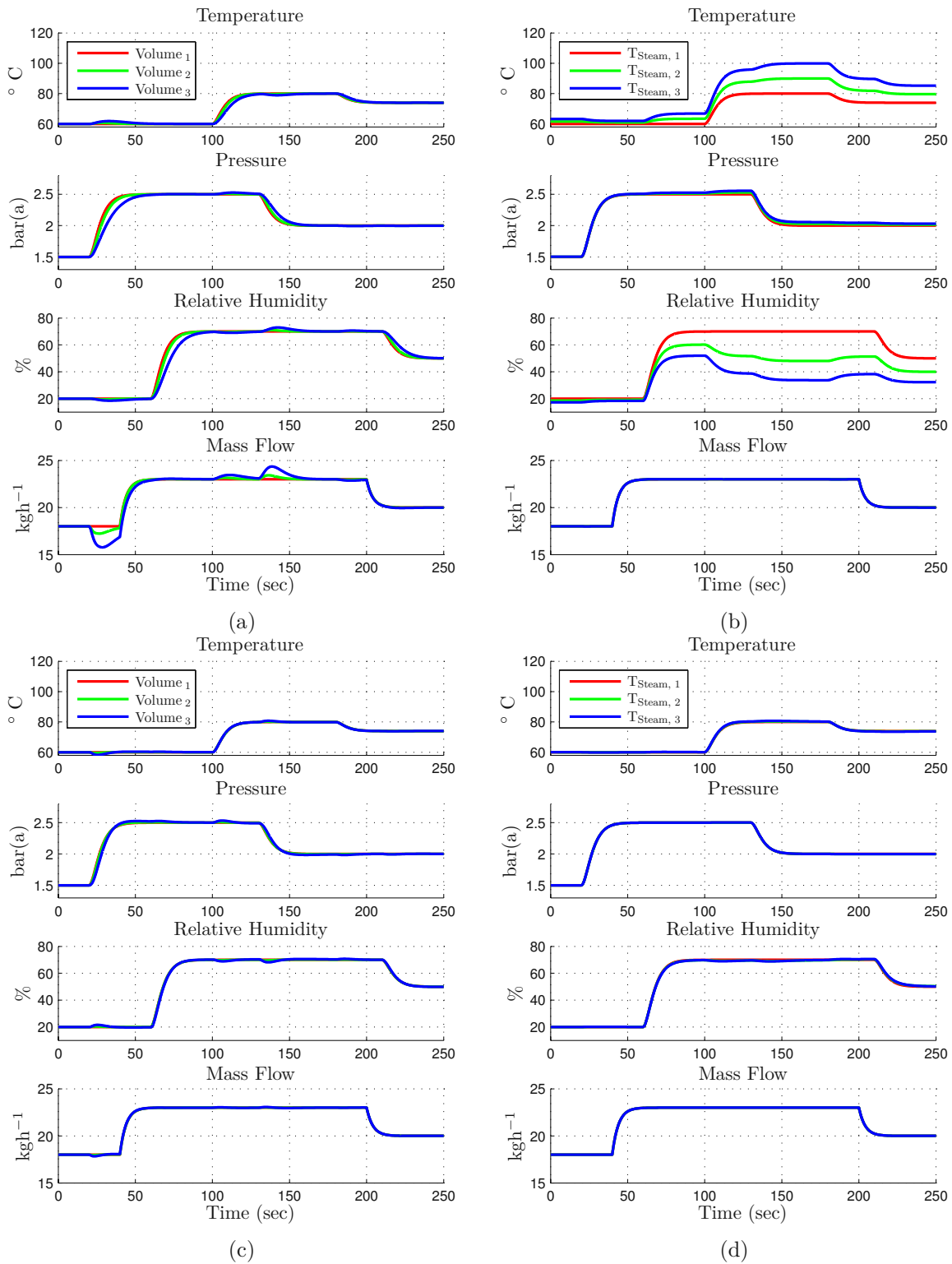


Figure 4.11: The figures show the effect of parameter variations of the system volume and steam temperature on the decoupled system. In plot (a) and (b) only feedforward control is applied. In plot (c) and (d) the designed 2DoF controller is applied.

Chapter 5

Implementation and Measurement

Experimental studies were conducted in order to validate the hardware concept and the implemented nonlinear control concept. In the following, the implementation of the designed nonlinear multivariate control structure, presented in Section 4, on the designed fuel cell stack test bed, presented in Section 2, will be discussed. First, the mechatronical setup will be introduced, which has been used for control and measurements. Second, the control concepts for the submodules, presented in Section 2.1, and an observer for the flow sensor will be discussed. Third, measurement results with the implemented nonlinear multivariate control concept, a linear control scheme as comparison and an extended linear control scheme are presented in order to validate the hardware concept and the designed nonlinear control concept.

5.1 Mechatronical Setup

A schematic of the mechatronic setup is depicted in Fig. 5.1. The nonlinear control algorithm is implemented in Matlab/Simulink and compiled to a *dSpace MicroAutoBox II 1511/1512*, where it runs in a real-time environment. The depicted programmable logic controller (PLC) is mainly used for signal conversion and to provide basic safety measures at the test facility. The fuel cell stack at the test bed is represented by an applied measuring section. It includes

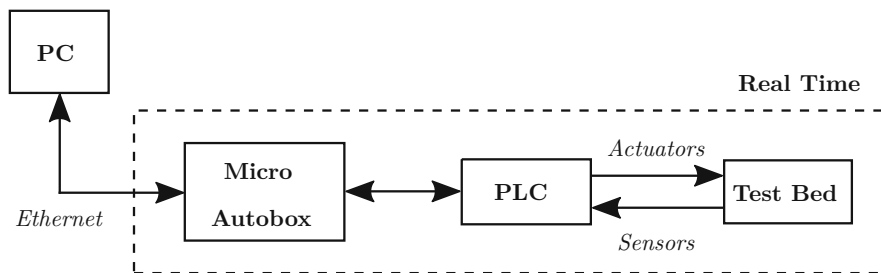


Figure 5.1: Schematic of control setup on test bed.

sensors for air temperature T , pressure p , relative humidity φ and mass flow \dot{m} . The application of a real fuel cell stack would introduce an additional pressure resistance, which is in series with the back pressure valve, and would act as a disturbance on the control. Due to different fuel cell stack designs (e.g. flow field), the pressure drop caused by the stack varies

for different manufacturers. The test bed should be independent of a specific stack design, hence, this is not included in the control design, but regarded as a disturbance.

5.2 Implementation of Low Level Control Structures

As shown in Fig. 3.1, the nonlinear control concept relies on the input variables given by Eq. (3.20). These are not the physical input variables available at the test bed, but *virtual* inputs provided by the submodules as described in Section 2.1. These submodules pose as *virtual* actuators, which map the physical input variables to the *virtual* inputs required by the nonlinear control concept. This can be seen in Eq. (3.20), where these *virtual* inputs are used as control inputs to the nonlinear system model. This approach has the advantage that the resulting nonlinear multivariate control concept is independent of the actual realisation of these submodules. This makes the derived *high level* control structure easily adaptable and scalable to a wide variety of hardware implementations. To provide sufficient dynamics, the mapping of the physical input variables to the *virtual* inputs is done by a combination of cascade controllers and characteristic maps obtained by measurements. This mapping is referred to as *low level* control.

This relation of the nonlinear system model, derived in Section 3.1, to the hardware implementation and input signal mapping is depicted in Fig. 5.2. Fig. 5.2a shows the nonlinear system model with the control inputs u_{1-4} , system states x_{1-7} and system outputs y_{1-4} as described by Eq. (3.22). Fig. 5.2b shows the actual hardware implementation depicted by the block *Test Bed* with the input variables u_{TB} and the system outputs y_{1-4} . These input variables are mapped to the *virtual* inputs u_{1-4} by a combination of cascade controllers and characteristic maps. The resulting system has the same inputs and outputs as the nonlinear system model.

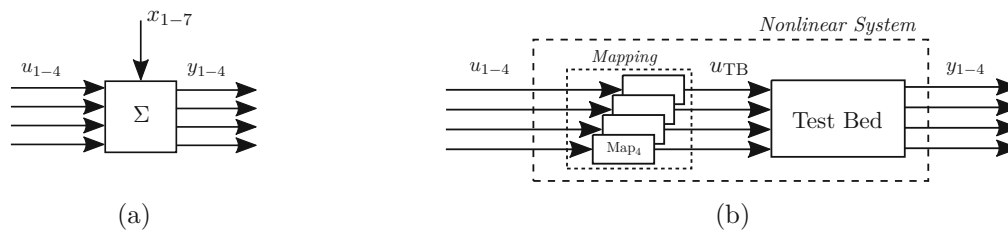


Figure 5.2: Fig. (a) shows the nonlinear system model, which has been used to design the nonlinear multivariate control concept. Fig. (b) shows the nonlinear system with the control inputs u_{TB} and the mapping of these inputs to the *virtual* inputs u_{1-4} used for modelling.

In the following, the *low level* control concepts for the submodules and an observer structure for the mass flow measurement are presented.

5.2.1 Gas Flow Submodule Control

In Fig. 5.3, the *low level* control concept applied for the mass flow concept described in Section 2.1.1 is shown. Fig. 5.3a shows concept A_F with the indicated control input u_p for the pressure controller (PC) and the *virtual* control input \dot{m}_{ref} , which is used as input variable by the nonlinear control concept for this submodule. Fig. 5.3b shows the designed cascade controller with additional feedforward control. The characteristic map (LUT) is used to determine the inlet pressure for the orifice plate (OP) in dependence of the required mass

flow, inlet temperature and outlet pressure of the OP. In Fig. 3.7, the obtained characteristic map from measurements, for the applied OP in the hardware setup, is shown.

The feedforward control applies this pressure directly to the PC, while a linear feedback controller corrects the remaining error. This controller structure is needed due to a build-in PID controller in the PC, which can not be switched off and which uses an internal pressure measurement to correct the output. This internal pressure measurement shows a slight nonlinear offset to the actual achieved output pressure measurement. Due to the limited available test bed time, this was not further investigated. The described control structure showed a good performance for steady state and transient operations.

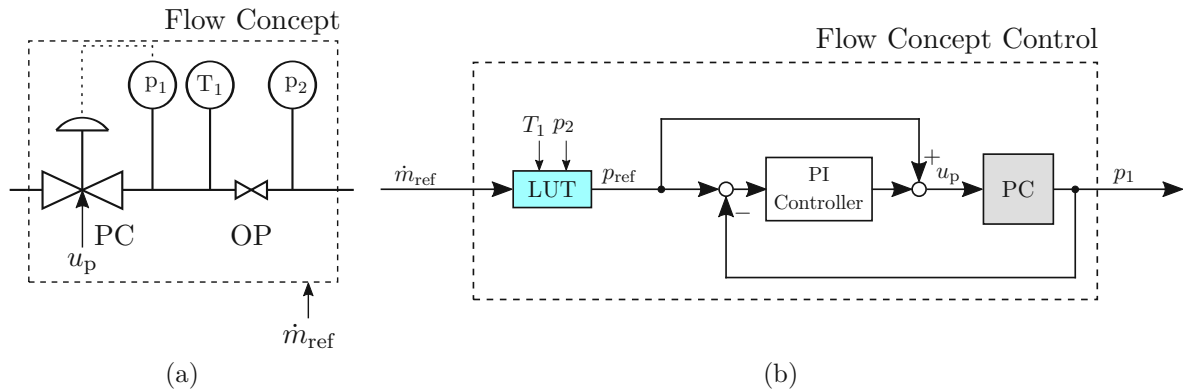


Figure 5.3: Schematic view of the hardware components of the flow concept (a) and the block diagram of the corresponding *low level* control concept (b).

Due to this control structure, the *virtual* input \dot{m}_{ref} is mapped to the available control input at the test bed. The available actuator for this submodule is given by

$$u_{Gas} = u_p. \quad (5.1)$$

5.2.2 Heater Submodule Control

In Fig. 5.4, the *low level* control concept applied for the heating concept described in Section 2.1.2 is shown. Fig. 5.4a shows concept C_H with indicated control inputs u_{V_1} , u_{V_2} and u_{HG} for the control valves (CV_1 , CV_2) and the heat exchanger, respectively. Further, the *virtual* control input T_{ref} is depicted, which is used as input variable by the nonlinear control concept for this submodule.

In Fig. 5.4b, the designed control concept for the heater with bypass is shown. The control structure is divided into two controllers. The lower controller is responsible for a constant set point for the heater. This ensures that the supplied thermal energy of the hot gas stream is nearly constant. Additionally, a control mechanism is implemented to ensure that, if the heat exchanger is active, there is always a minimal gas mass flow to prevent an overheating. Since the heat exchanger can only be switched on or off, the control signal is transformed into a Pulse-Width-Modulated (PWM) signal.

The upper control structure obtains as reference value the control variable T_{ref} , which is used by the nonlinear control concept as *virtual* input. It applies a linear controller to control the direction of the gas mass flow. A sub-controller combines the two control valves to act as one valve. The combined valve control is shown in Fig. 2.7b. Due to this combined valve control, the heater-bypass module poses as single input system for the linear controller. The

control range is 0 - 100 %. Where 0 % means that no mass flow goes through the bypass path while 100 % means that all the mass flow goes through the bypass. The heater-bypass characteristic is shown in Fig. 3.9. The characteristic is used as an additional feedforward control input to increase the dynamic response of the heater-bypass module.

Although the feedforward part proved to improve the transient behaviour of the heater-bypass module in the course of the development of the test bed, it had to be switched off. The rapid change of mass flow in the applied heat exchanger led to a hardware malfunction. This is only due to the specific design of the heat exchanger and could have been avoided by using a different heat exchanger. Due to limited resources in the project, this has been taken into consideration for the redesign.

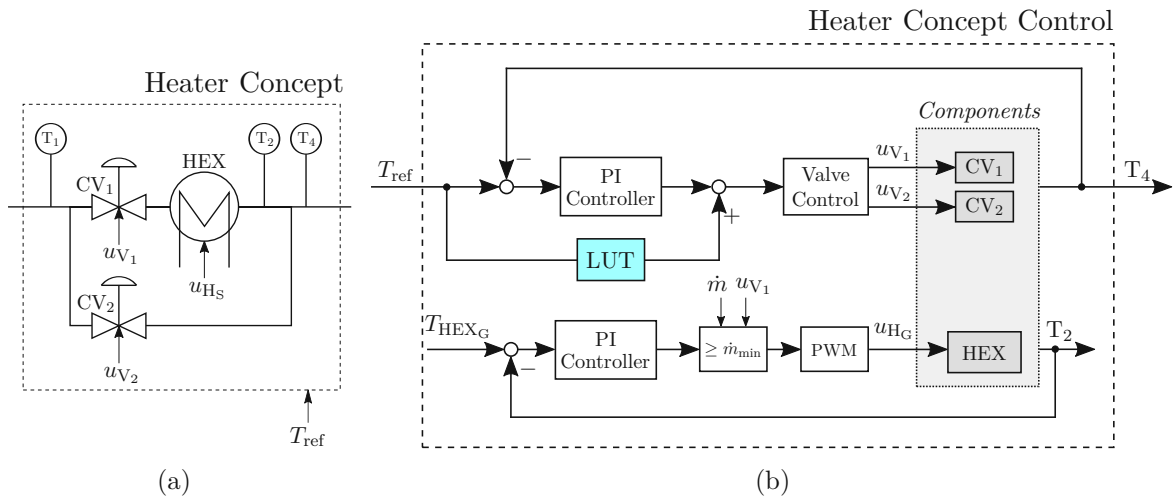


Figure 5.4: Schematic view of the hardware components of the heating concept (a) and the block diagram of the corresponding *low level* control concept (b).

Due to this control structure, the *virtual* input T_{ref} is mapped to the available control inputs at the test bed. The available actuators for this submodule are given by

$$u_{\text{Heater}} = \left[u_{V1}, u_{V2}, u_{HG} \right]^T. \quad (5.2)$$

5.2.3 Steam Flow Submodule Control

In Fig. 5.5, the *low level* control concept applied for the humidification concept described in Section 2.1.3 is shown. Fig. 5.5a shows the control valve and heat exchanger from the humidification concept with the indicated control inputs u_{A_S} and u_{H_S} . Further, the *virtual* control input $\dot{m}_{S, ref}$, which is used as input variable by the nonlinear control concept for this submodule is depicted.

Fig. 5.5b shows the designed control concept for this submodule. The upper control structure shows the control of the steam valve. The control range of the valve is 0 - 100 % of the valve stroke. To map this to the control variable of the nonlinear control concept, the steam valve characteristic from Fig. 3.8a is applied. This maps the valve stroke to an opening area, which can further be used to determine the steam mass flow by utilising sensor measurements and the nonlinear flow equation Eq. (2.1).

The lower control structure shows the control for the overheating of the steam. The set point of the heat exchanger is controlled via a linear controller. Similarly, as for the heater-bypass

module, the control signal for the heat exchanger is transformed into a PWM signal before applied to the test bed.

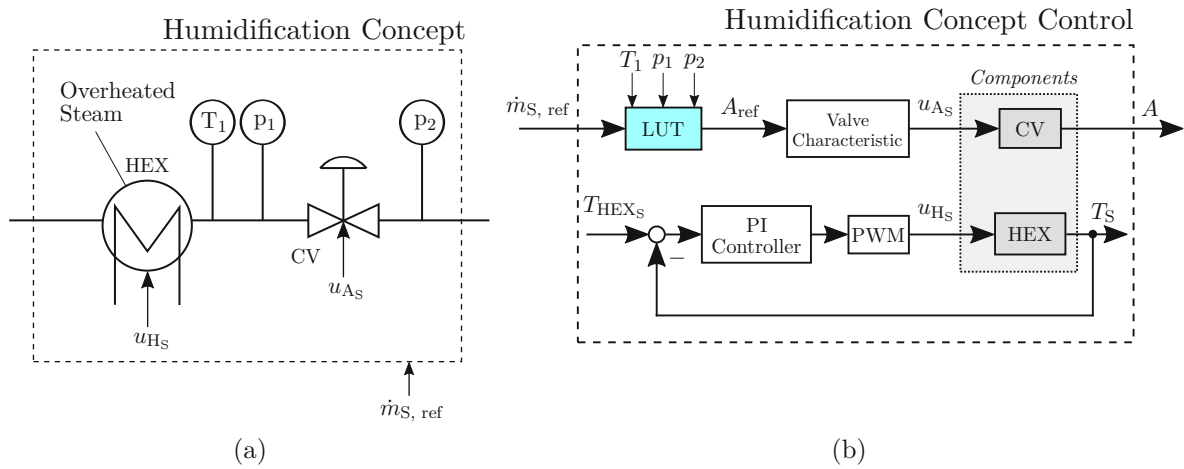


Figure 5.5: Schematic view of the hardware components of the steam concept (a) and the block diagram of the corresponding *low level* control concept (b).

Due to this control structure, the *virtual* input $\dot{m}_{S, ref}$ is mapped to the available control inputs at the test bed. The available actuators for this submodule are given by

$$u_{\text{Steam}} = [u_{AS}, u_{HS}]^T. \quad (5.3)$$

5.2.4 Backpressure Valve Submodule Control

In Fig. 5.6, the *low level* control concept applied for the backpressure concept described in Section 2.1.4 is shown. Fig. 5.6a shows the control valve from the backpressure concept with the indicated control input u_{ABP} for the valve. Further, the *virtual* control input A_{ref} , which is used as input variable by the nonlinear control concept for this submodule is depicted.

Fig. 5.6b shows the designed control concept for this submodule. The control range of the valve is 0 - 100 % of the valve stroke. To map this to the control variable of the nonlinear control concept, the backpressure valve characteristic from Fig. 3.8b is used. This maps the valve stroke to the opening area, which is directly applied in the nonlinear control concept.

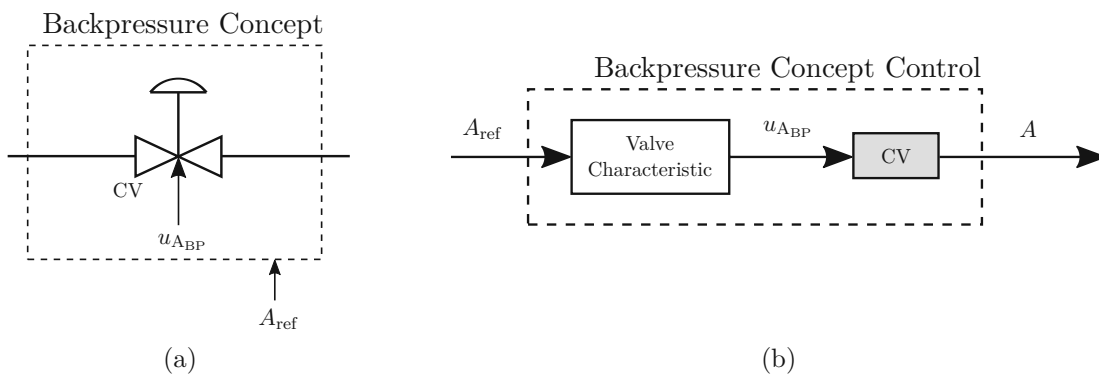


Figure 5.6: Schematic view of the hardware components of the backpressure concept (a) and the block diagram of the corresponding *low level* control concept (b).

Due to this control structure, the *virtual* input A_{ref} is mapped to the available control input at the test bed. The available actuator for this submodule is given by

$$u_{\text{BP}} = u_{\text{ABP}}. \quad (5.4)$$

5.2.5 Mass Flow Observer

The applied coriolis sensor, which is used to measure the mass flow, has been chosen such that the pressure drop is minimal and therefore, the accuracy at lower mass flow ranges is limited. Additionally, the sensor has a measurement lag, which makes it not suitable for transient measurements. Therefore, a *Luenberger* observer [61] for the outflowing mass flow is designed. The observer design is based on the dynamics of the decoupled system given by Eq. (4.60). For mass flow transients, the observer gain is set to zero, which prevents the observer from being affected by the measurement lag. This proved to achieve good results for control. An alternative approach would be applying just feedforward control during mass flow transitions.

5.3 Measurement Results for High Level Controller

The presented combination of cascade controllers and characteristic maps map the *virtual* control inputs to the available actuators at the test bed. The available actuators are given by

$$u_{\text{TB}} = \left[u_{\text{Gas}}, u_{\text{Heater}}, u_{\text{Steam}}, u_{\text{BP}} \right]^T, \quad (5.5)$$

where the control inputs for the submodules are given by Eq. (5.1), Eq. (5.2), Eq. (5.3) and Eq. (5.4). The selected hardware components implemented in the test bed are listed in Table 5.1. Due to limitation of the applied hardware and constraints at the test facility, not the full operating range is available for validation measurements of the *high level* controller. Nonetheless, the control concepts and overall hardware performance, can sufficiently be tested in the available subrange of the operating range. In the following, three different control approaches will be presented and compared to each other.

First, the presented model-based nonlinear multivariate control concept will be implemented. Second, as comparison a linear PID control structure is designed, which can be seen as standard approach for industrial applications. Third, the model-based system knowledge can be exploited to design a feedforward control extension to the introduced linear PID control structure. This additional feedforward control utilises the concepts from the nonlinear control design and significantly improves the performance of the linear controller.

As reference signal, a random trajectory $r(t)$ is generated for all four system outputs. The signal shape is generated in accordance with the relative degree of the system outputs y_{1-4} . Due to the high thermal inertia of the system, the reference trajectory for the system temperature has been chosen considerably slower than the other trajectories. As discussed in Section 5.2.5, the control of the mass flow is based on an observer. Therefore, both measurement and observer signals are shown in the mass flow plots.

As control input signals, the actual measured signals of the actuators at the test bed are given. Except for the heater module, since the control valves do not possess a stroke sensor. Therefore, the measured gas temperature is given as reference, which poses a *virtual* input to the system.

Component	Hardware Type	Specifications
Fig. 2.2a, PC	Pressure Regulator	$T_{90} < 0.1 \text{ sec}$
Fig. 2.2a, OP	Orifice Plate	$\varnothing 2.5 \text{ mm}$
Fig. 2.4c, CV ₁	Seat Valve	$C_{vs} 0.92$
Fig. 2.4c, CV ₂	Seat Valve	$C_{vs} 1.39$
Fig. 2.4c, HEX	Heat Exchanger	800 W
Fig. 2.9, D ₁	Saturated Steam Boiler	42.5 kg h ⁻¹ at 6 bar(a)
Fig. 2.9, CV	Sliding Gate Valve	$C_{vs} 1.27$
Fig. 2.10b, CV	Sliding Gate Valve	$C_{vs} 9.24$

Table 5.1: Hardware components implemented in the test bed.

The numeric values of the standard deviations of output signal to the reference trajectory are given for two cases. First, data obtained from stationary measurements and second, data obtained from dynamic measurements. For the stationary measurements, the reference trajectories are kept constant. For the dynamic measurements, the whole reference trajectory is evaluated.

5.3.1 Nonlinear Multivariate Control

In the following, measurement results for the nonlinear multivariate control structure, which has been introduced in Section 4.5, are shown. The actual resulting implemented control structure on the test bed is shown in Fig. 5.7. Similar to Fig. 4.5, the decoupling block Σ^{-1} acts on the nonlinear system and transforms it to four linear and decoupled systems. For the resulting SISO systems, four linear controllers are applied. Each with feedback and feedforward control. The nonlinear system itself consists of the test bed and the controllers for the actuator signal mapping.

The used parameter configuration of the four 2DoF controllers is given in Table C.1.

The measurement results for the implemented nonlinear controller are shown in Fig. 5.8. Fig. 5.8b shows the reference trajectories in blue and the measured sensor signals in red. The standard deviation is indicated in dashed blue lines. The plots show that the controller successfully decouples the system and the system outputs y_{1-4} can independently follow their desired reference trajectories. Small couplings of the outputs remain, which are corrected by the 2DoF controller. Overall, the controller shows good trajectory tracking and disturbance rejection behaviour.

The corresponding control variables u are shown in Fig.5.8a. Due to the high thermal inertia of the system, the 2DoF control for the gas temperature has been parameterised such that the time constant is very small. Therefore, it behaves almost like a two-point controller. This leads to the control performance shown in the second plot in Fig.5.8a. The control input variation is very fast, but the output functions given in Fig. 5.8b show a good performance. The resulting limit cycle of the temperature is in an acceptable range and can be seen in the upmost plot of Fig. 5.8b.

The numeric values of the standard deviations obtained from stationary and dynamic measurements are presented in Table 5.2.

Although the evolution of the state space system, as shown in Fig. 4.7, does not include information about the time evolution, it gives additional insight into the system behaviour.

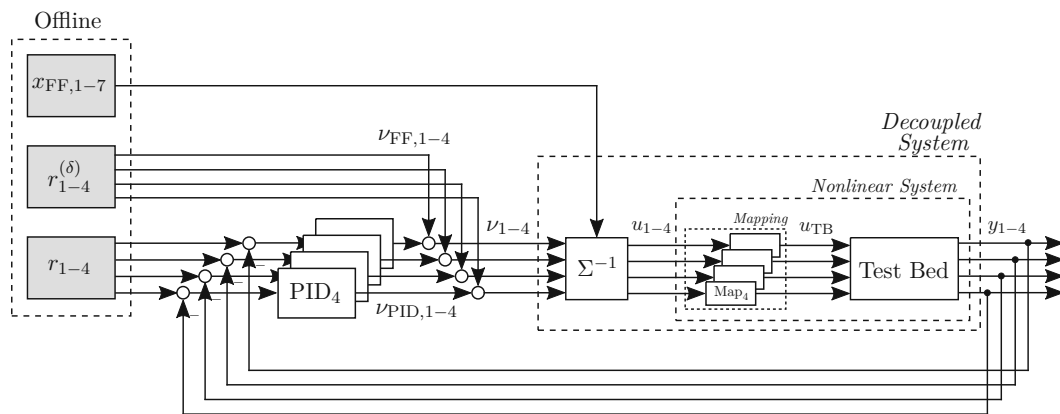


Figure 5.7: Block diagram of the Two-Degree-of-Freedom (2DoF) controller. To each decoupled linear system, a PID controller is applied. The control variables of the nonlinear decoupling block are mapped to the actual actuator inputs of the test bed.

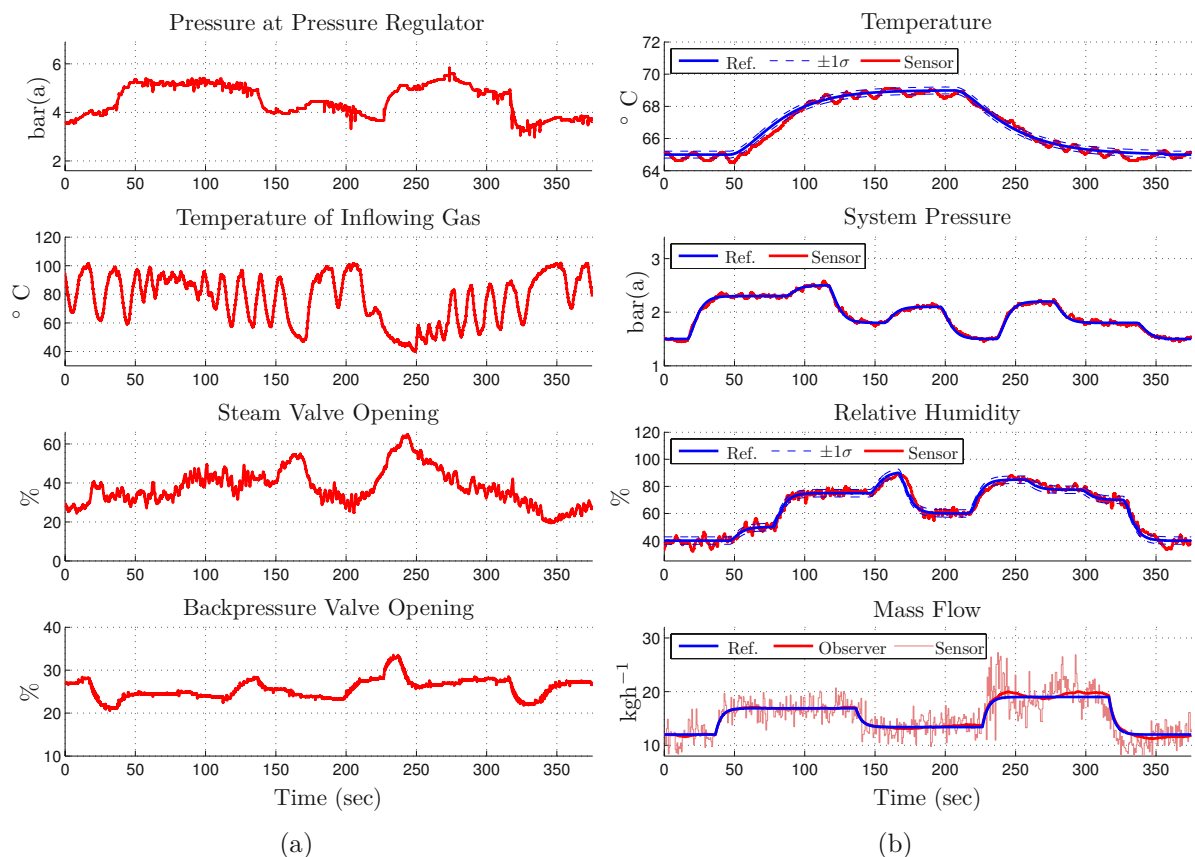


Figure 5.8: Control performance of nonlinear control concept applied on the nonlinear and coupled test bed. Plot (a) shows the sensor signals of the control variables. Plot (b) shows the output of the nonlinear system in red and the reference trajectories in blue.

Output	σ_{stat}	σ_{dyn}
T	0.16 °C	0.21 °C
p	0.03 bar(a)	0.03 bar(a)
φ	2.60 %	2.75 %
\dot{m}_{out} (Obs.)	0.17 kgh ⁻¹	0.50 kgh ⁻¹
\dot{m}_{out} (Sens.)	1.79 kgh ⁻¹	2.20 kgh ⁻¹

Table 5.2: Standard deviations for stationary and dynamic measurements of nonlinear control concept.

The deviation of the system from the reference trajectory shows the accuracy with which the system can follow the trajectory in state space.

Since the states are not directly accessible through measurements, the evaluation is based on applying the system property of flatness to estimate the state variables.

Fig. 5.9 shows state evolution of the closed loop measurement from Fig. 5.8. Fig. 5.9a shows the three dimensional plot while Fig. 5.9b shows a two dimensional projection. The system boundaries are illustrated as grey surface areas. The reference trajectory is shown in blue and the measurements are given in red. Fig. 5.9c shows a zoomed view of the three dimensional representation given in Fig. 5.9a.

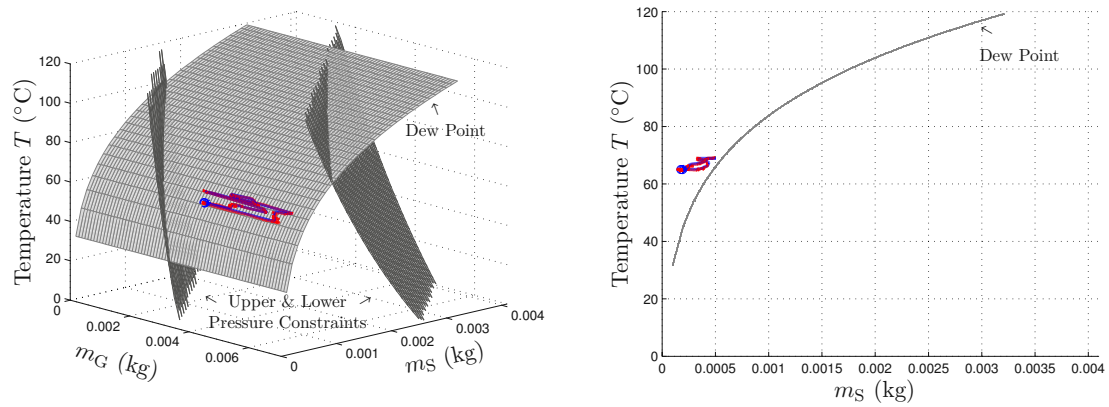
Due to limitations in the hardware setup, the operating range of the test bed was constrained to a small subset of the defined range. Nonetheless the system shows good behaviour in the state space and the reference trajectory can sufficiently be followed. The large measurement noise of the humidity sensor is reflected in the large variation of the estimated steam content state variable m_S , which is depicted on the y-axis.

5.3.2 Linear Control

In the following, a linear control structure is designed to compare its performance with the presented nonlinear control concept. The designed nonlinear control structure is based on the derived system model presented in Section 3.1. This system model has the *virtual* inputs u_{1-4} as input variables, as shown in Fig. 5.2a. To allow for a comparison, the linear controllers act on the nonlinear system shown in Fig. 5.2b.

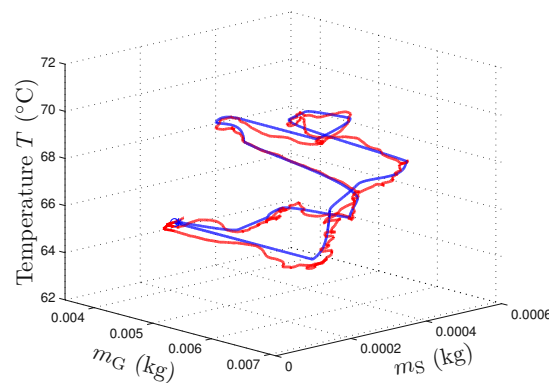
Fig. 5.10 shows the designed linear control structure for control of the nonlinear and coupled test bed. The control parameters are given in Table C.2.

Fig. 5.11 shows the measurement results for the linear control structure. Fig. 5.11b shows the reference trajectories in blue and the system output in red. The standard deviation is indicated in dashed blue lines. Fig. 5.11a shows the corresponding control inputs to the system. The former plot shows that especially during transitions of one of the system outputs a deviation of the other system outputs occur. This is due to the coupling of the system. The standard deviation from the reference signal is given in Table 5.3. From the relative humidity plot, it is obvious that during transients the maximum deviation exceeds the operating limits of the system and condensation occurs (e.g. at 320 sec). This control concept neither ensures the decoupling of the system nor does it prevent the test bed to flood the fuel cell stack. Additionally, the coupling of the system leads to coupling of the linear controllers, since they are not independent anymore. For certain combination of set point variations this leads to large limit cycles, which would damage the fuel cell stack. Therefore, it can be concluded that



(a) Closed loop measurement - 3D view.

(b) Closed loop measurement - 2D view.



(c) Closed loop measurement - 3D zoomed view.

Figure 5.9: The figures show the closed loop system following a reference trajectory in state space. Measurements are given in red and the reference trajectory in blue. Plot (a) is a 3D representation where the system constraints are indicated as grey surface areas. Plot (b) is a 2D projection of (a). Plot (c) is a zoomed 3D view.

this concept does not provide a viable control for the coupled nonlinear system. Nonetheless it provides a reference and a starting point for improvements.

The evolution in the system state space is shown in Fig. 5.12. The reference trajectory is shown in blue and the measurements are given in red. The system shows large deviation and is considerably worse than Fig. 5.9c.

5.3.3 Linear Control with additional Model-based Feedforward Control

The introduced PID control structure can be adapted by a nonlinear model-based feedforward control part, which is based on the presented concept of exact input-output linearisation. It is to be noted that in contrast to the presented nonlinear control concept, the PID controllers still act on the control inputs of the nonlinear system. Since every correcting action of the PID controllers act on the coupled system, the additional feedforward control does not fully decouple the nonlinear system. The resulting control structure is shown in Fig. 5.13. By comparing this to Fig. 5.10, it can be seen that the feedforward control part represents an

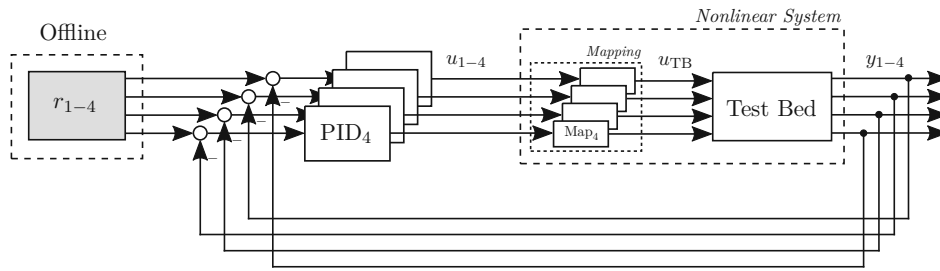


Figure 5.10: Linear control structure for control of nonlinear and coupled test bed.

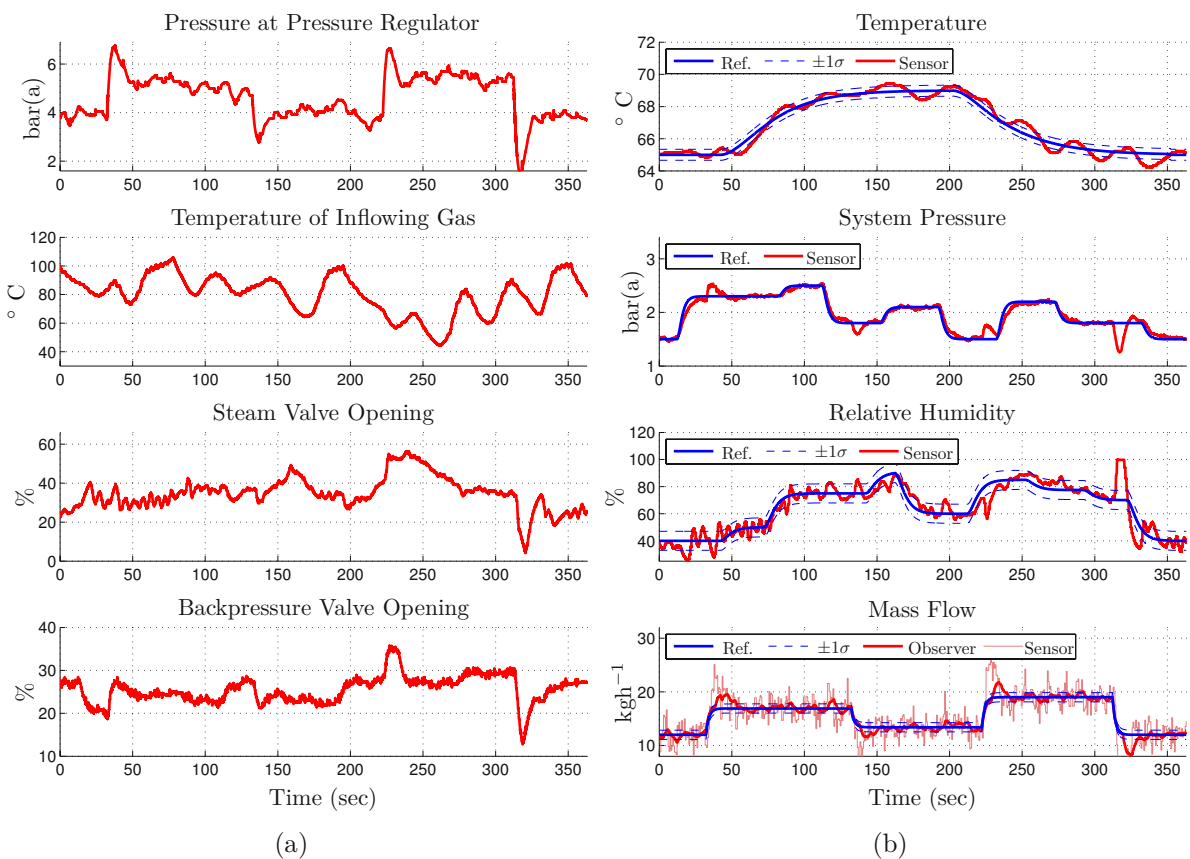


Figure 5.11: Control performance of linear controllers applied on the nonlinear and coupled test bed. Plot (a) shows the sensor signals of the control variables. Plot (b) shows the output of the nonlinear system in red and the reference trajectories in blue.

Output	σ_{stat}	σ_{dyn}
T	0.24 °C	0.34 °C
p	0.03 bar(a)	0.09 bar(a)
φ	3.69 %	7.04 %
\dot{m}_{out} (Obs.)	0.18 kgh ⁻¹	0.85 kgh ⁻¹
\dot{m}_{out} (Sens.)	1.75 kgh ⁻¹	2.49 kgh ⁻¹

Table 5.3: Standard deviations for stationary and dynamic measurements of linear control structure.

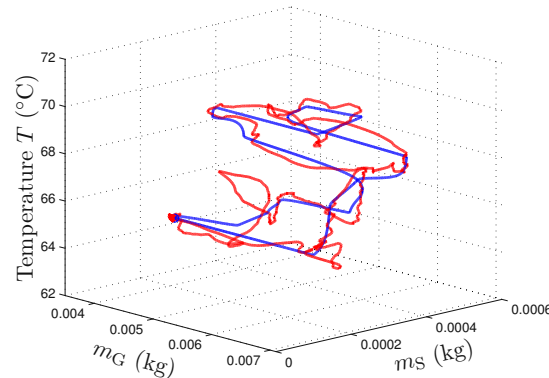


Figure 5.12: State evolution of closed loop system with linear control structure. The reference trajectory is shown in blue, measurements are shown in red.

extension of the linear control structure to a 2 DoF control structure. The control parameters for the PID controllers are listed in Table C.3.

Measurement results for the closed loop performance are shown in Fig. 5.14. In Fig. 5.14b, the system outputs y_{1-4} are shown. The reference trajectory is indicated in blue and the system outputs in red. The standard deviation is indicated in dashed blue lines. The numerical values for the standard deviation are listed in Table 5.4. The performance of this extended control structure is clearly better than the linear control structure. Although some couplings remain, the magnitude of the deviation is much smaller. This is also reflected in the standard deviations. The system temperature shows a larger oscillation than the temperature variation with the linear control structure. This is due to a different tuning of the corresponding PID controller.

The system evolution in the state space is depicted in Fig. 5.15. Due to the large temperature oscillations of the system, this figure is not conclusive.

Output	σ_{stat}	σ_{dyn}
T	0.45 °C	0.67 °C
p	0.03 bar(a)	0.03 bar(a)
φ	2.46 %	3.12 %
\dot{m}_{out} (Obs.)	0.20 kgh ⁻¹	0.29 kgh ⁻¹
\dot{m}_{out} (Sens.)	1.90 kgh ⁻¹	2.08 kgh ⁻¹

Table 5.4: Standard deviations for stationary and dynamic measurements of linear control concept with additional model-based feedforward control.

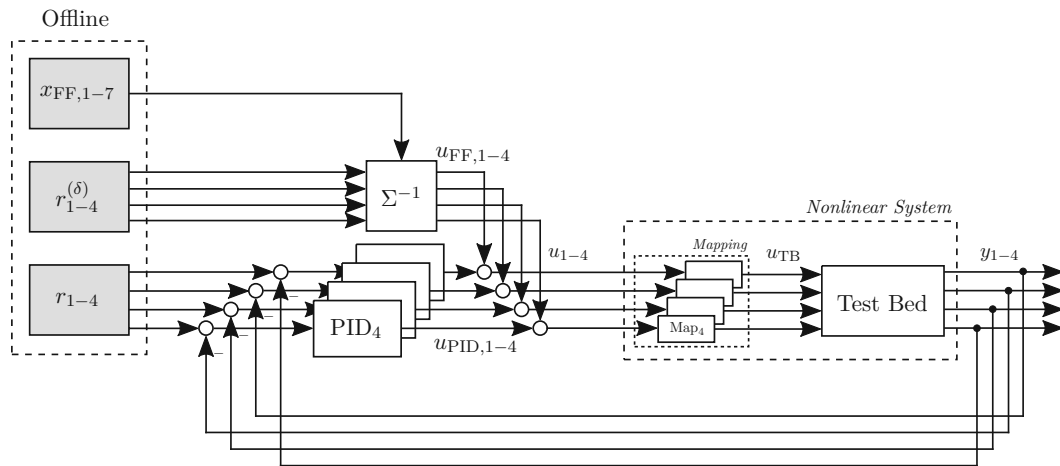


Figure 5.13: Linear control structure with additional model-based feedforward control for control of nonlinear and coupled test bed.

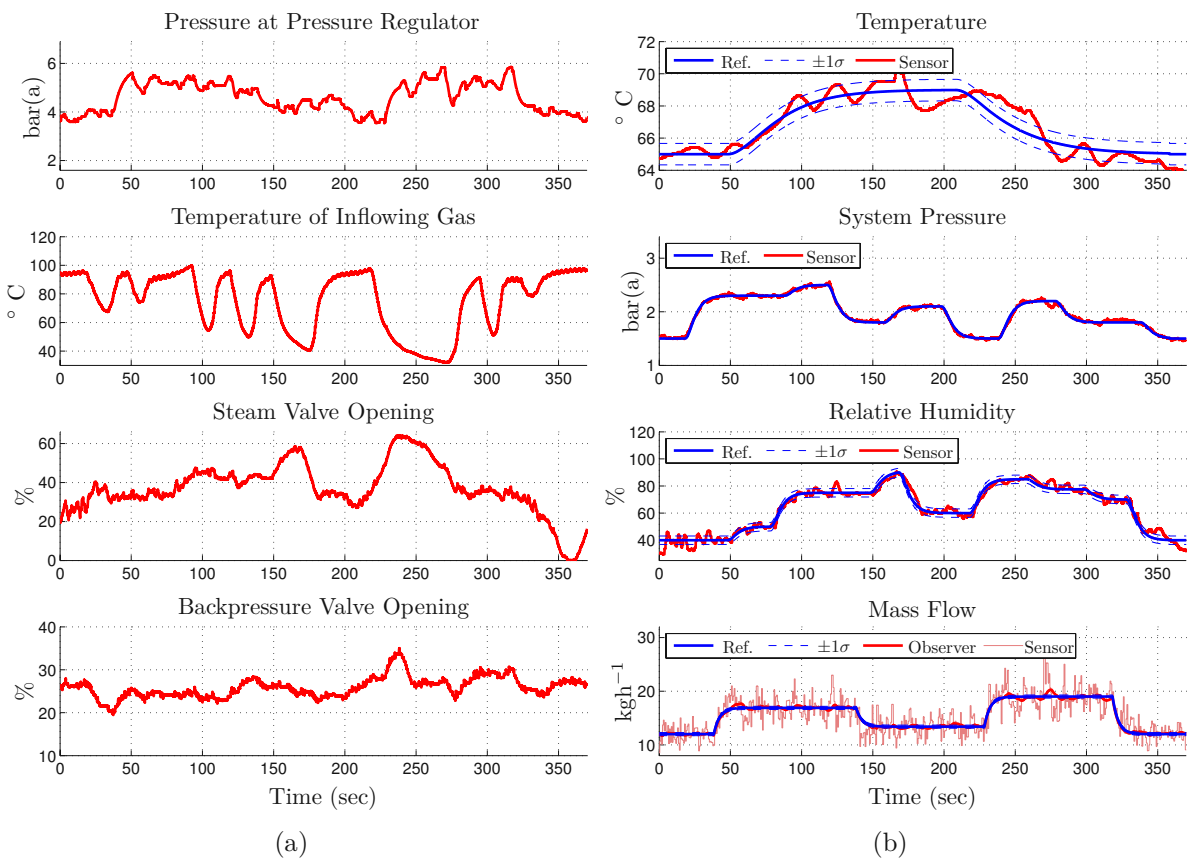


Figure 5.14: Control performance of linear controllers with additional model-based feedforward control applied on the nonlinear and coupled test bed. Plot (a) shows the sensor signals of the control variables. Plot (b) shows the output of the nonlinear system in red and the reference trajectories in blue.

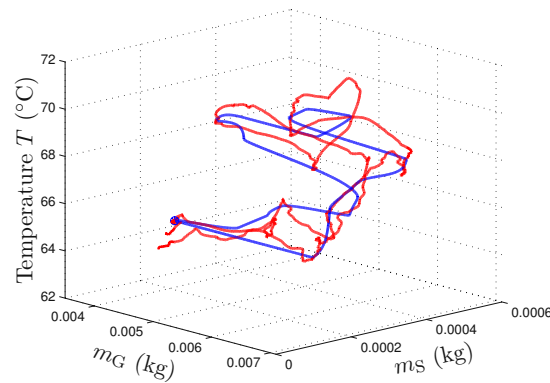


Figure 5.15: State evolution of closed loop system with linear control structure and additional model-based feedforward control. The reference trajectory is shown in blue, measurements are shown in red.

5.3.4 Discussion of Control Performances

The comparison of Fig. 5.8, Fig. 5.11 and Fig. 5.14 shows that the nonlinear control concept ensures trajectory tracking during dynamic set point changes, while the linear controller shows an insufficient performance. However, by extending the linear control structure with an additional model-based feedforward control, the performance is significantly improved. The obtained standard deviations in Table 5.2, Table 5.3 and Table 5.4 show the quantitative improvement and endorse the former statement.

The state space evolution given in Fig. 5.9, Fig. 5.12 and Fig. 5.15 also show clearly that the nonlinear control concept significantly outperforms the other concepts. However, for the results of the expansion of the linear control structure with the additional model-based feedforward control the figures are not conclusive, since the large temperature fluctuation affect the states space trajectories as well.

The concept of extending a linear control structure with nonlinear model-based feedforward control is a suitable and promising approach for upgrading already operational test beds. The implementation *only* requires to superimpose the control inputs with the additional feedforward signal. The operational linear control structure does not need to be altered.

Chapter 6

Conclusions and Outlook

In order to develop PEM fuel cell technologies, manufacturers rely on high-performance testing environments. Especially in automotive applications the fuel cell stack is operated under highly dynamic conditions, which means that the set points are changed continuously during operation. In order to successfully integrate the fuel cell system into the electric power train, transient testing is of particular interest. In this thesis, a novel approach for hardware and control design of the gas conditioning system of such a transient test infrastructure was proposed.

First, different hardware concepts were tested and evaluated in order to provide the stack with an inflowing gas mass flow, gas temperature, relative humidity of the inflowing gas and stack pressure. Based on the evaluation, a modular test setup was constructed. During the prototyping this modular concept proved to be highly efficient in order to minimise the downtime of the test bed. Humidity control for temperature ranges below 100 °C is challenging and requires that parts of the test bed piping are heated and isolated in order to avoid condensation. Further, the injected steam needs to be overheated in order to compensate for the thermal inertia of the system and to avoid condensation.

Second, based on the constructed test bed a dynamic nonlinear system model was derived. This model incorporates the essential dynamic properties, nonlinearities and thermodynamic couplings of the system. At the same time, the model structure has a manageable model complexity and therefore can be applied for the design of a model-based controller. Further, the system model accounts for the modularity of the designed test bed by being flexible and scalable to hardware adaptations. The model is derived from first principles and extended with the actuator dynamics and parameters, which enable the model to be accurately fitted to measurements from the test bed.

Third, measurements from the test bed and the analysis of the dynamic system model proved that the system is highly nonlinear, multivariate and coupled in many ways. Therefore, a model-based nonlinear multivariate control strategy was designed. The designed control concept deals with the nonlinearities and couplings of the multivariate system by transforming the system into multiple linear single-input single-output systems for which, each, feedforward and feedback control was designed.

Fourth, the performance of the realised hardware concept and applied nonlinear control concept was demonstrated. Measurement results for the closed loop system validate the realised hardware setup and show the performance of the nonlinear control concept. The designed controller ensures trajectory tracking during dynamic set point changes. Further,

the model-based feedforward controller can be applied to a standard linear controller, which, itself, shows an insufficient performance for the nonlinear coupled system. The extension of the linear control structure with additional model-based feedforward control significantly improved the performance.

The successful design and application of a transient testing environment for fuel cell stacks is a very promising result for future dynamic HiL fuel cell stack test beds. Further improvements of the overall system may include reducing the thermal inertia of the system by implementing the test bed in a more compact hardware setup. This can be achieved by reducing the length of piping and applying plastic piping where possible. Further, the dynamic response of the system can be increased by replacing components (i.e. heater module), with slow dynamics and by providing the test bed with high pressurised gas and large mass flow quantities in order to enable fast pressure build-ups.

Appendix A

Mathematics

A.1 State Space Coordinate Transformation

Consider the following state space system

$$\begin{aligned} \dot{z} &= A_c z + B_c \gamma(x) (u - \alpha(x)), & \gamma(x) &= \beta(x)^{-1}, \\ y &= C_c z, \end{aligned} \tag{A.1}$$

where z is a (7×1) vector, $\gamma(x)$ is a (4×4) matrix, u is a (4×1) vector, $\alpha(x)$ is a (4×1) vector and the matrices A_c , B_c and C_c as defined by Eq. (4.58).

The reference trajectory $r(t)$ for the system is defined as

$$r(t) = [r_1, r_2, r_3, r_4]^T. \tag{A.2}$$

The derivative of the reference trajectory, which contains the δ -th time derivative of each component, where δ_j is the relative degree of the system output y_j , is defined as

$$r^{(\delta)} = [\ddot{r}_1, \ddot{r}_2, \ddot{r}_3, \dot{r}_4]^T. \tag{A.3}$$

The state variable z is defined by Eq. (4.54) and is given as

$$z = [z_1, z_2, z_3, z_4, z_5, z_6, z_7]^T \tag{A.4}$$

$$= [y_1, \dot{y}_1, y_2, \dot{y}_2, y_3, \dot{y}_3, y_4]^T. \tag{A.5}$$

The corresponding reference trajectory R , which also contains the δ_{j-1} -th time derivative for each r_j , is given by

$$R = [r_1, \dot{r}_1, r_2, \dot{r}_2, r_3, \dot{r}_3, r_4]^T. \tag{A.6}$$

The deviation of the system from the reference trajectory is defined as

$$\bar{e} = z - R = [\bar{e}_1, \bar{e}_2, \bar{e}_3, \bar{e}_4]^T, \tag{A.7}$$

where the components are given by

$$\bar{e}_1 = \begin{bmatrix} e_{1,1} \\ e_{1,2} \end{bmatrix} = \begin{bmatrix} z_1 \\ z_2 \end{bmatrix} - \begin{bmatrix} r_1 \\ \dot{r}_1 \end{bmatrix}, \quad (\text{A.8})$$

$$\bar{e}_2 = \begin{bmatrix} e_{2,1} \\ e_{2,2} \end{bmatrix} = \begin{bmatrix} z_3 \\ z_4 \end{bmatrix} - \begin{bmatrix} r_2 \\ \dot{r}_2 \end{bmatrix}, \quad (\text{A.9})$$

$$\bar{e}_3 = \begin{bmatrix} e_{3,1} \\ e_{3,2} \end{bmatrix} = \begin{bmatrix} z_5 \\ z_6 \end{bmatrix} - \begin{bmatrix} r_3 \\ \dot{r}_3 \end{bmatrix}, \quad (\text{A.10})$$

$$\bar{e}_4 = [e_{4,1}] = [z_7] - [r_4]. \quad (\text{A.11})$$

Inserting Eq. (A.7) into Eq. (A.1) leads to

$$\underbrace{(\dot{\bar{e}} + \dot{R})}_{\dot{z}} = A_c \underbrace{(\bar{e} + R)}_z + B_c \gamma(x) (u - \alpha(x)), \quad (\text{A.12})$$

which can be reformulated to

$$\dot{\bar{e}} = A_c \bar{e} + B_c \gamma(x) (u - \alpha(x)) + A_c R - \dot{R}, \quad (\text{A.13})$$

where the last two terms can be combined to

$$A_c R - \dot{R} = \begin{bmatrix} \dot{r}_1 \\ 0 \\ \dot{r}_2 \\ 0 \\ \dot{r}_3 \\ 0 \\ 0 \\ 0 \end{bmatrix} - \begin{bmatrix} \dot{r}_1 \\ \ddot{r}_1 \\ \dot{r}_2 \\ \ddot{r}_2 \\ \dot{r}_3 \\ \ddot{r}_3 \\ \dot{r}_4 \\ \ddot{r}_4 \end{bmatrix} = - \begin{bmatrix} 0 \\ \ddot{r}_1 \\ 0 \\ \ddot{r}_2 \\ 0 \\ \ddot{r}_3 \\ \dot{r}_4 \\ \ddot{r}_4 \end{bmatrix} = -B_c r^{(\delta)}. \quad (\text{A.14})$$

Therefore, Eq. (A.13) can be rewritten as the error dynamics of the system as

$$\dot{\bar{e}} = A_c \bar{e} + B_c [\gamma(x) (u - \alpha(x)) - r^{(\delta)}]. \quad (\text{A.15})$$

Further, the error vector can additionally be expanded by introducing an integral component. The components of the expanded error vector are given by

$$e_j = \begin{bmatrix} e_{j,0} \\ e_{j,1} \\ e_{j,2} \end{bmatrix} = \begin{bmatrix} \int (z_{2j-1} - r_j) dt \\ z_{2j-1} - r_j \\ z_{2j} - \dot{r}_j \end{bmatrix} = \begin{bmatrix} e_{j,0} \\ \bar{e}_j \end{bmatrix}, \quad j = 1, 2, 3 \quad (\text{A.16})$$

$$e_4 = \begin{bmatrix} e_{4,0} \\ e_{4,1} \end{bmatrix} = \begin{bmatrix} \int (z_7 - r_4) dt \\ z_7 - r_4 \end{bmatrix} = \begin{bmatrix} e_{4,0} \\ \bar{e}_4 \end{bmatrix}. \quad (\text{A.17})$$

Applying the time derivative to components of the expanded error vector yields

$$\dot{e}_j = \begin{bmatrix} z_{2j-1} - r_j \\ \dot{z}_{2j-1} - \dot{r}_j \\ \dot{z}_{2j} - \ddot{r}_j \end{bmatrix} = \begin{bmatrix} e_{j,1} \\ \dot{e}_j \end{bmatrix}, \quad j = 1, 2, 3 \quad (\text{A.18})$$

$$\dot{e}_4 = \begin{bmatrix} z_7 - r_4 \\ \dot{z}_7 - \dot{r}_4 \end{bmatrix} = \begin{bmatrix} e_{4,1} \\ \dot{e}_4 \end{bmatrix}, \quad (\text{A.19})$$

which can be formulated as the error dynamics in the new expanded error vector

$$\dot{e} = A_c e + B_c \left[\gamma(x) (u - \alpha(x)) - r^{(\delta)} \right] \quad (\text{A.20})$$

with A_c and B_c defined as in Eq. (4.58), but the components $A_{c,1-4}$ and $B_{c,1-4}$ are given by

$$A_{c,j} = \begin{bmatrix} 0 & 1 & 0 \\ 0 & 0 & 1 \\ 0 & 0 & 0 \end{bmatrix}, \quad B_{c,j} = \begin{bmatrix} 0 \\ 0 \\ 1 \end{bmatrix}, \quad j = 1, 2, 3 \quad (\text{A.21})$$

$$A_{c,4} = \begin{bmatrix} 0 & 1 \\ 0 & 0 \end{bmatrix}, \quad B_{c,4} = \begin{bmatrix} 0 \\ 1 \end{bmatrix}. \quad (\text{A.22})$$

A.2 Derivation of Disturbance Term for Nominal System

Considering the transformed system from Eq. (4.72) with Eq. (4.73) and Eq. (4.74)

$$\dot{e} = A_c e + B_c \left[\gamma(x) (u - \alpha(x)) - r^{(\delta)} \right], \quad \gamma = \beta(x)^{-1}, \quad (\text{A.23a})$$

$$u = \hat{\alpha}(x) + \hat{\beta}(x) \nu, \quad (\text{A.23b})$$

$$\nu = \nu_{\text{FF}} + \nu_{\text{FB}} = r^{(\delta)} - K \hat{e}, \quad (\text{A.23c})$$

where $\hat{\alpha}(x)$ and $\hat{\beta}(x)$ denote the parameter variation of the nonlinear input transformation and \hat{e} describes the deviation of the disturbed system output to the reference trajectory $\hat{e} = \hat{z} - R$.

By inserting Eq. (A.23b) and Eq. (A.23c) into Eq. (A.23a), the system can be rewritten such that the resulting system appears as a perturbation of the nominal system:

$$\begin{aligned} \dot{e} &= A_c e + B_c \left[\gamma(u - \alpha) - r^{(\delta)} \right] \\ &= A_c e + B_c \left[\gamma((\hat{\alpha} - \alpha) + \hat{\beta}(-K \hat{e} + r^{(\delta)}) - r^{(\delta)}) \right] \\ &= A_c e + B_c \left[\gamma((\hat{\alpha} - \alpha) - \hat{\beta}K \hat{e} + \hat{\beta}r^{(\delta)} + \underbrace{\hat{\beta}K e - \hat{\beta}K e}_{=0}) - r^{(\delta)} \right] + \underbrace{B_c K e - B_c K e}_{=0} \\ &= (A_c - B_c K) e + B_c \left[\gamma((\hat{\alpha} - \alpha) - \hat{\beta}K \hat{e} + \hat{\beta}r^{(\delta)} + \hat{\beta}K e - \hat{\beta}K e - \beta r^{(\delta)} + \beta K e) \right] \quad (\text{A.24}) \\ &= (A_c - B_c K) e + B_c \left[\gamma((\hat{\alpha} - \alpha) + \hat{\beta}K(e - \hat{e}) + (\hat{\beta} - \beta)r^{(\delta)} + (\beta - \hat{\beta})K e) \right] \\ &= (A_c - B_c K) e + B_c \underbrace{\left[\gamma((\hat{\alpha} - \alpha) + (\hat{\beta} - \beta)(r^{(\delta)} - K e) + \hat{\beta}K(e - \hat{e})) \right]}_{\delta(e)} \\ &= (A_c - B_c K) e + B_c \delta(e), \quad \delta(e) \in \mathbb{R}^4 \end{aligned}$$

where

$$\begin{aligned} e - \hat{e} &= (z - R) - (\hat{z} - R) \\ &= z - \hat{z} \\ &= T(x) - \hat{T}(x) \end{aligned} \quad (\text{A.25})$$

is the effect of the parameter variation on the nonlinear state transformation defined in Eq. (4.54).

The final equation in Eq. (A.24) shows that the parameter variation of Eq. (A.23b) can be represented as disturbance of the nominal system.

A.3 Proof of System Stability for Disturbed System

Consider a system of the form

$$\dot{z} = (A_c - B_c K)z + B_c \delta(z), \quad \delta(z) \in \mathbb{R}^4, \quad (\text{A.26})$$

which represents a closed loop system and appears as a perturbation of the nominal system.

Lemma [38] Consider the closed-Loop system (A.26), where $(A_c - B_c K)$ is Hurwitz. Let $P = P^T > 0$ be the solution of the Lyapunov equation

$$P(A - BK) + (A - BK)^T P = -I$$

and k be a nonnegative constant less than $1/(2\|PB\|_2)$.

- If $\|\delta(z)\| \leq k\|z\|$ for all z , the origin of (A.26) will be globally exponentially stable.
- If $\|\delta(z)\| \leq k\|z\| + \epsilon$ for all z , the state z will be globally ultimately bounded by ϵc for some $c > 0$.

Proof Transposing Eq. (A.26) yields

$$\dot{z}^T = z^T (A_c - B_c K)^T + \delta(z)^T B_c^T, \quad \delta(z) \in \mathbb{R}^4. \quad (\text{A.27})$$

To analyse the stability of the system a quadratic Lyapunov function V is considered

$$V = z^T P z, \quad P = \text{const}. \quad (\text{A.28})$$

Applying the time derivative to the Lyapunov function leads to

$$\begin{aligned} \dot{V} &= \dot{z}^T P z + z^T P \dot{z} \\ &= z^T [(A_c - B_c K)^T P z + \underbrace{\delta(z)^T B_c^T P z}_{= z^T P B_c \delta(z)}] + z^T P (A_c - B_c K) z + z^T P B_c \delta(z) \\ &= z^T \underbrace{[P(A_c - B_c K) + (A_c - B_c K)^T P]}_{=-I} z + 2 \underbrace{z^T P B_c \delta(z)}_{\in \mathbb{R}} \\ &\leq -|z|_2^2 + 2|P B_c|_2 |z|_2 |\delta(z)|_2, \end{aligned} \quad (\text{A.29})$$

where the first part is negative and, therefore, has to compensate the second term to yield an overall negative value.

If $|\delta(z)|_2 \leq k|z|_2 + \epsilon$, then

$$\begin{aligned} \dot{V} &\leq -|z|_2^2 + 2k|P B_c|_2 |z|_2^2 + 2\epsilon|P B_c|_2 |z|_2 \\ &= -|z|_2^2 + \underbrace{\Theta_1 |z|_2^2 - \Theta_1 |z|_2^2}_{=0} + 2k|P B_c|_2 |z|_2^2 + 2\epsilon|P B_c|_2 |z|_2 \\ &= -(1 - \Theta_1)|z|_2^2 - \underbrace{\Theta_1 |z|_2^2 + 2k|P B_c|_2 |z|_2^2}_{\leq 0} + 2\epsilon|P B_c|_2 |z|_2, \end{aligned} \quad (\text{A.30})$$

where $\Theta_1 \in (0, 1)$. By requiring that the second term compensates the third term, one obtains the inequality

$$k \leq \frac{\Theta_1}{2|P B_c|_2}, \quad (\text{A.31})$$

where Θ_1 is chosen such that the inequality is fulfilled. The remaining inequality

$$\dot{V} \leq -(1 - \Theta_1)|z|_2^2 + 2\epsilon|PB_c|_2|z|_2^2 \quad (\text{A.32})$$

is fulfilled for $\epsilon = 0$ and the origin is globally exponentially stable. If $\epsilon > 0$,

$$\begin{aligned} \dot{V} &\leq -(1 - \Theta_1)|z|_2^2 + 2\epsilon|PB_c|_2|z|_2^2 \\ &= -(1 - \Theta_1)|z|_2^2 - (1 - \Theta_1) \underbrace{(\Theta_2|z|_2^2 - \Theta_2|z|_2^2)}_{=0} + 2\epsilon|PB_c|_2|z|_2 \\ &= -(1 - \Theta_1)(1 - \Theta_2)|z|_2^2 - \underbrace{(1 - \Theta_1)\Theta_2|z|_2^2 + 2\epsilon|PB_c|_2|z|_2}_{\leq 0} \end{aligned} \quad (\text{A.33})$$

with $\Theta_2 \in (0, 1)$ and requiring that the second term compensates the third term, one obtains the inequality

$$|z| \geq \frac{2\epsilon|PB_c|_2}{(1 - \Theta_1)\Theta_2} = \epsilon c_0. \quad (\text{A.34})$$

The resulting equation

$$\dot{V} \leq -(1 - \Theta_1)(1 - \Theta_2)|z|_2^2 \leq 0, \quad |z| \geq \frac{2\epsilon|PB_c|_2}{(1 - \Theta_1)\Theta_2} = \epsilon c_0 \quad (\text{A.35})$$

is globally ultimately bounded. For large values of z , the derivative of the Lyapunov function \dot{V} is negative, but in the neighborhood of the origin Eq. (A.35) is not satisfied.

Appendix B

Thermodynamics

B.1 Supercritical Water Injection

The idea of supercritical water injection is based on the research in the field of Rapid Expansion of a Supercritical Solution (RESS) [62, 63]. This technique is used to generate small particle distributions from certain solutions. This is e.g. applied in the pharmaceutical industry to maximise the surface area of pharmaceutical drugs.

The concept of supercritical water injection is depicted in Fig. B.1. The figure shows the TS-Diagram of water with isobaric and isenthalpic processes depicted in red and blue, respectively. The critical point of water T_K is depicted at the top of the two-phase region. The critical point is located at 221 bar and 374 °C [45]. For the injection of the supercritical water

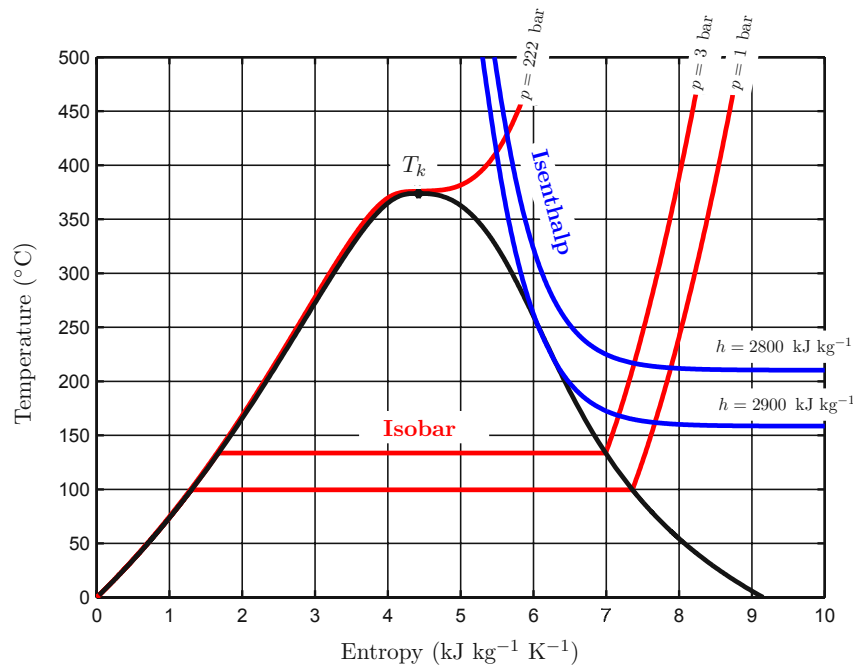


Figure B.1: Schematic concept of supercritical water injection.

into a process gas, the water has to be compressed above the critical pressure and heated along an isobaric line above the critical point as depicted in the figure. In the figure, the

222 bar isobaric is highlighted, but this only poses as the lower limit. Above the critical point water is in the state of a supercritical fluid. From this state, it can be injected into a low pressure chamber (e.g. through a nozzle or orifice). This corresponds to an isenthalpic process to a low pressure region. In the figure, two possible isenthalpic processes are depicted as reference. The supercritical water would directly enter the gas phase without crossing the two-phase region.

Compared to the liquid water injection, as described in Section 2.1.3, this has the advantage that the enthalpy of vapourisation does not have to be provided by the process gas, but can be supplied with the injection process. Additionally, the supercritical water injection does not cross the two-phase region and therefore, the risk of inserting unwanted water droplets into the process is minimised.

B.2 Full Derivation of Temperature Dynamics

Consider the system depicted in Fig. B.2, where two gas streams (Gas and Steam) are entering the system, mixing in the chamber and leaving as gas mixture at the outlet. The temperature dynamics $\frac{d}{dt}T$ of the system derives as follows:

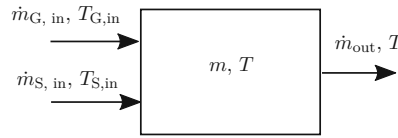


Figure B.2: System under consideration.

The mass balance equations for the system are given by

$$\frac{d}{dt}m_G = \dot{m}_{G, in} - \dot{m}_{G, out}, \quad (\text{B.1})$$

$$\frac{d}{dt}m_S = \dot{m}_{S, in} - \dot{m}_{S, out}, \quad (\text{B.2})$$

where the first terms represent the inflowing gas streams, and the second terms represent the outflowing mass streams. The outflowing gas streams in Eq. (B.1) and Eq. (B.2) are given by the mass fraction of the total outflowing mass stream

$$\dot{m}_{G, out} = \frac{m_G}{m} \dot{m}_{out}, \quad (\text{B.3})$$

$$\dot{m}_{S, out} = \frac{m_S}{m} \dot{m}_{out}, \quad (\text{B.4})$$

with the total mass in the system given by

$$m = m_G + m_S, \quad (\text{B.5})$$

where m_G represents the gas mass and m_S the steam mass in the system. The energy balance equation for the system is given by

$$\frac{dU}{dt} = \dot{m}_{G, in} h_{G, in} + \dot{m}_{S, in} h_{S, in} - \dot{m}_{out} h_{out}, \quad (\text{B.6})$$

$$\frac{dU}{dt} = \frac{d}{dt}(m_G u_G + m_S u_S), \quad (\text{B.7})$$

where U is the internal energy of the system, $h_{G,\text{in}}$ is the specific enthalpy of the inflowing gas, $h_{S,\text{in}}$ is the specific enthalpy of the inflowing steam, h_{out} is the specific enthalpy of the outflowing gas mixture and u_G and u_S represent the specific internal energy of the gas and steam, respectively.

By inserting Eq. (B.3) and Eq. (B.4) into the outflowing enthalpy stream, given by Eq. (B.6), one obtains

$$\dot{m}_{\text{out}} h_{\text{out}} = \frac{1}{m} \dot{m}_{\text{out}} (m_G h_{G,\text{out}} + m_S h_{S,\text{out}}). \quad (\text{B.8})$$

The enthalpy of the gas (dry air) is given by

$$h_{G,\text{in}} = c_{p,G} T_{G,\text{in}}, \quad (\text{B.9})$$

$$h_{G,\text{out}} = c_{p,G} T, \quad (\text{B.10})$$

where $c_{p,G}$ and $c_{p,S}$ are the specific heat capacities at constant pressure. The enthalpy of the steam is given by

$$h_{S,\text{in}} = c_{p,S} T_{S,\text{in}} + r_0, \quad (\text{B.11})$$

$$h_{S,\text{out}} = c_{p,S} T + r_0, \quad (\text{B.12})$$

where $c_{v,G}$ and $c_{v,S}$ are the specific heat capacities at constant volume and r_0 represents the latent heat of steam.

Combining Eq. (B.10) and Eq. (B.12) with the relation of the gas constant R and the specific heat capacities, the relation of specific enthalpy and specific internal energy and the ideal gas law

$$R = c_p - c_v, \quad (\text{B.13})$$

$$h = u + pv, \quad v = \frac{V}{m}, \quad (\text{B.14})$$

$$RT = pv, \quad (\text{B.15})$$

the specific internal energy of gas in the system can be written as

$$\begin{aligned} u_G &= h_G - pv_G \\ &= c_{p,G} T - pv_G \\ &= (R + c_{v,G}) T - pv_G \\ &= \underbrace{RT - pv_G}_{=0} + c_{v,G} T. \end{aligned} \quad (\text{B.16})$$

Further, the specific internal energy of steam in the system can be written as

$$\begin{aligned} u_S &= h_S - pv_S \\ &= c_{p,S} T + r_0 - pv_S \\ &= (R + c_{v,S}) T + r_0 - pv_S \\ &= \underbrace{RT - pv_S}_{=0} + c_{v,S} T + r_0. \end{aligned} \quad (\text{B.17})$$

By inserting these into Eq. (B.7) and assuming constant specific heat capacities c_p and c_v , one obtains

$$\begin{aligned} \frac{d}{dt} (m_G u_G + m_S u_S) &= \left(\frac{d}{dt} m_G \right) c_{v,G} T + \left(\frac{d}{dt} m_S \right) (c_{v,S} T + r_0) \\ &\quad + \left(\frac{d}{dt} T \right) (m_G c_{v,G} + m_S c_{v,S}). \end{aligned} \quad (\text{B.18})$$

Combining this equation with Eq. (B.6), one obtains the final form

$$\begin{aligned} \frac{d}{dt}T = & \frac{1}{m_G c_{v,G} + m_S c_{v,S}} \\ & \cdot \left(\dot{m}_{G, \text{in}} c_{p,G} T_{G, \text{in}} + \dot{m}_{S, \text{in}} (c_{p,S} T_{S, \text{in}} + r_0) \right. \\ & - \frac{1}{m} \dot{m}_{\text{out}} \left(m_G c_{p,G} T + m_S (c_{p,S} T + r_0) \right) \\ & \left. - \frac{d}{dt} m_G c_{v,G} T - \frac{d}{dt} m_S (c_{v,S} T + r_0) \right), \end{aligned} \quad (\text{B.19})$$

which is used to express the temperature dynamics of the system.

B.3 Derivation of Nonlinear Flow Equation

From the first law of thermodynamics for stationary and adiabatic flow one can state

$$h_1 + \frac{v_1^2}{2} = h_2 + \frac{v_2^2}{2}, \quad (\text{B.20})$$

where $h_{1,2}$ are the enthalpies and the $v_{1,2}$ velocities of the fluid. Further, for frictionless and ideal gases the ideal gas law is given by

$$pv = RT, \quad v = \frac{1}{\rho} = \frac{V}{m}, \quad (\text{B.21})$$

where p denotes the pressure, v the volume per mass, R the gas constant and T the temperature. The relation of the gas constant and the specific heat capacities is given by

$$R = c_p - c_v. \quad (\text{B.22})$$

The enthalpy is defined as

$$dh = c_p dT \quad (\text{B.23})$$

and the isentropic process is given by

$$\frac{T_2}{T_1} = \left(\frac{p_2}{p_1} \right)^{\frac{\kappa-1}{\kappa}} = \left(\frac{v_1}{v_2} \right)^{\kappa-1} = \left(\frac{\rho_2}{\rho_1} \right)^{\kappa-1}, \quad \kappa = \frac{c_p}{c_v}. \quad (\text{B.24})$$

Assuming the start velocity to be zero ($v_1 = 0$) and applying the above introduced equations, Eq. (B.20) can be written as

$$\begin{aligned} \frac{v_2^2}{2} &= h_1 - h_2 \\ &= c_{p,1} T_1 - c_{p,2} T_2 \\ &= c_{p,1} T_1 - c_{p,2} T_1 \left(\frac{p_2}{p_1} \right)^{\frac{\kappa-1}{\kappa}} \\ &= c_p T_1 \left(1 - \left(\frac{p_2}{p_1} \right)^{\frac{\kappa-1}{\kappa}} \right). \end{aligned} \quad (\text{B.25})$$

By assuming

$$c_{p,1} = c_{p,2} = c_p \quad (\text{B.26})$$

and expressing the product of the specific heat capacity and the temperature as

$$c_p T = c_p \frac{pv}{R} = c_p \frac{pv}{c_p - c_v} = \frac{\kappa}{\kappa - 1} pv \quad (\text{B.27})$$

the velocity can further be expressed as

$$v_2 = \sqrt{2 \frac{\kappa}{\kappa - 1} p_1 v_1 \left[1 - \left(\frac{p_2}{p_1} \right)^{\frac{\kappa-1}{\kappa}} \right]}. \quad (\text{B.28})$$

With Eq. (B.28) and Eq. (B.24)

$$p_1 v_1^\kappa = p_2 v_2^\kappa \quad \Leftrightarrow \quad p_1 \left(\frac{1}{\rho_1} \right)^\kappa = p_2 \left(\frac{1}{\rho_2} \right)^\kappa \quad (\text{B.29})$$

the mass flow through an opening area A can be expressed as

$$\begin{aligned} \dot{m} &= v_2 \rho_2 A \\ &= A \rho_1 \left(\frac{p_2}{p_1} \right)^{\frac{1}{\kappa}} \sqrt{2 \frac{\kappa}{\kappa - 1} p_1 \frac{1}{\rho_1} \left[1 - \left(\frac{p_2}{p_1} \right)^{\frac{\kappa-1}{\kappa}} \right]} \\ &= A \sqrt{2 p_1 \rho_1} \underbrace{\sqrt{\frac{\kappa}{\kappa - 1} \left[\Pi^{\frac{2}{\kappa}} - \Pi^{\frac{\kappa+1}{\kappa}} \right]}}_{\Psi}, \quad \Pi = \frac{p_2}{p_1} \\ &= A p_1 \sqrt{\frac{2}{RT_1}} \psi. \end{aligned} \quad (\text{B.30})$$

with the critical pressure given by

$$\Pi_{\text{crit.}} = \left(\frac{2}{\kappa + 1} \right)^{\frac{\kappa}{\kappa-1}}. \quad (\text{B.31})$$

The properties of this function are discussed in Section 2.1.1 and the dependency of the mass flow of upstream and downstream pressure are highlighted in Fig. 2.3. To derive the critical pressure ratio, the maximum of the function Ψ is derived analytically.

Ψ has a maximum for

$$\frac{\partial \Psi}{\partial \Pi} = 0. \quad (\text{B.32})$$

Setting the derivation of Ψ with respect to Π to zero yields

$$\frac{\partial}{\partial \Pi} \left[\Pi^{\frac{2}{\kappa}} - \Pi^{\frac{\kappa+1}{\kappa}} \right] = \frac{2}{\kappa} \Pi^{\frac{2-\kappa}{\kappa}} - \frac{\kappa+1}{\kappa} \Pi^{\frac{1}{\kappa}} = 0, \quad (\text{B.33})$$

which can be rewritten as

$$\begin{aligned} 2 \Pi^{\frac{2-\kappa}{\kappa}} &= (\kappa + 1) \Pi^{\frac{1}{\kappa}} \\ \left(\frac{2}{\kappa + 1} \right)^\kappa \Pi^{(2-\kappa)} &= \Pi \\ \left(\frac{2}{\kappa + 1} \right)^\kappa &= \Pi^{\kappa-1} \quad \rightarrow \quad \Pi_{\text{crit.}} = \left(\frac{2}{\kappa + 1} \right)^{\frac{\kappa}{\kappa-1}}. \end{aligned} \quad (\text{B.34})$$

Inserting $\Pi_{\text{crit.}}$ into Ψ , as defined in Eq. (B.30), it immediately follows that

$$\psi_{\text{max}} = \left(\frac{2}{\kappa + 1} \right)^{\frac{1}{\kappa-1}} \sqrt{\frac{\kappa}{\kappa + 1}}. \quad (\text{B.35})$$

The derivation of the nonlinear flow equation Eq. (B.30) has been done under the assumptions of laminar and frictionless flow. In real applications, this is not given and turbulences occur on edges and such. These cause additional pressure resistance, which affects the resulting mass flow. Therefore, literature suggests a correctional factor α , which accounts for these effects. It is generally referred to as discharge coefficient. The modified equation is given by

$$\dot{m} = \alpha A p_1 \sqrt{\frac{2}{RT_1}} \psi. \quad (\text{B.36})$$

As described in Section 3.3, the nonlinear flow equation is parameterised with measurements from the test bed and therefore, the factor α is included in the determined opening area. This can be expressed by

$$\dot{m} = \alpha A p_1 \sqrt{\frac{2}{RT_1}} \psi = \hat{A} p_1 \sqrt{\frac{2}{RT_1}} \psi, \quad (\text{B.37})$$

where \hat{A} is the opening area determined from measurements. This notation is applied throughout this thesis.

Appendix C

Control Parameters Applied for Measurements

The used parameter configuration of the four 2 DoF controllers is given in Table C.1.

Channel	K_P	K_I	K_D
T	2	0.001	15
p	6	3	0
φ	5	1	5
\dot{m}_{out}	1	0.1	0

Table C.1: Control parameters for measurement nonlinear control concept.

The used parameter configuration of the four linear controllers is given in Table C.2.

Channel	K_P	K_I	K_D
$\dot{m}_{G, u}$	40	1	0
T_u	20	3	0
$\dot{m}_{S, u}$	0.5	0.1	0.2
A_u	0.5	0.1	0.1

Table C.2: Control parameters for linear control structure.

The used parameter configuration of the four linear controllers with extended model-based feedforward control is given in Table C.3.

Channel	K_P	K_I	K_D
$\dot{m}_{G, u}$	100	1	0
T_u	10	3	0
$\dot{m}_{S, u}$	0.5	0.3	0.5
A_u	0.5	0.1	0.1

Table C.3: Control parameters for linear control structure with additional model-based feedforward control.

Appendix D

Fuel Cell System Definitions

In the following a variety of definitions of fuel cell systems are provided, which are used by different organisations.

- Fig. D.1 shows a fuel cell system schematic from the International Electrotechnical Commission (IEC) [64]. An update can be found in [65].
- Fig. D.2 shows a fuel cell system schematic from the Argonne National Laboratory (ANL) [66].
- Fig. D.3 shows a dual stack fuel cell system schematic from the US-Department of Energy [67].
- Fig. D.4 shows a the fuel cell system definition according to the Society of Automotive Engineers (SAE) [68]. The abbreviations are as follows: Fuel Supply System (FSS), Fuel Processing Subsystem (FPS), Air Processing Subsystem (APS), Thermal Management Subsystem (TMS), Water Treatment Subsystem (WTS), Fuel Cell Stack Power Subsystem (FCSS), Power Distribution Subsystem (PDS), Fuel Cell Control System (FCCS), Vehicle Control System (VCS) and Power Conditioning System (PCS).

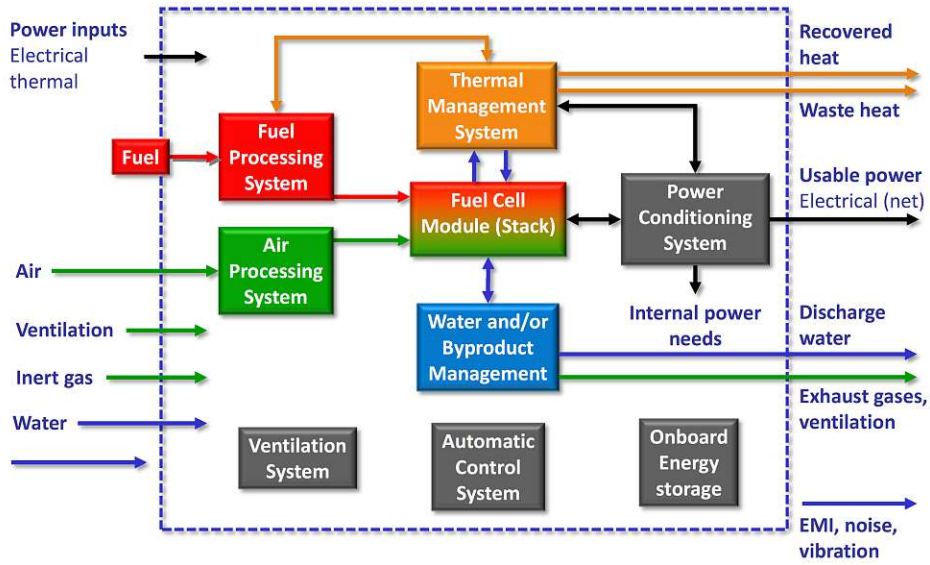


Figure D.1: Schematic of fuel cell system according to IEC.

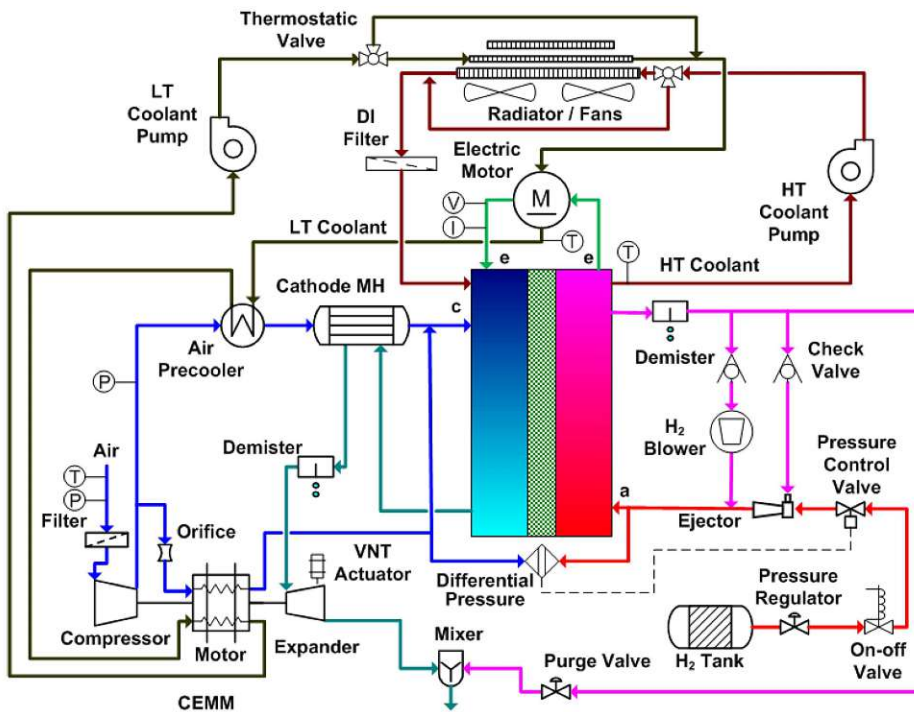


Figure D.2: Schematic of fuel cell system according to ANL.

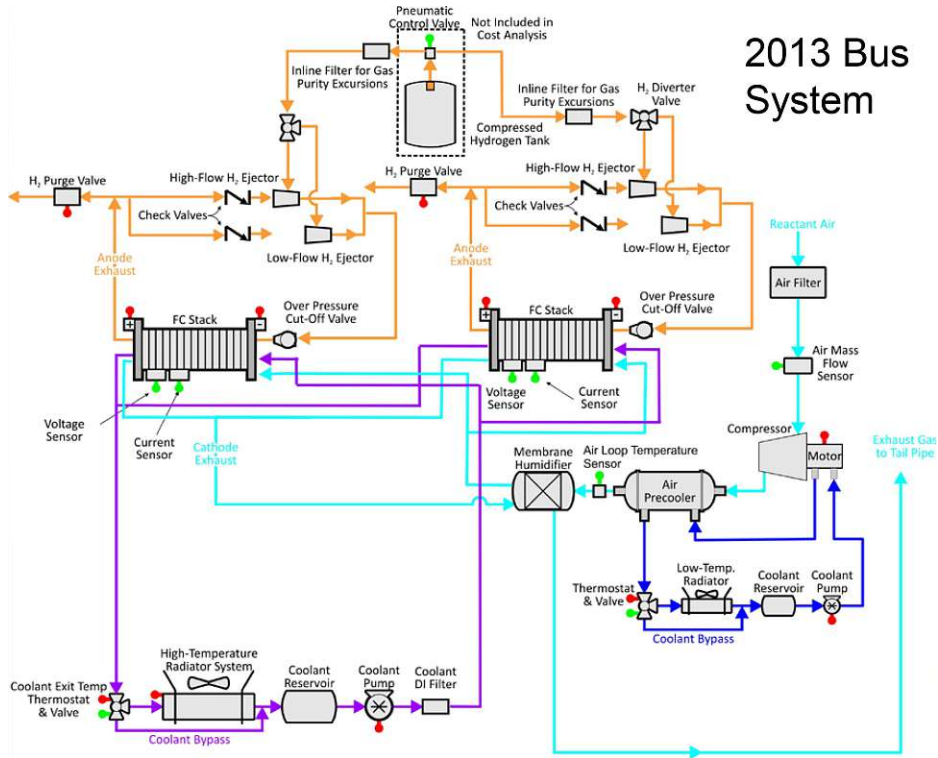


Figure D.3: Schematic of fuel cell system according to US-Department of Energy.

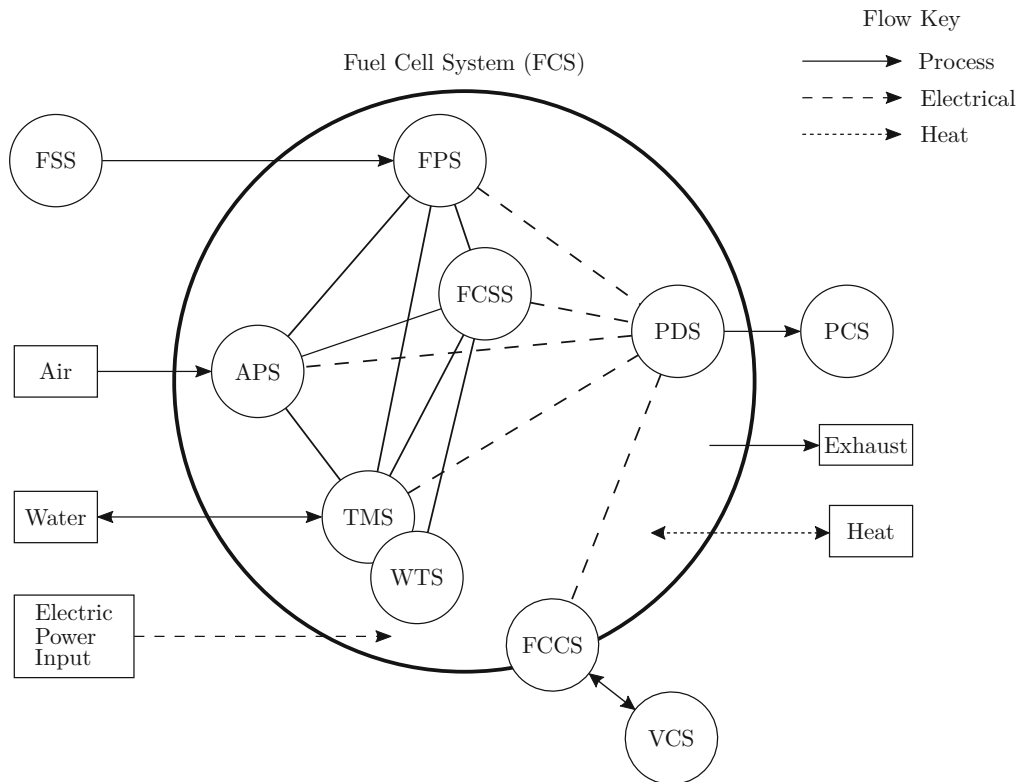


Figure D.4: Schematic of fuel cell system according to SAE J2617.

List of Figures

1.1	Explosive view of a membrane electrode assembly [14].	2
1.2	Schematic of fuel cell and working principle.	3
1.3	Schematic of a fuel cell system.	4
1.4	Schematic of a fuel cell test bed.	7
2.1	Schematic of functional blocks.	10
2.2	Flow control concepts.	10
2.3	The plots show the nonlinear flow equation as a function of the pressure ratio of the upstream pressure (p_{in}) and the downstream pressure (p_{out}). Plot (a) shows the mass flow for varying the upstream pressure and keeping the downstream pressure constant. Plot (b) shows the mass flow for varying the downstream pressure and keeping the upstream pressure constant.	11
2.4	Thermal management concepts.	12
2.5	Plot (a) shows the step response of the heater. The upper subplot shows the gas temperature at the heater outlet, whereas the lower subplot shows the applied power of the heater. Plot (b) shows the step response of the concept C_H	13
2.6	Plot (a) shows the characteristic of concept B_H obtained from stationary measurements. Plot (b) shows the characteristic of concept C_H obtained from stationary measurements.	14
2.7	Plot (a) shows the valve positions for Bypass opening. Plot (b) shows adapted valve positions to account for the flat part in the Bypass characteristic. . . .	14
2.8	The plots show the TS-Diagram for Water. Plot (a) shows the evaporation process for liquid water injection. Plot (b) shows that for direct steam injection the evaporation enthalpy is already accounted for.	15
2.9	Humidification by steam boiler.	16
2.10	Back pressure control concepts.	17
2.11	Piping and instrumentation diagram of cathode gas conditioning system. . . .	18
2.12	The figures show the applied hardware components for the realised hardware setup. In Fig. (a), the concept A_F with the pressure controller (PC), orifice plate (OP) and the sensors are shown. In Fig. (b), the gas heating elements are shown. In Fig. (c), the steam valve, backpressure valve and applied measuring section are shown. In Fig. (d), the overall hardware setup is shown and in Fig. (e), the real-time capable MicroAutoBox II with a programmable logic controller is shown, which has been used to implement the designed control algorithms.	19

2.13	The measured step response of the system shows coupling of the system outputs. Plot (a) shows the sensor signals of the input variables, and plot (b) shows the measured step response of the system outputs. The variation of one input has an effect on all four outputs.	20
3.1	Schematic block diagram of dynamic gas conditioning system model.	22
3.2	The figure illustrates the nonlinearity of the relative humidity φ given by Eq. (3.16). The variables gas mass m_G and pressure p are fixed and the function is evaluated by iterating through the steam mass m_S and the temperature T	27
3.3	Step response of the system model. Plot (a) shows the input variables u of the system, and plot (b) shows the system outputs y	28
3.4	The figures show the coupled nonlinear input-to-output behaviour of the system. For the plots, a set point change was performed, where the two input variables T_u and A_u were kept constant and the other two input variables \dot{m}_G and \dot{m}_S were varied. The different grey surface areas illustrate the time evolution of the system with the final steady state as coloured surface.	29
3.5	Lyapunov function surface levels.	30
3.6	The figures show the state trajectories for set point changes of the nonlinear system. The colour of the trajectories indicate the value of the Lyapunov function at the given point. The boundaries of the system are indicated by the grey surface areas. Fig. (a) and (b) show a set of set point changes to a low set point. Fig. (c) and (d) show a set of set point changes to a high set point. Fig. (e) and (f) show a double set point change.	33
3.7	Parametrisation of nonlinear flow equation with measurements of the aperture. Plot shows measured data points and the (best) fit result.	35
3.8	Plot (a) shows the steam valve characteristic obtained from stationary measurements. Plot (b) shows the back pressure valve characteristic obtained from stationary measurements. Measurements in (b) could only be obtained up to 60 % valve opening. The valve characteristic above this point was linearly extrapolated.	36
3.9	Characteristic of the <i>Heater</i> (concept C_H , Fig. 2.4c) obtained from stationary measurements. Data points taken for opening and for closing of the bypass.	37
3.10	Comparison of parametrised model with measurement data. The red line shows the measured system output. The blue line shows the corresponding system model output. For the temperature, a dashed blue line indicates a $\pm 3^\circ\text{C}$ temperature band for the model output.	38
3.11	Step response of the system model with different system parameters. Plot (a) shows the output trajectories y for the variation of the system volume, and plot (b) shows the output trajectories y for the variation of the steam temperature.	39
4.1	The figure depicts the linear and decoupled MIMO system. Σ represents the nonlinear system given by Eq. (4.19). Σ^{-1} represents the nonlinear input transformation, which transforms the whole system into a linear and decouple system.	47
4.2	The Lie-Bäcklund transformation transforms the system from the state space coordinates into flat coordinates. To visualise this, the potential Φ_{DGL} of the conservative differential equation $\dot{x} = f(x, u)$ with $\nabla\Phi_{\text{DGL}} = f(x, 0)$ and the potential Φ_{F} of the trivial system in flat coordinates with $\nabla\Phi_{\text{F}} = 0$ is plotted on the z -axis [39].	48
4.3	Illustration of a Two-Degree-of-Freedom (2 DoF) control structure for a SISO system.	49

4.4	Schematic view of the transformation of the coupled system (a) into the decoupled system (b). The decoupled system is represented as chain of integrators with the new input variable ν . The length of the chain of integrators is equal to the <i>relative degree</i> δ_j of the output y_j	52
4.5	Block diagram of the Two-Degree-of-Freedom (2DoF) controller. To each decoupled linear system, a PID controller is applied.	54
4.6	The plot shows a series of step changes of the closed loop system. Plot (a) shows the control input u . Plot (b) shows the system output y , with the reference trajectory in dashed blue and the achieved system output in red. . .	56
4.7	The figure shows different closed loop trajectories of the system. Fig. (a) and (b) show a comparison of an open loop set point change (from Fig. 3.6e) with three different closed loop trajectories (blue full lines). In contrast to the open loop system, the closed loop trajectories stay within the operation range. Fig. (c) and (d) show a more complex system trajectory, which demonstrates the closed loop system performance.	57
4.8	Schematic of the set Λ , Ω_ϵ and Ω_c	59
4.9	Non-Decoupled closed loop system. System parameters Θ_0 differ from parameters Θ_1 , which are used to determine the nonlinear input transformation. . .	60
4.10	Calculated trajectory $\ \delta(e)\ - k\ e\ $ in accordance to Lemma 4.1. For the trajectory, an ϵ can be found, which fulfils the Lemma.	61
4.11	The figures show the effect of parameter variations of the system volume and steam temperature on the decoupled system. In plot (a) and (b) only feedforward control is applied. In plot (c) and (d) the designed 2DoF controller is applied.	63
5.1	Schematic of control setup on test bed.	64
5.2	Fig. (a) shows the nonlinear system model, which has been used to design the nonlinear multivariate control concept. Fig. (b) shows the nonlinear system with the control inputs u_{TB} and the mapping of these inputs to the <i>virtual</i> inputs u_{1-4} used for modelling.	65
5.3	Schematic view of the hardware components of the flow concept (a) and the block diagram of the corresponding <i>low level</i> control concept (b).	66
5.4	Schematic view of the hardware components of the heating concept (a) and the block diagram of the corresponding <i>low level</i> control concept (b).	67
5.5	Schematic view of the hardware components of the steam concept (a) and the block diagram of the corresponding <i>low level</i> control concept (b).	68
5.6	Schematic view of the hardware components of the backpressure concept (a) and the block diagram of the corresponding <i>low level</i> control concept (b). . .	68
5.7	Block diagram of the Two-Degree-of-Freedom (2DoF) controller. To each decoupled linear system, a PID controller is applied. The control variables of the nonlinear decoupling block are mapped to the actual actuator inputs of the test bed.	71
5.8	Control performance of nonlinear control concept applied on the nonlinear and coupled test bed. Plot (a) shows the sensor signals of the control variables. Plot (b) shows the output of the nonlinear system in red and the reference trajectories in blue.	71
5.9	The figures show the closed loop system following a reference trajectory in state space. Measurements are given in red and the reference trajectory in blue. Plot (a) is a 3D representation where the system constraints are indicated as grey surface areas. Plot (b) is a 2D projection of (a). Plot (c) is a zoomed 3D view. . .	73

5.10	Linear control structure for control of nonlinear and coupled test bed.	74
5.11	Control performance of linear controllers applied on the nonlinear and coupled test bed. Plot (a) shows the sensor signals of the control variables. Plot (b) shows the output of the nonlinear system in red and the reference trajectories in blue.	74
5.12	State evolution of closed loop system with linear control structure. The reference trajectory is shown in blue, measurements are shown in red.	75
5.13	Linear control structure with additional model-based feedforward control for control of nonlinear and coupled test bed.	76
5.14	Control performance of linear controllers with additional model-based feedforward control applied on the nonlinear and coupled test bed. Plot (a) shows the sensor signals of the control variables. Plot (b) shows the output of the nonlinear system in red and the reference trajectories in blue.	76
5.15	State evolution of closed loop system with linear control structure and additional model-based feedforward control. The reference trajectory is shown in blue, measurements are shown in red.	77
B.1	Schematic concept of supercritical water injection.	85
B.2	System under consideration.	86
D.1	Schematic of fuel cell system according to IEC.	93
D.2	Schematic of fuel cell system according to ANL.	93
D.3	Schematic of fuel cell system according to US-Department of Energy.	94
D.4	Schematic of fuel cell system according to SAE J2617.	94

List of Tables

2.1	System operating range.	17
2.2	Operating ranges and quantities that the different concepts should provide.	17
3.1	Lyapunov function parameters.	31
3.2	Model parameters estimated from measurements.	34
3.3	Deviation factors of model parameters used for step response simulations of parameter varied system.	38
4.1	Mean squared error for different magnitudes of measurement noise. The magnitude is given as standard deviation of the normal distribution.	62
5.1	Hardware components implemented in the test bed.	70
5.2	Standard deviations for stationary and dynamic measurements of nonlinear control concept.	72
5.3	Standard deviations for stationary and dynamic measurements of linear control structure.	75
5.4	Standard deviations for stationary and dynamic measurements of linear control concept with additional model-based feedforward control.	75
C.1	Control parameters for measurement nonlinear control concept.	91
C.2	Control parameters for linear control structure.	91
C.3	Control parameters for linear control structure with additional model-based feedforward control.	91

Bibliography

- [1] European Parliament, “Regulation (EU) No 333/2014 of the European Parliament and of the Council of 11 March 2014 amending Regulation (EC) No 443/2009 to define the modalities for reaching the 2020 target to reduce CO₂ emissions from new passenger cars,” *Official Journal of the European Union*, 2014. (Downloaded 18/11/2015).
- [2] U.S. Department of Energy, “2015 Annual Progress Report,” Tech. Rep. DOE/GO-102015-4731, DOE Hydrogen and Fuel Cells Program, 2015.
- [3] N. Yamaguchi, A. Iwai, T. Fukushima, and H. Shinoki, “New Drive Motor for Fuel Cell Vehicle FCX Clarity,” Apr. 2009.
- [4] W. Sung, Y.-I. Song, K.-H. Yu, and T.-W. Lim, “Recent Advances in the Development of Hyundai & Kia’s Fuel Cell Electric Vehicles,” *SAE Int. J. Engines*, vol. 3, pp. 768–772, 04 2010. <http://dx.doi.org/10.4271/2010-01-1089>.
- [5] T. Moriya, “Honda Fuel Cell Electric Vehicle Development,” *SAE Technical Paper 2011-39-7240*, p. 2011.
- [6] T. Yoshida and K. Kojima, “Toyota MIRAI Fuel Cell Vehicle and Progress Toward a Future Hydrogen Society,” *The Electrochemical Society Interface*, vol. 24, no. 2, pp. 45–49, 2015. <http://dx.doi.org/10.1149/2.F03152if>.
- [7] O. Z. Sharaf and M. F. Orhan, “An overview of fuel cell technology: Fundamentals and applications,” *Renewable and Sustainable Energy Reviews*, vol. 32, pp. 810 – 853, 2014. <https://doi.org/10.1016/j.rser.2014.01.012>.
- [8] S. Mekhilef, R. Saidur, and A. Safari, “Comparative study of different fuel cell technologies,” *Renewable and Sustainable Energy Reviews*, vol. 16, no. 1, pp. 981 – 989, 2012. <https://doi.org/10.1016/j.rser.2011.09.020>.
- [9] F. Barbir, *PEM Fuel Cells - Theory and Practice*. Academic Press, 2012.
- [10] X. Yuan, C. Song, H. Wang, and J. Zhang, *Electrochemical Impedance Spectroscopy in PEM Fuel Cells: Fundamentals and Applications*. Springer London, 2009.
- [11] V. Mehta and J. S. Cooper, “Review and analysis of PEM fuel cell design and manufacturing,” *Journal of Power Sources*, vol. 114, no. 1, pp. 32 – 53, 2003. [https://doi.org/10.1016/S0378-7753\(02\)00542-6](https://doi.org/10.1016/S0378-7753(02)00542-6).
- [12] G. Hoogers, *Fuel cell technology handbook*. CRC Press LLC, 2003.
- [13] K. Kuang and K. Easler, *Fuel Cell Electronics Packaging*. Springer, 2007.

- [14] B. G. Pollet, I. Staffell, and J. L. Shang, “Current status of hybrid, battery and fuel cell electric vehicles: From electrochemistry to market prospects,” *Electrochimica Acta*, vol. 84, pp. 235 – 249, 2012. <http://dx.doi.org/10.1016/j.electacta.2012.03.172>.
- [15] S. Litster and G. McLean, “PEM fuel cell electrodes,” *Journal of Power Sources*, vol. 130, no. 1, pp. 61 – 76, 2004. <https://doi.org/10.1016/j.jpowsour.2003.12.055>.
- [16] I.-S. Han, J. Jeong, and H. K. Shin, “PEM fuel-cell stack design for improved fuel utilization,” *International Journal of Hydrogen Energy*, vol. 38, no. 27, pp. 11996 – 12006, 2013. <https://doi.org/10.1016/j.ijhydene.2013.06.136>.
- [17] H. Liu, P. Li, D. Juarez-Robles, K. Wang, and A. Hernandez-Guerrero, “Experimental study and comparison of various designs of gas flow fields to PEM fuel cells and cell stack performance,” *Frontiers in Energy Research*, vol. 2, p. 2, 2014. <https://doi.org/10.3389/fenrg.2014.00002>.
- [18] H. Nishikawa, H. Sasou, R. Kurihara, S. Nakamura, A. Kano, K. Tanaka, T. Aoki, and Y. Ogami, “High fuel utilization operation of pure hydrogen fuel cells,” *International Journal of Hydrogen Energy*, vol. 33, no. 21, pp. 6262 – 6269, 2008. <https://doi.org/10.1016/j.ijhydene.2008.07.019>.
- [19] V. Das, S. Padmanaban, K. Venkitesamy, R. Selvamuthukumar, F. Blaabjerg, and P. Siano, “Recent advances and challenges of fuel cell based power system architectures and control - A review,” *Renewable and Sustainable Energy Reviews*, vol. 73, no. Supplement C, pp. 10 – 18, 2017. <https://doi.org/10.1016/j.rser.2017.01.148>.
- [20] W. Daud, R. Rosli, E. Majlan, S. Hamid, R. Mohamed, and T. Husaini, “PEM fuel cell system control: A review,” *Renewable Energy*, vol. 113, no. Supplement C, pp. 620 – 638, 2017. <https://doi.org/10.1016/j.renene.2017.06.027>.
- [21] A. Kirubakaran, S. Jain, and R. Nema, “A review on fuel cell technologies and power electronic interface,” *Renewable and Sustainable Energy Reviews*, vol. 13, no. 9, pp. 2430 – 2440, 2009. <https://doi.org/10.1016/j.rser.2009.04.004>.
- [22] N. Sulaiman, M. Hannan, A. Mohamed, E. Majlan, and W. W. Daud, “A review on energy management system for fuel cell hybrid electric vehicle: Issues and challenges,” *Renewable and Sustainable Energy Reviews*, vol. 52, no. Supplement C, pp. 802 – 814, 2015. <https://doi.org/10.1016/j.rser.2015.07.132>.
- [23] M. Hatti, A. Meharrar, and M. Tioursi, “Power management strategy in the alternative energy photovoltaic/PEM fuel cell hybrid system,” *Renewable and Sustainable Energy Reviews*, vol. 15, no. 9, pp. 5104 – 5110, 2011. <https://doi.org/10.1016/j.rser.2011.07.046>.
- [24] J. Kancsár, M. Kozek, and S. Jakubek, “Flatness-based feedforward control of polymer electrolyte membrane fuel cell gas conditioning system,” *International Journal of Hydrogen Energy*, vol. 41, no. 39, pp. 17526 – 17538, 2016. <http://dx.doi.org/10.1016/j.ijhydene.2016.06.086>.
- [25] J. Kancsár, M. Striednig, D. Aldrian, A. Trattner, M. Klell, C. Kügele, and S. Jakubek, “A novel approach for dynamic gas conditioning for PEMFC stack testing,” *International Journal of Hydrogen Energy*, vol. 42, no. 48, pp. 28898–28909, 2017. <https://doi.org/10.1016/j.ijhydene.2017.09.076>.

- [26] J. Zhang, H. Zhang, J. Wu, and Z. JiuJun, *PEM Fuel Cell Testing and Diagnosis*. Amsterdam: Elsevier, 2013. <http://dx.doi.org/10.1016/B978-0-444-53688-4.00008-5>.
- [27] T. W. Patterson and R. M. Darling, “Damage to the cathode catalyst of a PEM fuel cell caused by localized fuel starvation,” *Electrochemical and Solid-State Letters*, vol. 9, no. 4, pp. A183–A185, 2006.
- [28] P. Ferreira-Aparicio, A. M. Chaparro, B. Gallardo, M. Folgado, and L. Daza, “Anode degradation effects in PEMFC stacks by localized fuel starvation,” *ECS Transactions*, vol. 26, no. 1, pp. 257–265, 2010.
- [29] F. Jia, L. Guo, and H. Liu, “Mitigation strategies for hydrogen starvation under dynamic loading in proton exchange membrane fuel cells,” *Energy Conversion and Management*, vol. 139, pp. 175 – 181, 2017. <https://doi.org/10.1016/j.enconman.2017.02.051>.
- [30] A. Taniguchi, T. Akita, K. Yasuda, and Y. Miyazaki, “Analysis of electrocatalyst degradation in PEMFC caused by cell reversal during fuel starvation,” *Journal of Power Sources*, vol. 130, no. 1, pp. 42 – 49, 2004. <https://doi.org/10.1016/j.jpowsour.2003.12.035>.
- [31] A. Taniguchi, T. Akita, K. Yasuda, and Y. Miyazaki, “Analysis of degradation in PEMFC caused by cell reversal during air starvation,” *International Journal of Hydrogen Energy*, vol. 33, no. 9, pp. 2323 – 2329, 2008. <https://doi.org/10.1016/j.ijhydene.2008.02.049>.
- [32] P. Rodatz, F. Büchi, C. Onder, and L. Guzzella, “Operational aspects of a large PEMFC stack under practical conditions,” *Journal of Power Sources*, vol. 128, no. 2, pp. 208 – 217, 2004. <https://doi.org/10.1016/j.jpowsour.2003.09.060>.
- [33] N. Yousfi-Steiner, P. Moçotéguy, D. Candusso, D. Hissel, A. Hernandez, and A. Aslanides, “A review on PEM voltage degradation associated with water management: Impacts, influent factors and characterization,” *Journal of Power Sources*, vol. 183, no. 1, pp. 260 – 274, 2008. <http://dx.doi.org/10.1016/j.jpowsour.2008.04.037>.
- [34] C. Damour, M. Benne, B. Grondin-Perez, J.-P. Chabriat, and B. G. Pollet, “A novel non-linear model-based control strategy to improve PEMFC water management - the flatness-based approach,” *International Journal of Hydrogen Energy*, vol. 40, no. 5, pp. 2371 – 2376, 2015. <http://dx.doi.org/10.1016/j.ijhydene.2014.12.052>.
- [35] A. Haddad, R. Bouyekhf, and A. El Moudni, “Dynamic modeling and water management in proton exchange membrane fuel cell,” *International Journal of Hydrogen Energy*, vol. 33, no. 21, pp. 6239 – 6252, 2008. <http://dx.doi.org/10.1016/j.ijhydene.2008.06.014>.
- [36] A. J. Chorin and J. Marsden, *A Mathematical Introduction to Fluid Mechanics*. Springer-Verlag New York, 3rd ed., 1993.
- [37] R. S. Plant and J.-I. Yano, *Parameterization of Atmospheric Convection*, vol. 1. Imperial College Press, 2015.
- [38] H. K. Khalil, *Nonlinear systems*, vol. 3. Prentice Hall, 2002.
- [39] J. Adamy, *Nichtlineare Systeme und Regelungen*, vol. 2. Springer, 2009.
- [40] A. Liapounoff, “Problème général de la stabilité du mouvement,” *Annales de la Faculté des sciences de Toulouse : Mathématiques*, vol. 9, pp. 203–474, 1907.

- [41] A. M. Lyapunov, “The general problem of the stability of motion,” *International Journal of Control*, vol. 55, no. 3, pp. 531–534, 1992. <https://doi.org/10.1080/00207179208934253>.
- [42] A. Bacciotti and L. Rosier, *Liapunov Functions and Stability in Control Theory*. Springer, 2010.
- [43] W. Hahn, *Stability of Motion*. Springer, 1967.
- [44] N. Rouche, P. Habets, and M. Laloy, *Stability Theory by Liapunov’s Direct Method*. Springer, 1977.
- [45] VDI-Gesellschaft Verfahrenstechnik und Chemieingenieurwesen, *VDI Wärmeatlas*. Berlin, Heidelberg : Springer Berlin Heidelberg, 2013.
- [46] P. Brunovský, “A classification of linear controllable systems,” *Kybernetika*, vol. 6, no. 3, pp. 173–188, 1970.
- [47] M. Fliess, J. Lévine, P. Martin, and P. Rouchon, “Sur les systèmes non linéaires différentiellement plats,” *Comptes Rendus de l’Académie des Science*, pp. 1–315, 1992.
- [48] M. Fliess, J. Lévine, P. Martin, and P. Rouchon, “On differentially flat nonlinear systems,” *Proceedings of the 2nd IFAC Symposium on Nonlinear Control Systems (NOLCOS)*, pp. 159–163, 1992. Bordeaux.
- [49] M. Fliess, J. Lévine, P. Martin, and P. Rouchon, “Flatness and defect of non-linear systems: introductory theory and examples,” *International Journal of Control*, vol. 61, no. 6, pp. 1327–1361, 1995. <http://dx.doi.org/10.1080/00207179508921959>.
- [50] M. Fliess, J. Lévine, P. Martin, and P. Rouchon, “A lie-backlund approach to equivalence and flatness of nonlinear systems,” *IEEE Transactions on Automatic Control*, vol. 44, no. 5, pp. 922–937, 1999. <http://dx.doi.org/10.1109/9.763209>.
- [51] J. Lévine, *Analysis and Control of Nonlinear Systems - A Flatnessbased Approach*. Springer, 2009.
- [52] R. Rothfuß, J. Rudolph, and M. Zeitz, “Flatness based control of a nonlinear chemical reactor model,” *Automatica*, vol. 32, no. 10, pp. 1433–1439, 1996.
- [53] R. Rothfuß, *Anwendung der flachheitsbasierten Analyse und Regelung nichtlinearer Mehrgrößensysteme*. VDI Verlag, 1997.
- [54] R. Rothfuß, J. Rudolph, and M. Zeitz, “Flachheit: ein neuer Zugang zur Steuerung und Regelung nichtlinearer Systeme,” *at-Automatisierungstechnik*, vol. 45, no. 11, pp. 517–525, 1997.
- [55] P. Martin, R. M. Murray, and P. Rouchon, “Flat systems,” *4th European Control Conference (ECC)*, 1997. Plenary Lectures and Mini-Courses, Brussels, Belgium.
- [56] P. Martin, R. M. Murray, and P. Rouchon, “Flat systems: open problems, infinite dimensional extension, symmetries and catalog,” in *Advances in the control of nonlinear systems*, pp. 33–57, Springer, 2001.
- [57] P. Rouchon, “Motion planning, equivalence, infinite dimensional systems,” *Applied Mathematics and Computer Science*, vol. 11, no. 1, pp. 165–188, 2001.

- [58] J. Rudolph, *Beiträge zur flachheitsbasierten Folgeregelung linearer und nichtlinearer Systeme endlicher und unendlicher Dimension*. Shaker-Verlag, Aachen, 2003.
- [59] V. Hagenmeyer and E. Delaleau, “Exact feedforward linearization based on differential flatness,” *International Journal of Control*, vol. 76, no. 6, pp. 537–556, 2003.
- [60] V. Hagenmeyer and E. Delaleau, “Robustness analysis of exact feedforward linearization based on differential flatness,” *Automatica*, vol. 39, no. 11, pp. 1941–1946, 2003.
- [61] D. G. Luenberger, “Observing the state of a linear system,” *IEEE transactions on military electronics*, vol. 8, no. 2, pp. 74–80, 1964.
- [62] M. Türk, P. Hils, B. Helfgen, K. Schaber, H.-J. Martin, and M. Wahl, “Micronization of pharmaceutical substances by the rapid expansion of supercritical solutions (ress): a promising method to improve bioavailability of poorly soluble pharmaceutical agents,” *The Journal of Supercritical Fluids*, vol. 22, no. 1, pp. 75 – 84, 2002. [https://doi.org/10.1016/S0896-8446\(01\)00109-7](https://doi.org/10.1016/S0896-8446(01)00109-7).
- [63] P. Debenedetti, J. Tom, X. Kwauk, and S.-D. Yeo, “Rapid expansion of supercritical solutions (ress): fundamentals and applications,” *Fluid Phase Equilibria*, vol. 82, pp. 311 – 321, 1993. [https://doi.org/10.1016/0378-3812\(93\)87155-T](https://doi.org/10.1016/0378-3812(93)87155-T).
- [64] International Electrotechnical Commission, “Fuel cell technologies - part 1: Terminology,” *IEC TS 62282-1:2005*, 2005.
- [65] International Electrotechnical Commission, “Fuel cell technologies - part 1: Terminology,” *IEC TS 62282-1:2013*, 2013.
- [66] R. K. Ahluwalia, X. Wang, T. Q. Hua, and D. Myers, “Fuel Cell Systems for Transportation: Recent Developments in U.S.A.,” *IEA Annex 26/35 Meeting*, 2014. Presentation.
- [67] B. D. James, J. M. Moton, and W. G. Colella, “Fuel Cell Transportation Cost Analysis,” *Annual Merit Review and Peer Evaluation Meeting*, 2014. Presentation.
- [68] SAE Fuel Cell Standards Committee, “Recommended Practice for Testing Performance of PEM Fuel Cell Stack Sub-system for Automotive Applications,” *Standard J2617_200711*, 2007. https://doi.org/10.4271/J2617_200711.

Dipl.-Ing. János Kancsár

Curriculum Vitae



Personal Data

Date of Birth



Place of Birth



Citizenship



Education

- 03/2014 - Present Vienna University of Technology
Doctoral Programme in Engineering Sciences
Mechanical Engineering with Specialisation in Automation and Control
Research in the Field of Nonlinear Multivariate Control
- 02/2011 - 09/2013 Vienna University of Technology
Master Programme Technical Physics
Specialisation in Atomic, Nuclear and Particle Physics
Research in the Field of Data Analysis at the CMS Experiment at CERN/LHC, Graduated with High Distinction
- 08/2009 - 09/2010 Linköping University, Sweden
Exchange Year
- 10/2006 - 02/2011 Vienna University of Technology
Bachelor Programme Technical Physics
- 10/2000 - 06/2005 **TGM**, Vienna
Electronics and Telecommunication
A-levels, Graduated with High Distinction

Diploma Thesis

- Title Search for New Physics Phenomena Based on
Top-Antitop Quark Production
- Supervisor Univ. Prof. Dr. Christian Fabjan

Bachelor Thesis

Title Nanostrukturen an Oberflächen
Supervisor Prof. Michael Schmid

Experience

03/2014 - 12/2017 Vienna University of Technology
Institute of Mechanics and Mechatronics
Division of Control and Process Automation

08/2012 - 07/2013 Austrian Academy of Science
Institute of High Energy Physics
Division of CMS Data Analysis at CERN/LHC

Computer skills

Systems Linux, Windows, Microcontroller, dSpace/MicroAutoBox
Programming Assembler, C/C++, Python, Matlab/Simulink
Networks Cisco CCNA Semester 1&2
Office MS Office, Latex

Languages

German Native Language
Hungarian Native Language
English Fluent in Written and Spoken

Peer Reviewed Publications

- 2016 János Kancsár, Martin Kozek and Stefan Jakubek, Flatness-based feedforward control of polymer electrolyte membrane fuel cell gas conditioning system, *International Journal of Hydrogen Energy* 2016, 41 (39): 17526 - 17538.
<https://dx.doi.org/10.1016/j.ijhydene.2016.06.086>
- 2017 János Kancsár, Michael Striednig, David Aldrian, Alexander Trattner, Manfred Klell, Christoph Kügele, Stefan Jakubek, A novel approach for dynamic gas conditioning for PEMFC stack testing, *International Journal of Hydrogen Energy* 2017, 42 (48): 28898 - 28909.
<https://doi.org/10.1016/j.ijhydene.2017.09.076>
- 2017 Elisabeth Luchini, Alexander Schirrer, János Kancsár, Martin Kozek, Hierarchical multiple sampling rate MPC for mixed-integer optimisation applied to redundant refrigeration circuits [submitted], *Journal of Process Control*

Patents

Granted Patents

- 15.07.2017 Patent AT 518518 B1 2017-11-15 describes a model-based nonlinear multivariate control concept for the gas conditioning system of fuel cell stack test beds.

Pending Patent Applications

- 2016 Patent PCT/EP2017/081122 (AV-3887AT) describes a novel concept for gas humidification based on supercritical water injection.
- 2017 Patent A51007/2017 (AV-3947AT) describes a soft-sensor concept, which can be used to improve transient relative humidity measurements.
- 2017 Patent A51040/2017 (AV-3957AT) describes a Power-Hardware-in-the-Loop (PHiL) concept for dynamic fuel cell stack testing.